TIME DOMAIN SIMULATION FOR SOUND PROPAGATION OVER VARIOUS OBJECTS AND UNDER VORTICAL BACKGROUND CONDITIONS

By

Wen Li

Submitted to the graduate degree program in Department of Aerospace Engineering and the Graduate Faculty of the University of Kansas in fulfillment of the requirements for the degree of Master of Science.

_____

Chairperson Dr. Zhongquan Charlie Zheng

_____

Dr. Saeed Farokhi

_____

Dr. Ray Taghavi

Date Defended: May 11, 2015

The thesis committee for Wen Li

certifies that this is the approved version of the following thesis:

TIME DOMAIN SIMULATION FOR SOUND PROPAGATION OVER VARIOUS OBJECTS AND UNDER VORTICAL BACKGROUND CONDITIONS

_____

Chairperson Dr. Zhongquan Charlie Zheng

_____

Dr. Saeed Farokhi

_____

Dr. Ray Taghavi

Date approved: May 11, 2015

Abstract

Acoustic wave propagations have been studied for a long time with both experimental and numerical methods. Most of the analytical solutions for wave propagations are considered for simple environments such as a homogeneous atmospheres. As a result, the analytical solutions are unable to be applied for complicated environments. Numerical methods have become more and more important in acoustics studies after decades of development. The finite difference time-domain method (FDTD) is one of the most commonly used numerical methods in wave propagation studies. Compared with the other methods, the FDTD method is able to include many aspects of sound wave behaviors such as reflection, refraction, and diffraction in the physical problems.

In this thesis, the linearized acoustic Euler equations coupled with the immersed boundary method are applied to investigate the sound wave propagation over complex environments. For the three-dimensional simulations of sound wave propagation in long distance, the moving domain method and parallel computing techniques are applied. Based on these approaches, the computational costs are significantly reduced and the simulation efficiency is greatly improved. When looking into the effects of high subsonic vortical flow, a high order WENO scheme is applied for the simulation. In this way the simulation stability can be achieved and the sound scattering of vortical flow can be studied. Then, the numerical scheme is applied to simulate an ultrasonic plane wave propagating through biological tissue. The linearized Euler acoustic equations coupled with the spatial fractional Laplacian operators are used for numerical simulations. The absorption and attenuation effects of the biological lossy media are successfully observed from the simulation results. Throughout this thesis, the simulation results are compared

with either experimental measurements or analytical solutions so that the accuracy of the implemented numerical scheme is validated.

Acknowledgments

First of all, I would like to give my sincerest thanks and appreciation to my advisor Dr. Zhongquan Charlie Zheng for his great guidance and support throughout my time at KU. His invaluable encouragement and patience is a great source of inspiration for me and helps me overcome many challenges encountered during my research.

I would like to give my special thanks to my thesis committee members: Dr. Farokhi and Dr. Taghavi. They have generously given their time and assistance in support of my research. The knowledge they have taught me helps me acquire a better understanding for my graduate study.

I need to express my deep appreciation to Dr. Guoyi Ke, who gives me his unreserved guidance for my research. I am also genuinely grateful for my group mates Anpeng He, Haidong Liu and Juanjian Zhang for their precious companionship and assistance. I have to give my special thanks to Lei Shi and Rohith for their unreserved help and encouragements.

Last, my endless gratitudes are given to my dearest parents. Their great love and company help me overcome all the hard time and finish my graduate career successfully.

.

Contents

List of Figures

List of Tables

1. Introduction

Sound propagation under various environments has received a lot of interest during the past several decades because of its high practical value in engineering. First, the outdoor sound propagation study can be applied to noise control in Ref. [1]-[6]. The quality of human living could be greatly improved by controlling the noise that is generated from vehicles, railways, airplanes and factories. The early studies were focused on simple models involved with homogeneous environments and isentropic propagations. With the development of numerical methods and computational techniques, more complicated circumstances were considered such as impedance ground, nonhomogeneous atmospheric conditions, turbulence, vortical flow, barriers with different shapes, and long distance propagation. Nowadays the numerical simulations can give more and more accurate predictions for more generalized environments. In noise control studies, the most general factor for outdoor acoustics is the complex impedance of the ground. It is defined as the ratio of pressure amplitude to the normal component of velocity amplitude evaluated at the ground surface in Ref. [7]. Usually the ground surface can be divided into two types: rigid and porous. For rigid ground, such as glass or water, the incident sound wave will be completely reflected back without any transmissions into the ground. For porous ground, such as grass, snow or sand, part of the wave will be reflected back, while the other part will propagate into the ground and be absorbed. The parameter for determining how much wave can be reflected and absorbed in porous ground is called flow resistivity.

Besides the applications for noise control, the study of ultrasound propagation in biological tissue can be applied in medical and therapeutic fields. This application can be categorized as the diagnostic application for signal processing and medical imaging in Ref. [8]-[13], and also as

therapeutic application. High intensity ultrasound can be used for tissue healing, ultrasonic surgery and destroying blood clots or internal stones in Ref. [14]-[19].

The research of sound propagation is also playing an extremely important role in the military filed. This technology that can be used for navigation, communication, detecting objects and tracking targets. The most famous application of this technology in the military is sonar, which is widely used in submarines.

1.1 Background Review

Sound propagation has been studied both analytically and numerically during the past decades. Since the analytical solutions are only capable in simple homogeneous circumstances, the numerical method becomes a powerful method when more realistic conditions are considered. So far there are many of numerical methods that have been developed for modeling acoustic waves, for example the Fast Field Program (FFP), Parabolic Equation Method (PEM), Boundary Element Method (BEM) and Finite Difference Time-Domain (FDTD) method.

The FFP method uses a spatial Fourier transform to the wave equation which transforms spatial domain into the wave number domain in Ref. [20]. The physical sound solutions can be solved by an inverse Fourier transform, after solving the wave equations numerically in the wave number domain. The FFP method was first derived in Ref. [21]-[22] for two-dimensional sound propagation simulations in inhomogeneous atmospheres, and the three-dimensional FFP method was derived in Ref. [23]-[24] for moving atmospheres. This method is also introduced for underwater acoustics to study the effects of sound speed variations in Ref. [25]-[26]. In the early 1980s it was adapted for atmospheric sound propagation in Ref. [27]-[31]. The FFP method can obtain accurate predictions of the sound field in the situation of a range-independent propagation

environment, but the disadvantage is that the method is limited to a horizontally stratified atmosphere and homogeneous ground surfaces.

The PE method is based on the axis-symmetric approximation form of the parabolic wave equation. It was first introduced for electromagnetic wave propagation in Ref. [32], and after that the PE Method was widely applied in sound propagation studies. The two main formulations for the PE method are Green's Function Parabolic Equation (GFPE) method, which was developed in Ref. [33]-[36], and the Crank-Nicholson Parabolic Equation (CNPE). A Wide Angle PE (WAPE) Method was introduced for sound propagation through a single vortex in Ref. [37]. For the GFPE method, Green's function of a point source is used with Fourier transforms for sound wave propagation. For CNPE method, the Crank-Nicholson finite difference scheme is used for numerical evaluations. Gilbert and White first applied the two-dimensional PE method to atmospheric sound propagation in Ref. [38]-[39]. They predicted the outdoor sound propagation over an impedance ground, and the atmosphere profiles of both downward-refraction and upward-refraction. Later, the PE method was applied successfully for underwater wave propagation in Ref. [40]-[41], long range sound propagation in the atmosphere in Ref. [42] and low-frequency sound propagation over a locally reacting boundary in Ref. [43]-[44]. Near the 21st century, the PE method was used for numerical simulations of sound wave propagation with complex topography in Ref. [45]-[52]. For sound wave propagation over inhomogeneous turbulent atmospheres, the PE method was applied by Chevret in Ref. [53] and Dallois in Ref. [54]. In the early 1990s, Collins introduced a PE starter called the self-starter in Ref. [55] which was based on high-order parabolic approximations. And this method was improved by using an operator of the split-step solution in Ref. [56]-[57].

The Boundary Element Method (BEM) is another popular method for sound propagation numerical simulations. It was first introduced in the early 1960s in Ref. [58]. The BE method is typically applied to steady state problems such as radiation from an arbitrary source, and it was successfully used for time-domain numerical simulations in Ref. [59]-[61]. Chandler and Hothersall in Ref. [62] applied the BE method for wave propagation with complex terrain, and it was improved for solving meteorological influences in Ref. [63]. Later, the BE Method was used to solve Helmholtz equations in both bounded interior and unbounded exterior domains in Ref. [64]. One big advantage of the BE method is that only the boundary of the domain and interfaces need to be discretized instead of the entire computational domain.

The Finite Difference Time-Domain (FDTD) method has become one of the most common tools for numerical simulations, and it has been widely used for outdoor sound propagation studies in recent years. Kelly first introduced a two-dimensional finite difference method for second order elastic wave equations in Ref. [65]-[66]. J. Vireux applied the FD method for shear vertical waves and shear horizontal waves in Ref. [67]-[68] by using the basic elastic wave equations with staggered grid. Later, the FD method was used for wave propagation studies under various circumstances such as sonic logging in Ref. [69]-[70], sound scattering by a single vortex in Ref. [71] and [72], wave propagation over rigid and impedance ground in Ref. [73]-[74], wave propagation over turbulent atmospheric flow in Ref. [75]-[76] and wave propagation over complex terrain in Ref. [77] and [78]. More recently Cotte et al. developed the time-domain impedance boundary conditions in Ref. [79] based on a recursive convolution method, and later Dragna et al. extended this method for two-dimensional long distance wave propagations in Ref. [80] for both homogeneous and downward reacting atmospheres. The FD method was also applied by Bohlen for three-dimensional wave propagation simulations in Ref. [81] with the domain decomposition

approach. The disadvantage of the FDTD method is that it requires tremendous computational memory, especially for three-dimensional and long propagation distance simulations. However, combined with the moving-zonal method and parallel computing techniques, the FDTD method has been much more efficient for outdoor sound wave propagation simulations. In this thesis, the Finite Difference Time Domain method is applied to implement all the numerical simulations. To show the capacity and accuracy of this method, one example is given below.

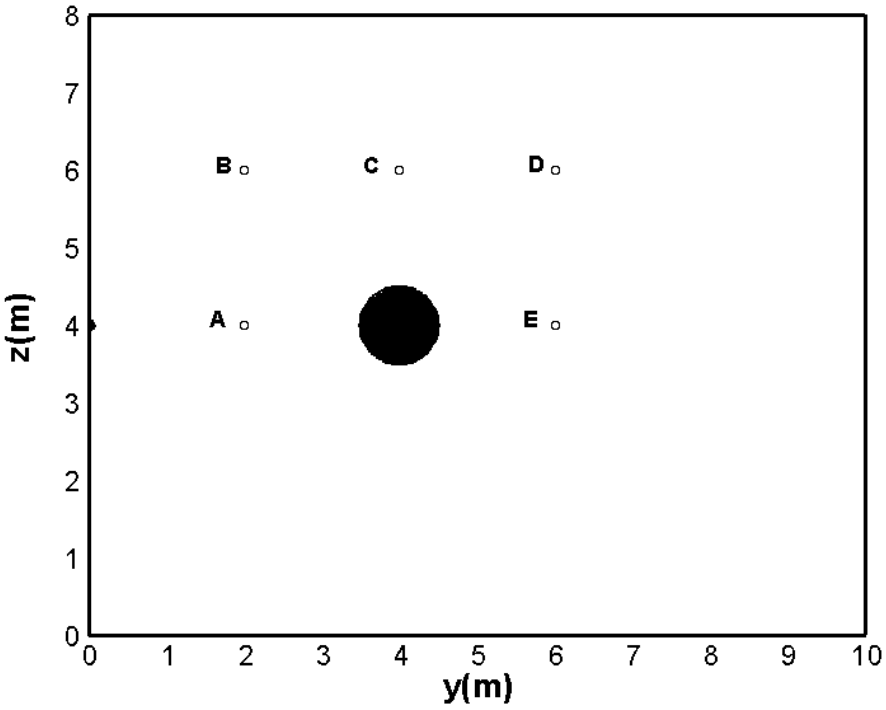

Fig. 1.1 Description of the geometry and coordinate system for Benchmark problem simulation

The following simulation is based on the 2D Benchmark problem discussed in Ref. [82]. A two-dimensional point source with a rigid obstacle is simulated in a rectangular domain $y \in [0,10]$m and $z \in [0,8]$m. The circular rigid barrier with radius 0.5m is located at (4, 4). A uniform grid size $\Delta y = \Delta z = 0.008$m is used and the time step is chosen as $\Delta t = 2.5 \times 10^{-6}$s. The time

domain is 29.4ms which is based on the y-direction domain size. The perfectly-matched-layer in Ref. [83]-[85] is specified at the top and bottom boundary of the domain with thickness 1m. The point sound source is located at (0, 4) with the Gaussian distribution in Ref. [82]. The pressure is non-dimensionalized and given like below:

$$p = \varepsilon \exp\left[-\ln(2)\left(\frac{x^2 + y^2}{0.04} \right) \right] \tag{1.1}$$

where $\varepsilon = 10^{-3}$. Five receivers A-E are put at (2, 4), (2, 6), (4, 6), (6, 6) and (6, 4). The geometry and coordinate system is shown in Fig. 1.1. The pressure contours of this simulation are given in Fig. 1.2 for several different moments. The pressure distributions clearly show that parts of the incident sound wave propagated through the rigid circular barrier, while the other parts were reflected back.

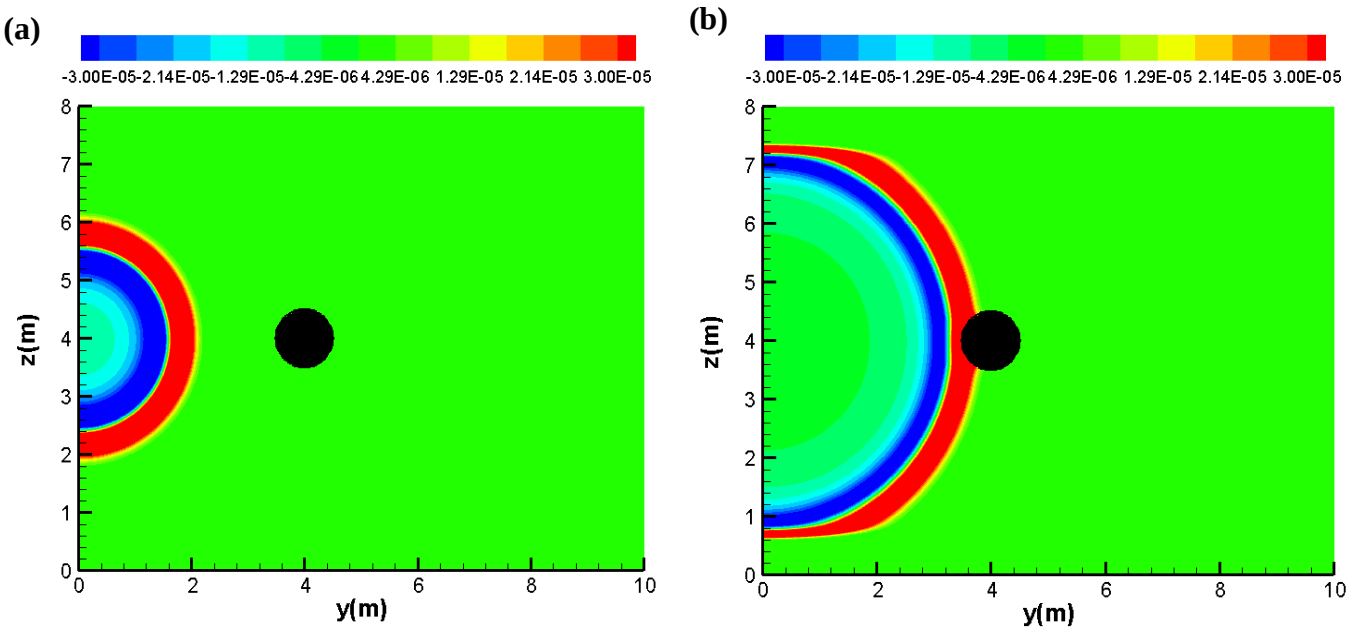

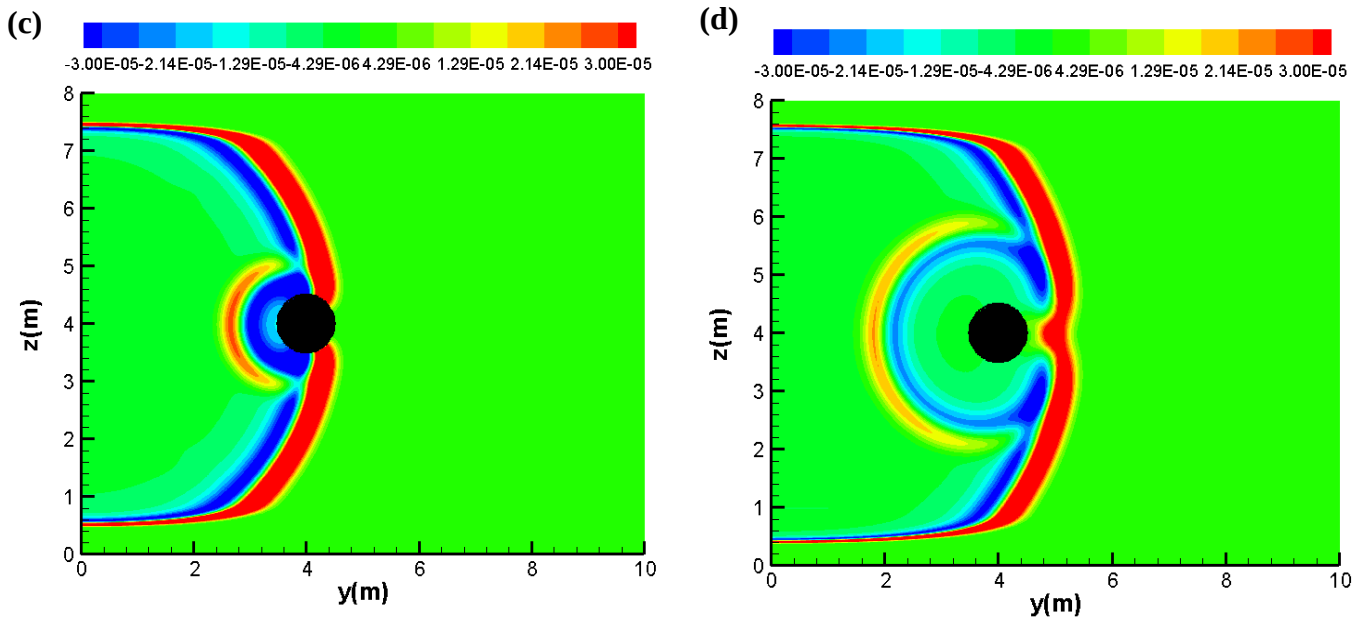

Fig. 1.2 Pressure contours of Benchmark problem simulation (a) t=5ms, (b) t=10ms, (c) t=12.5ms, (d) t=15ms.

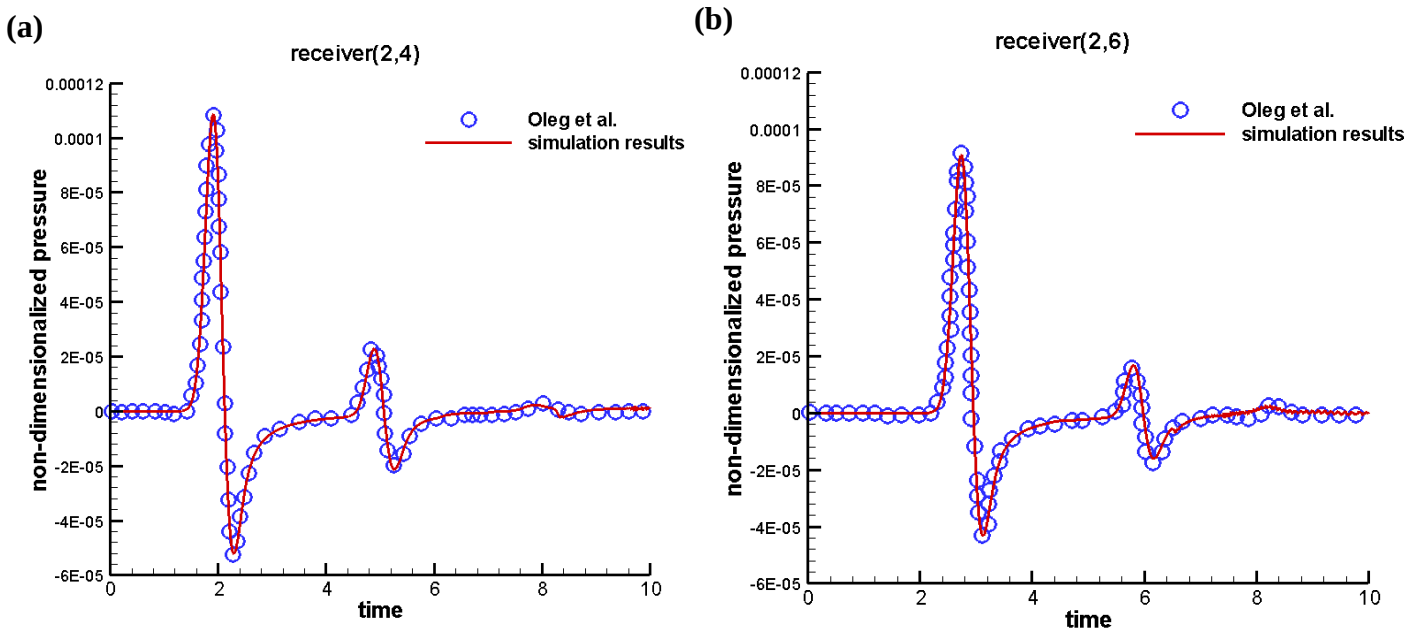

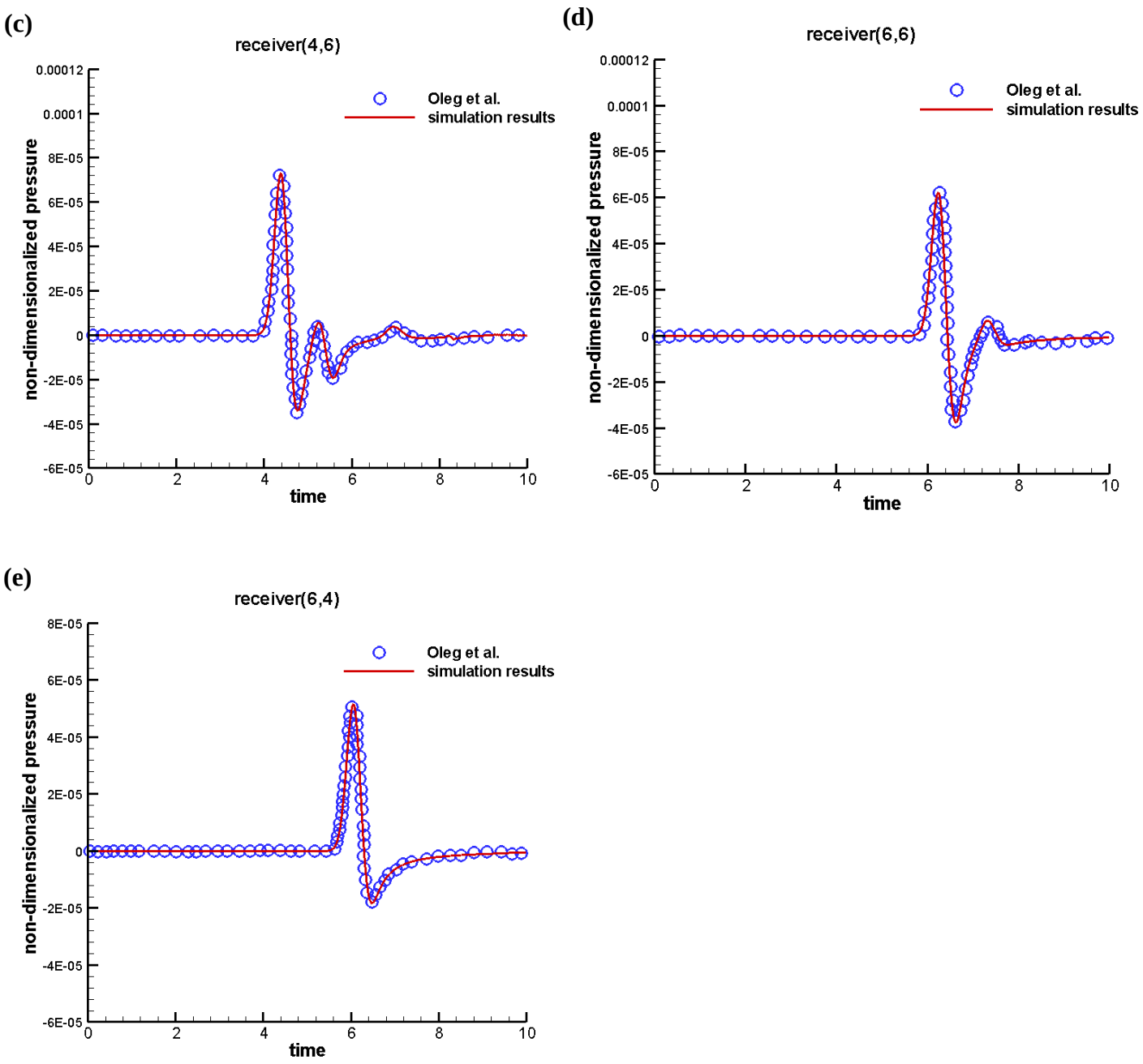

Fig. 1.3 2D Benchmark problem numerical pressure compared with analytical solutions

(a) receiver A, (b) receiver B, (c) receiver C, (d) receiver D, (e) receiver E.

The non-dimensionalized numerical pressure versus non-dimensionalized time is shown in Fig. 1.3 with the corresponding analytical solution in Ref. [82]. The time is non-dimensionalized by L / c, where L is the unit length and c is speed of sound. It can be seen that the numerical results are in excellent agreement with the analytical solutions. This finite difference time-domain numerical method is validated to be accurate. The corresponding error analysis for the applied numerical scheme is given in Appendix B.

1.2 Thesis Outline

This thesis is dedicated to study the outdoor sound propagation under different environments. The finite difference time-domain method is applied for the numerical simulations. The numerical results of each different simulation are validated by comparing the corresponding analytical solutions or experimental data.

This thesis is organized as follows. It is consisted of five chapters. The first chapter provides some background that describes different numerical methods for acoustics studies and their common applications. In chapter 2, the sound blockage effect of sonic crystals are studied. The sonic crystals are modeled as regular arrays of cylinder barriers. The different sound blockage effects caused by different numbers of cylinders, different materials of cylinders and rigid ground are studied. The finite difference time-domain numerical scheme coupled with immersed boundary method is applied for both two-dimensional and three-dimensional simulations, and the numerical results are verified by comparing the experimental data. The theoretical Bragg band gap can be successfully obtained by using the current numerical scheme. For three-dimensional simulations, the moving-zonal method is applied, and the numerical results are validated by comparing with the corresponding non-moving simulation results.

In chapter 3, the scattering effects of vortex dipole on two-dimensional sound wave propagation is studied. When acoustic wave propagates through a vortex or vortex dipole, both the amplitude and phase of the incident wave are affected. The different sound scattering effects caused by different strength of vortical flow and vortex pair placements are studied. For this problem a fifth order WENO scheme is applied for the convection terms. Besides the fixed vortex pair, numerical simulations for moving vortex pair are also conducted. The accuracy of the implemented numerical schemes are validated by the very good agreement between the numerical results and the analytical solutions.

In chapter 4, we study the absorption and dispersion effects of the ultrasonic wave propagation through biological tissue. The biological tissue is considered as a kind of lossy media with acoustic attenuation, whether caused by molecular relaxations or scattered by small random particles. We uses the linearized Euler acoustic equations coupled with space-fractional Laplacian operators for the ultrasound simulations.

Finally, the last chapter provides a summary and conclusions of the completed work. Current limitations and future developments are discussed.

2 Sound Propagation around Arrays of Cylinders

Sound propagation over sonic crystals has attracted a lot of interests and been studied during the past few decades. In the late 1980s, several authors showed that a transparent material can become opaque for any light wave vector provided that a strong modulation of the refractive index in the three dimensions of the space is attained in Ref. [86]. In the 90s it was demonstrated that sculptures built by the periodic arrays of cylinders inhibited the sound transmission for certain frequency ranges related to this modulation just as photonic crystals do with light in Ref. [87]. For this reason the sonic crystals are defined as a periodic arrangement of structures made of sound hard scatterers, and the sound can be attenuated in a certain range of frequency in Ref. [88]. For an infinite periodic structure, there is a range of frequencies known as band gap. At the gap frequency, the sound attenuation level is usually increased. Therefore, the sonic crystals can also be applied to environmental noise control.

So far the most used numerical methods for solving sound propagation over sonic crystals are Boundary Element Method (BEM) and Finite Element Method (FEM) in Ref. [89]-[91]. With the advent of high performance computers, the Finite Difference Time Domain (FDTD) method has evolved to be powerful and effective way for simulating sound propagation around complex geometries, different media and moving objects. By making use of parallel computation techniques, the simulation time can also be significantly reduced in Ref. [92]. Besides all the numerical methods, the corresponding analytical solutions and experiments are also studied for sonic crystals research in Ref. [88], [93] and [94].

In this study, the linearized Euler equations are employed for sound propagation in air media and Zwikker-Kosten equations in Ref. [95] for sound propagation inside the objects that are

modeled as made of porous materials. Different scales of regular square lattice arrays are simulated for both two-dimensional and three-dimensional cases to study the sound attenuation effect.

In this chapter, the numerical model, governing equations and simulation domain geometry are described, with a brief explanation of the FDTD numerical simulation. Then the simulated sound attenuations are compared among different simulations, and also compared with experimental data offered in Ref. [88]. At last, the summary and conclusions are given.

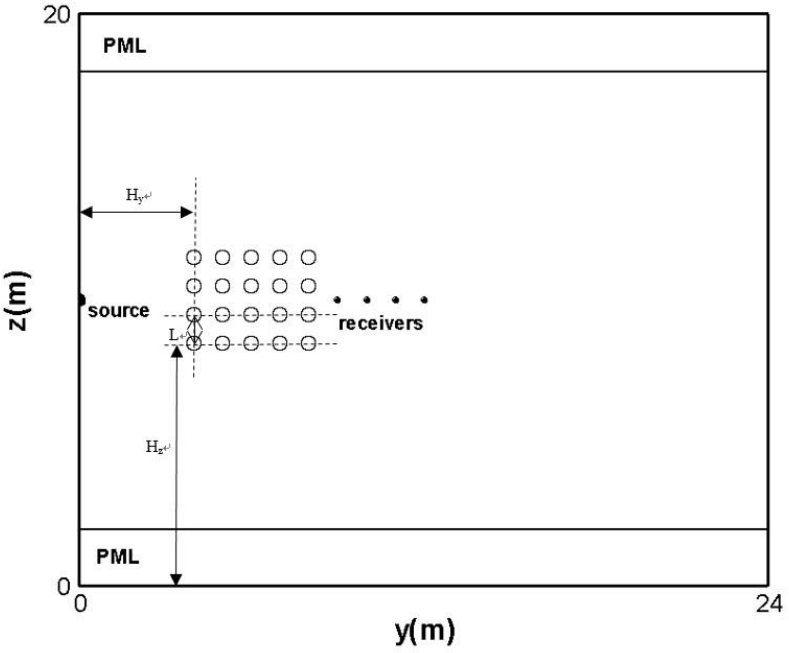

Fig. 2.1 Description of the geometry for regular array cylinder barriers.

2.1 2D Numerical Model Description

Figure 2.1 shows the geometry of the numerical model of the two-dimensional simulations for sound propagation through sonic crystals. The perfectly-matched-layer (PML) boundary conditions in Ref. [83]-[85] are set at top, bottom and left boundaries to represent non-reflective free field boundaries. We use the Gaussian pressure distribution for the sound source, and the other parameters ambient pressure $p_{av} = 100\text{kPa}$, $\gamma = 1.4$, speed of sound $c = 340\text{m/s}$, porosity $\Omega = 0.3$,

porous media structure factor $c_s = 3$. The flow resistivity of cylinders $\sigma = 4\times10^8\,\text{Pa s m}^{-2}$ which means the cylinders are rigid for sound propagation. The stability of the numerical scheme has been discussed in details in Ref. [96].

The definition of sound attenuation is

$$\Delta L = 20\lg\frac{p_f}{p} \tag{2.1}$$

Where p_f is the pressure simulated at the same location as p but without cylinder arrays.

For all the simulations of wave propagate through cylinder arrays in free field, the domain size is $24\text{m}\times20\text{m}$. The grid size $\Delta y = 0.008\text{m}$ and $\Delta z = 0.008\text{m}$ is used as a uniform grid. The radius of the cylinders is 0.25m and the lattice constant L which the distance between the centers of two cylinders which showed in figure 5.1 is 1m. Seven different kinds of cylinder arrays are tested, the corresponding parameters Hy and Hz of each case are listed in table 2-1:

Table 2-1 Parameters of different cylinder barriers array for 2D simulations

Cylinder array	H_y (m)	H_z (m)
3×3	5	9
3×4	5	8.5
3×5	5	8
3×6	5	7.5
4×3	5	9
4×4	5	8.5
5×4	4	8.5

The time step $\Delta t = 2.5\times10^{-6}$s and whole simulation time is 66.25ms. By that the wave propagates 22.525m when the simulation ends. The sound source is at (0 10) m and four receivers are put at the centerline along the y-direction with different distances from the source: (9 10) m, (10 10) m, (11 10) m and (12 10) m.

2.2 Results of 2D Simulations and Discussions

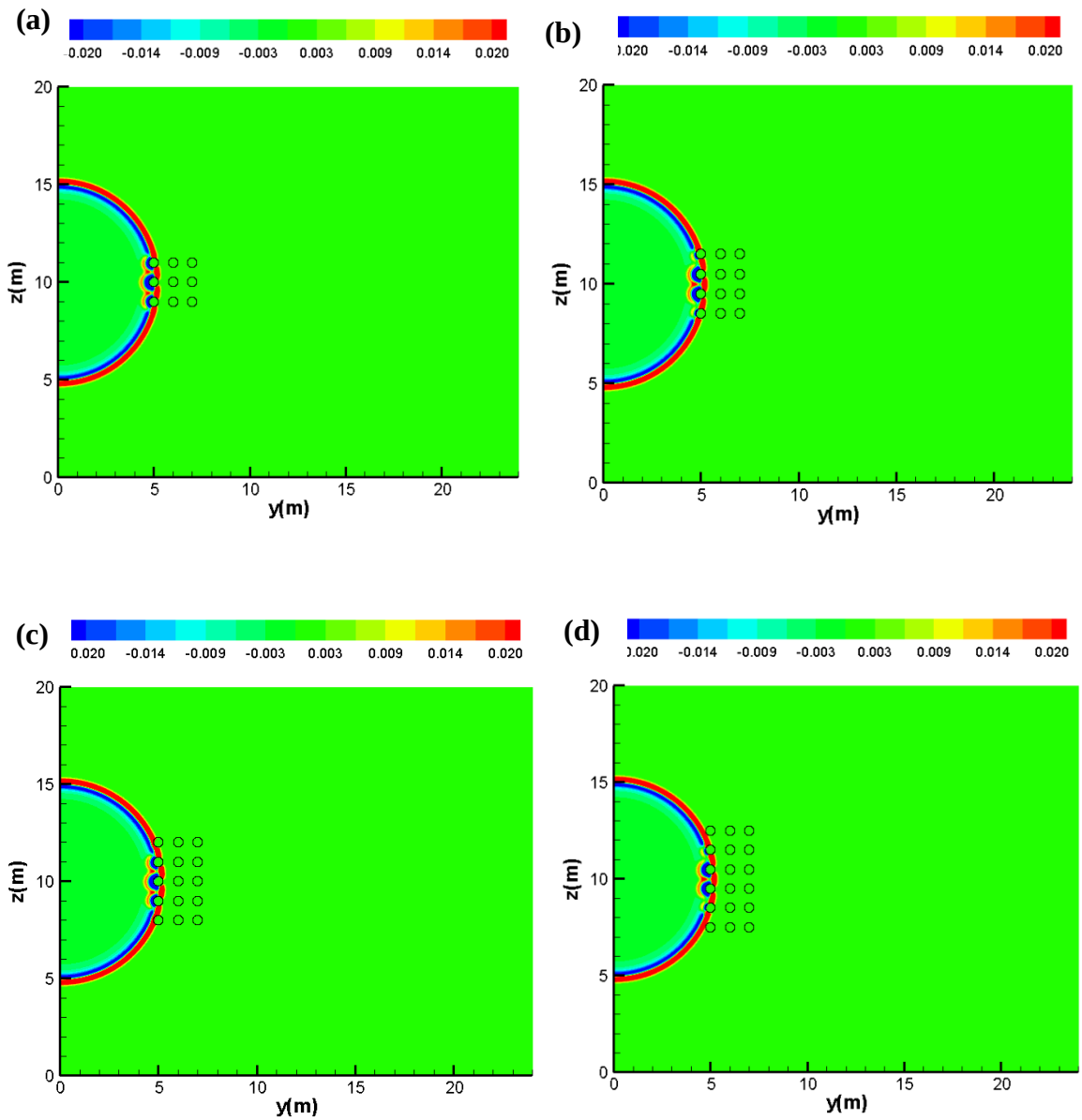

.

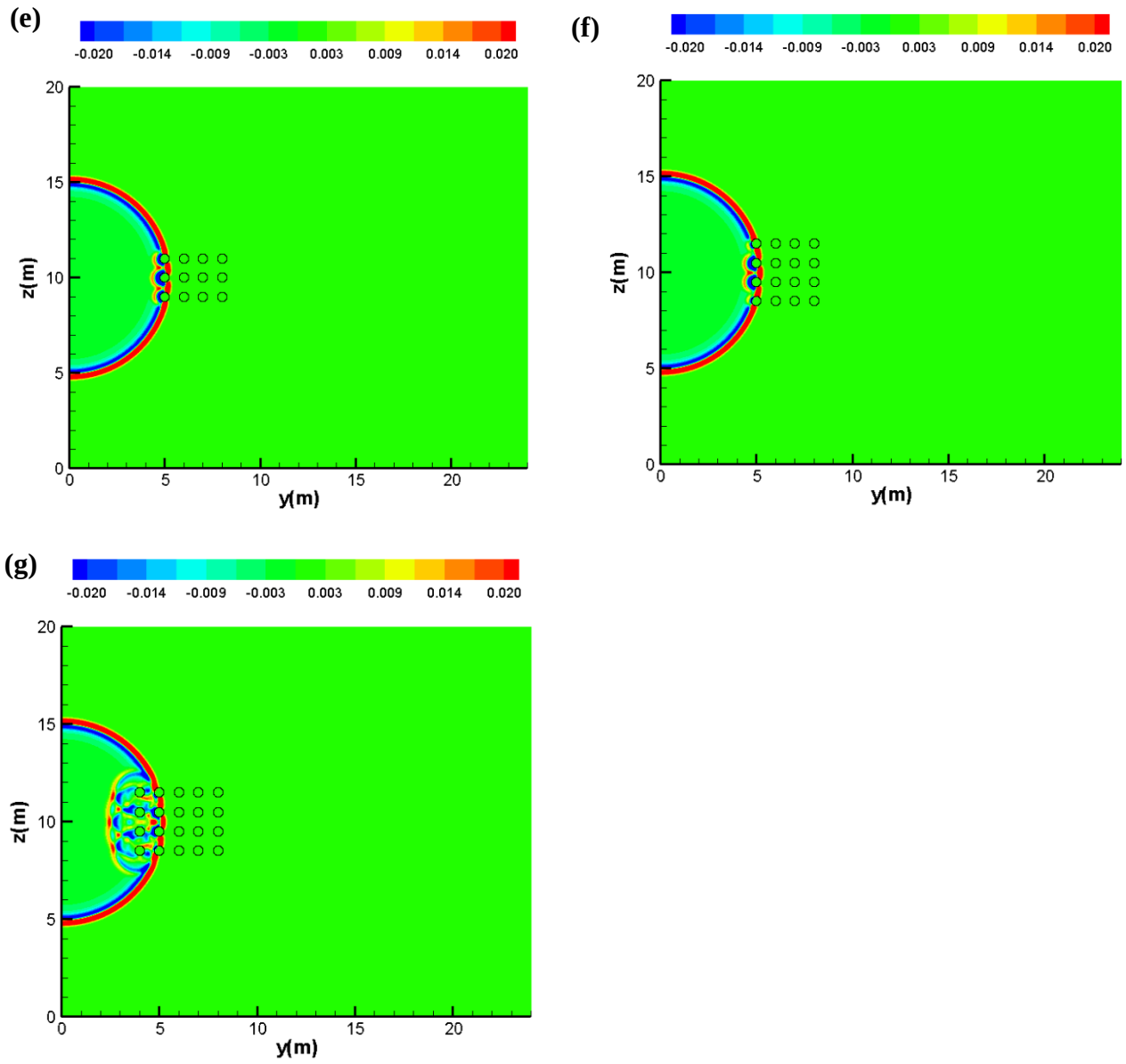

Fig. 2.2 Pressure contours at the moment t=15ms (a) 3x3 cylinders (b) 3x4 cylinders (c) 3x5 cylinders (d) 3x6 cylinders (e) 4x3 cylinders (f) 4x4 cylinders (g) 4x5 cylinders

Figures 2.2 and 2.3 are the pressure contours of the simulations for the seven different cylinder arrays. The contours clearly show the process of the wave propagating through the rigid cylinders and the interactions between the incident waves and reflected waves. Figure 2.2 shows the pressure contours at the moment t=15ms that the wave reaches the first column of the cylinder array, and

Fig. 2.3 shows the pressure contours at the moment t=35ms when the wave already passes the cylinder array.

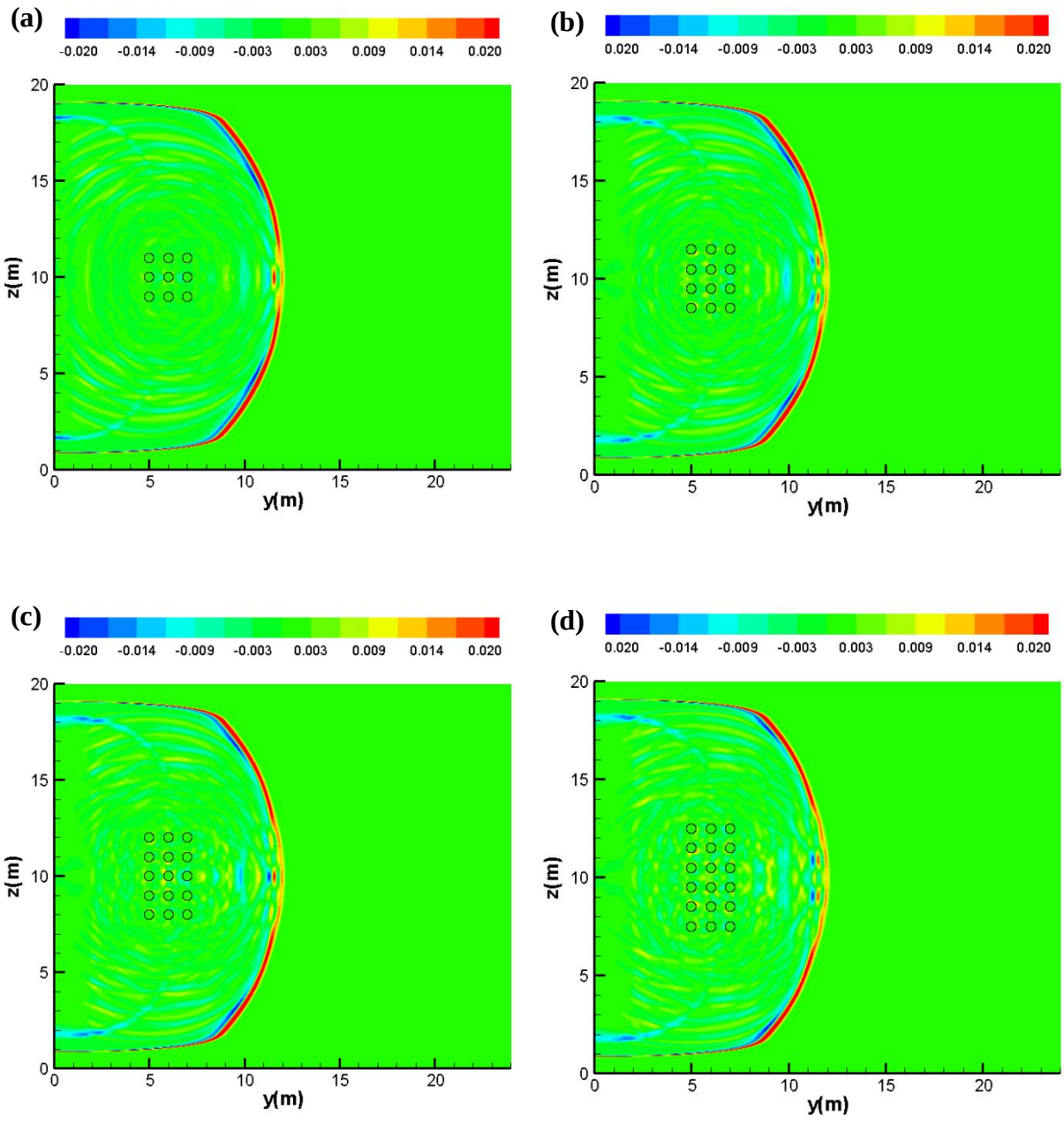

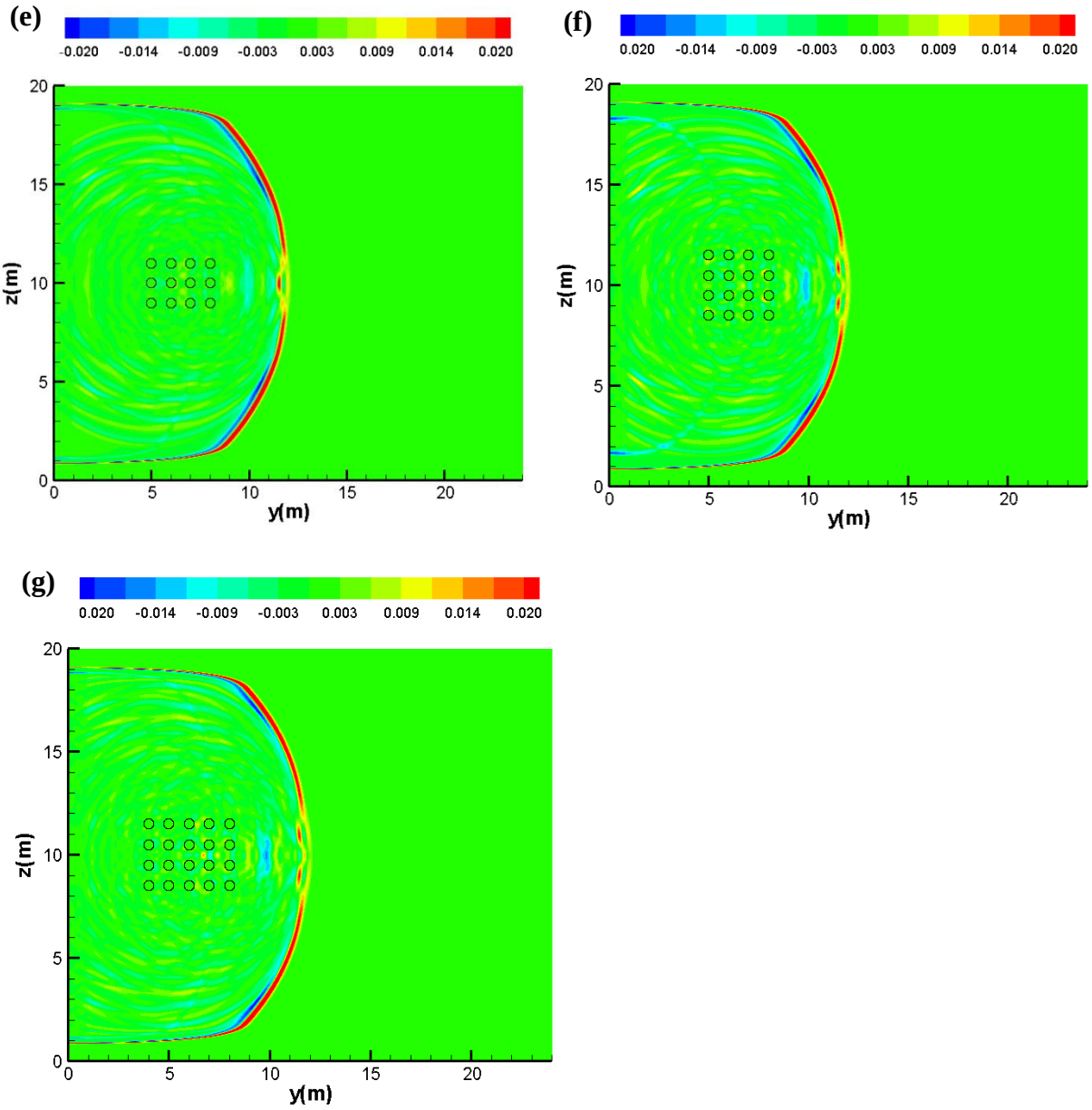

Fig. 2.3 Pressure contours at the moment t=35ms (a) 3x3 cylinders (b) 3x4 cylinders (c) 3x5 cylinders (d) 3x6 cylinders (e) 4x3 cylinders (f) 4x4 cylinders (g) 4x5 cylinders

Figure 2.4 shows the simulated sound attenuations of the four different receivers in each cylinder array. By comparing the sound attenuations from four different receivers, we can find that when the cylinder barriers are 3×3 array or 4×3, the nearest receiver (9, 10) m has the highest sound attenuation level, but at several frequencies the sound attenuation is below zero. As the number of cylinders is increasing, like $3\times4, 3\times5$ and 3×6, the nearest receiver no longer has the best sound blockage effect. The sound attenuation curves of the four receivers start to change more rapidly and have more peaks and dips. For example when the cylinder array is 4×4, the nearest receiver (9, 10) m has the lowest sound attenuation instead of the highest. The reason can be illustrated in the previous pressure contours showed in Fig. 2.2 and 2.3. We can see that more cylinder barriers can induce more reflections in the domain. Therefore the sound pressure level is even strengthen for the nearest receiver, instead of blocking the sound.

We can also see that for all the different cylinder arrays and different receivers, they all have the first sound attenuation peak at the frequency about 170Hz, even though the magnitude of sound attenuation of each case is very different. This phenomenon is explained by the Bragg's diffraction law in Ref. [88]. The theoretical Bragg band gap frequency is

$$f = \frac{c}{2L}$$

Where c is the speed of sound, and L is the sonic crystals lattice constant, with the values of $c = 340\text{m/s}$ and $L = 1\text{m}$. Therefore the theoretical band gap frequency is $f = \frac{340}{2\times1} = 170\text{Hz}$, which matches the numerical results very well. In addition to the Bragg band gap frequency, the results from all the different cylinder arrays also have a common that they all have the first dip at frequency around 250Hz. Besides that the magnitudes are also almost the same, around the sound attenuation 0dB.

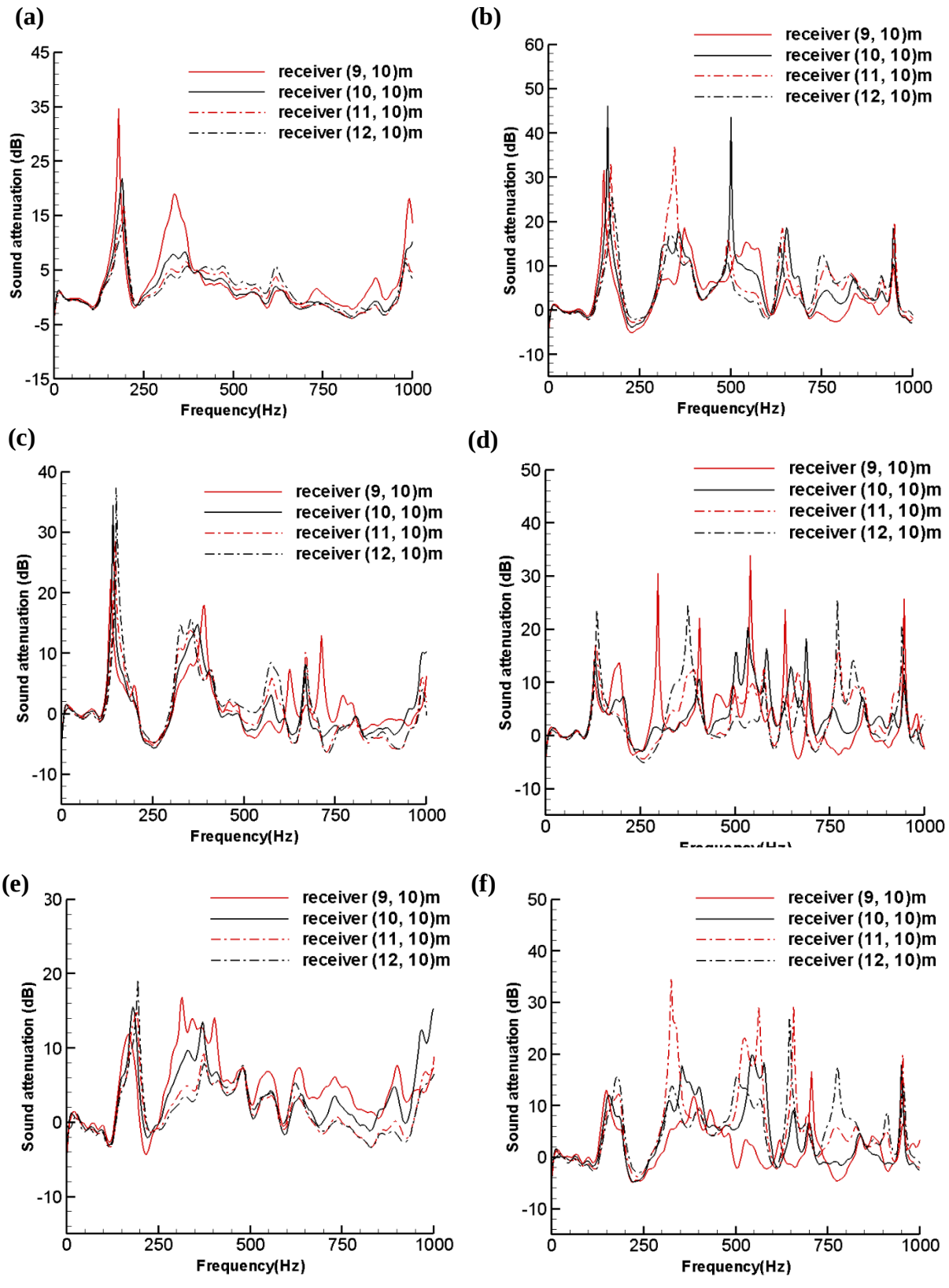
(a)
receiver (9, 10)m
receiver (10, 10)m
receiver (11, 10)m
receiver (12, 10)m
Sound attenuation (dB)
Frequency(Hz)
(b)
receiver (9, 10)m
receiver (10, 10)m
receiver (11, 10)m
receiver (12, 10)m
Sound attenuation (dB)
Frequency(Hz)
(c)
receiver (9, 10)m
receiver (10, 10)m
receiver (11, 10)m
receiver (12, 10)m
Sound attenuation (dB)
Frequency(Hz)
(d)
receiver (9, 10)m
receiver (10, 10)m
receiver (11, 10)m
receiver (12, 10)m
Sound attenuation (dB)
(e)
receiver (9, 10)m
receiver (10, 10)m
receiver (11, 10)m
receiver (12, 10)m
Sound attenuation (dB)
Frequency(Hz)
(f)
receiver (9, 10)m
receiver (10, 10)m
receiver (11, 10)m
receiver (12, 10)m
Sound attenuation (dB)
Frequency(Hz)

(g)

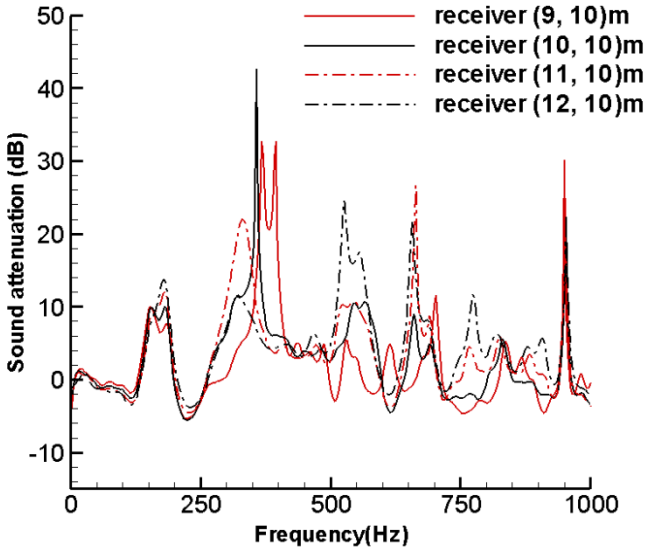

Fig. 2.4 Sound attenuations versus frequency for four receivers (a) 3x3 cylinders (b) 3x4 cylinders (c) 3x5 cylinders (d) 3x6 cylinders (e) 4x3 cylinders (f) 4x4 cylinders (g) 4x5 cylinders

When the number of cylinders in y-direction is fixed as 3 columns, figure 2.5 shows the numerical results of the sound attenuations of each receiver when the number of cylinders in z-direction increases from 3 rows to 6 rows. From figure 2.5 (a) we can see that when the receiver is at the nearest location from the sound source which is (9, 10) m, basically the sonic crystal with more cylinder barriers at z-direction has higher sound attenuations except several frequencies. And the cylinder array 3×6 has more sound attenuation peaks among the medium frequency from 250Hz to 750Hz than the other three arrays. From figure 2.5 (b) we can see that when the receiver is at location (10, 10) m, the cylinder array 3×4 has two remarkable sound attenuation peaks near the frequency 170Hz and 500Hz. When the frequency is relative high (from 700Hz to 1000Hz) the sound attenuation results become similar between 3×3 and 3×5, 3×4 and 3×6. From figure 2.5 (c) we can see that at location (11, 10) m, the cylinder array 3×4 also has a much higher sound

attenuation at frequency 350Hz than the other three arrays. When the receiver is at the furthest location (12, 10) m, the sound attenuations do not have many peaks during the medium frequency range as the three nearer receivers.

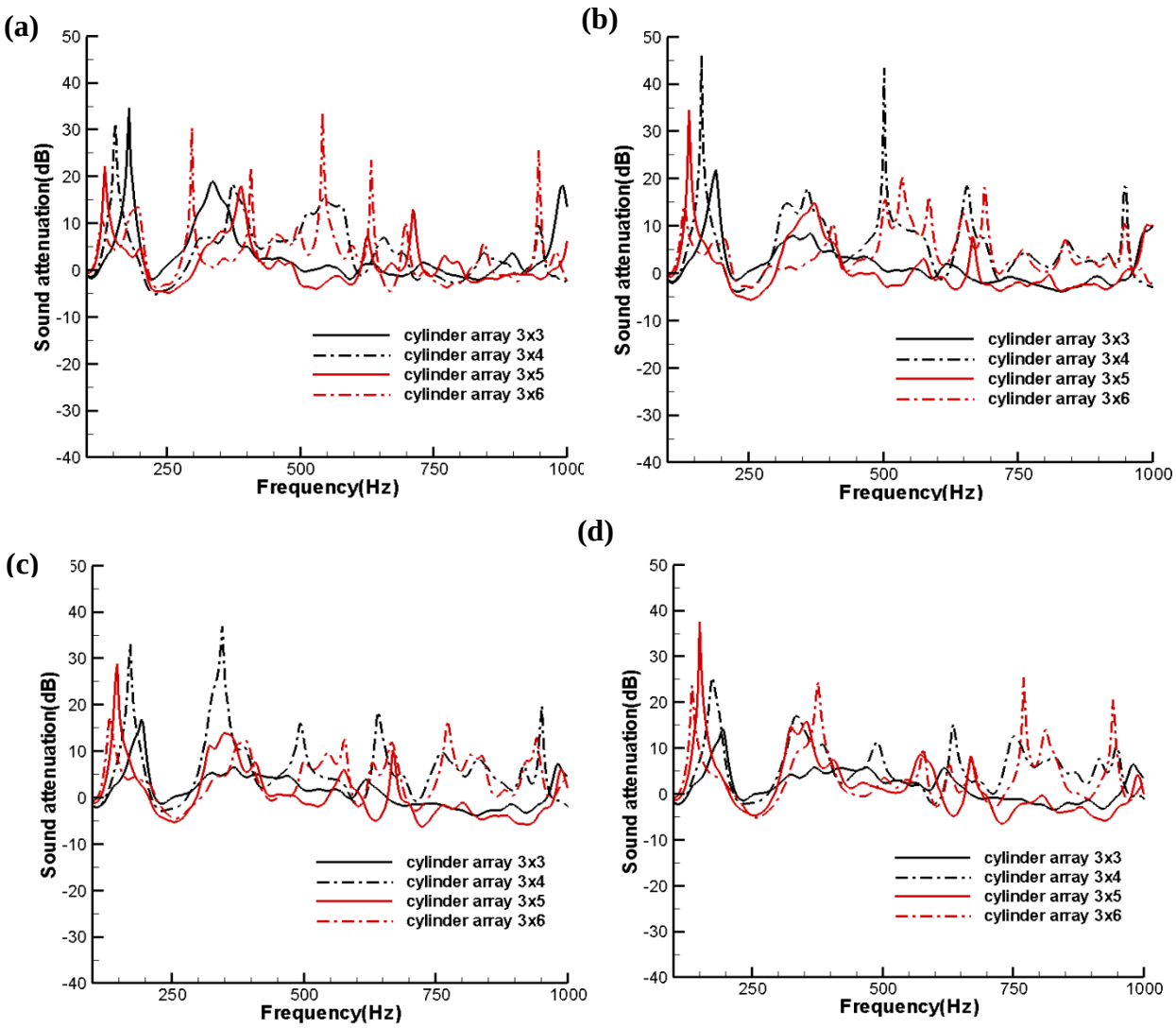

Fig. 2.5 Sound attenuations versus frequency (a) at the receiver (9, 10)m (b) at the receiver (10, 10)m (c) at the receiver (11, 10)m (d) at the receiver (12, 10)m

Combing all the numerical results of four different receivers above, it can be found that the sound attenuations are higher when the number of cylinder barriers in z-direction is even compared with odd, especially at relative high frequency (from 500Hz to 1000Hz).

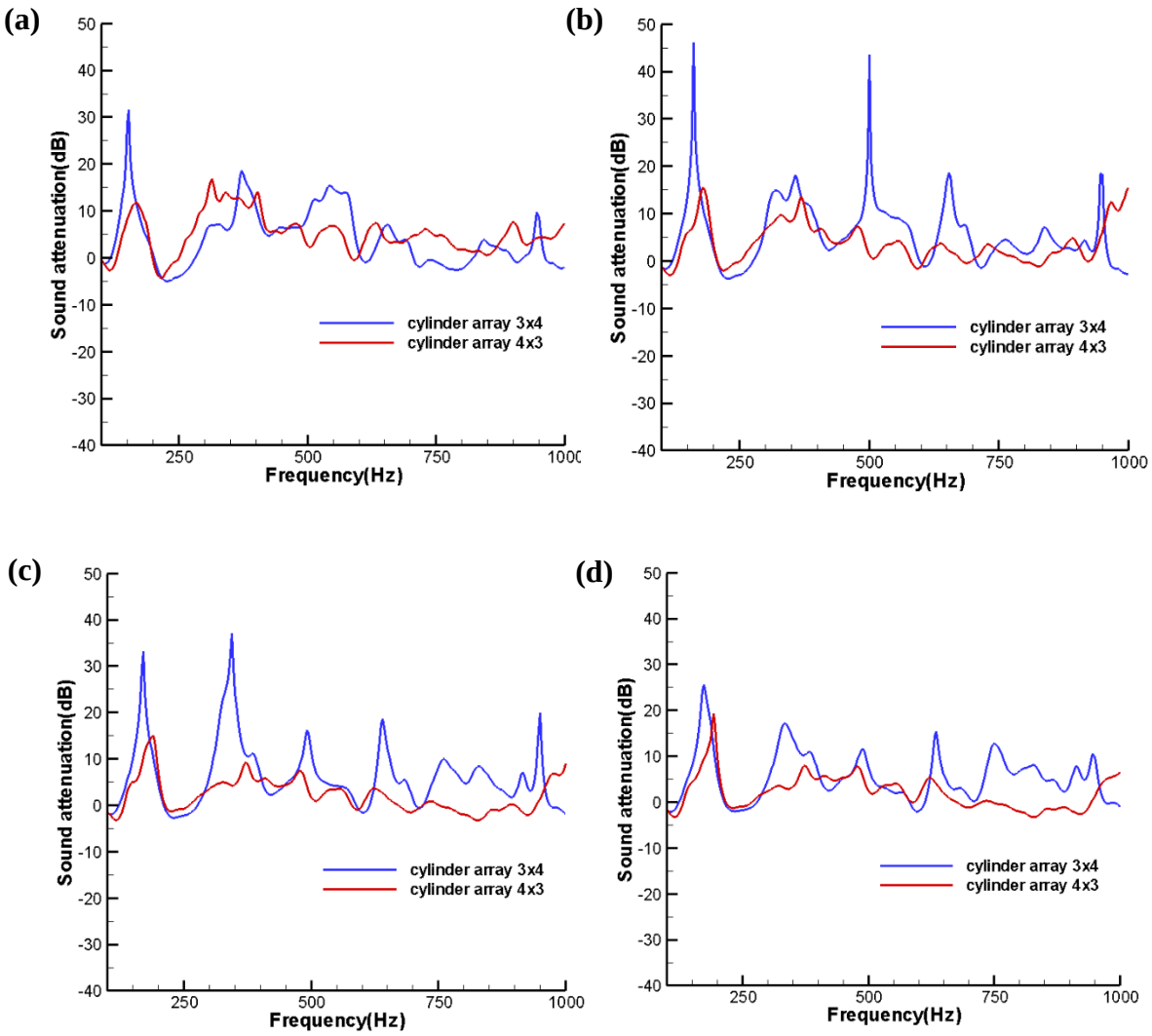

Fig. 2.6 Sound attenuations versus frequency comparison between transposed cylinder arrays (a) at the receiver (9, 10)m (b) at the receiver (10, 10)m (c) at the receiver (11, 10)m (d) at the receiver (12, 10)m

By comparing the numerical results from cylinders arrays 3×4 and 4×3, we can find the relation of sound attenuations between two inter-transposed arrays. Figure. 2.6 shows the numerical sound attenuations of four receivers of cylinder arrays 3×4 and 4×3. From 2.6 (a) we can see that for the nearest receiver (9, 10) m, the sound attenuation from cylinder array 3×4 is higher at relative low and high frequency than 4×3. The sound attenuation from cylinder array 4×3 is higher during the medium frequency than 3×4. From 2.6 (c) to (d) we can see that for the other three receivers the sound attenuations from cylinder array 4×3 are much higher than 3×4 except a few certain frequencies. Therefore even the incident wave is propagating in y-direction, the cylinder array 3×4 has much better sound blockage effect than 4×3 for the four different locations.

2.3 3D Numerical Model Description

2.3.1 Free Filed Simulation

The wave propagation through different cylinder arrays in free filed is also simulated for three-dimension. For this research, the three-dimensional Zwikker-Kosten equations in Ref. [95] of sound wave propagation are solved, and the finite-difference time-domain method coupled with immersed boundary method is applied. The parallel computing technique is also applied for three-dimensional simulations.

Combining the linearized Euler sound propagation equations in air with those equations in a porous media in the form of the Zwikker-Kosten equations in Ref. [95], we have:

$$\frac{\partial \mathbf{u}}{\partial t} + (\mathbf{u}_{av} \cdot \nabla)\mathbf{u} + (\mathbf{u} \cdot \nabla)\mathbf{u}_{av} = -\alpha_{av} \nabla p - \alpha \nabla p_{av} + f_{\mathbf{u}} \tag{2.2}$$

$$\frac{\partial p}{\partial t} + (\mathbf{u}_{av} \cdot \nabla) p + (\mathbf{u} \cdot \nabla) p_{av} = -\gamma p \nabla p - \gamma p_{av} (\nabla \cdot \mathbf{u}) + f_p \tag{2.3}$$

When the wave propagates through rigid cylinder barriers, the extra forced terms $f_{\mathbf{u}}$ and f_p from the immersed boundary method are applied:

$$f_{\mathbf{u}} = \begin{cases} 0 \quad \text{outside the porous media} \\ \alpha_{av}\nabla p + \alpha_{av}\nabla p + (\mathbf{u}_{av}\cdot\nabla)\mathbf{u} + \quad \text{inside the porous media} \\ \qquad (\mathbf{u}\cdot\nabla)\mathbf{u}_{av} - \dfrac{\Omega}{c_s}\alpha_{av}(\nabla p + \sigma\mathbf{u}) \end{cases} \tag{2.4}$$

$$f_p = \begin{cases} 0 \quad \text{outside the porous media} \\ \gamma p\nabla p + \gamma p_{av}(\nabla\cdot\mathbf{u}) + (\mathbf{u}_{av}\cdot\nabla)p + \quad \text{inside the porous media} \\ \qquad (\mathbf{u}\cdot\nabla)p_{av} - \dfrac{\gamma p_{av}}{\Omega}(\nabla\cdot\mathbf{u}) \end{cases} \tag{2.5}$$

In the above equations γ, c_s, Ω, σ, u_{av}, p_{av} and α_{av} are the specific heat ratio, porous media structure factor, porous media porosity, resistivity, time averaged background flow velocity, background pressure and specific volume respectively. In numerical simulations $\gamma = 1.4$, $c_s = 3.0$, $\Omega = 0.3$. The resistivity $\sigma = 4\times10^8$ Pa s m^{-2} which is a prohibitive high value and the cylinder barriers can be considered acoustic rigid. And the specific volume is defined as:

$$\alpha = -\frac{p}{\gamma p_{av}\rho_{av}} \tag{2.6}$$

The impulsive point sound source is given by:

$$p = e^{-40r^2} \tag{2.7}$$

where r is the distance from the sound source position.

Based on the PML boundary in Ref. [96] the PML boundary equations for three-dimension can be derived for three directions.

The PML boundary governing equations for x-direction is:

$$\frac{\partial u}{\partial t}+U_{av}\frac{\partial u}{\partial x}+V_{av}\frac{\partial u}{\partial y}+W_{av}\frac{\partial u}{\partial z}+u\frac{\partial U_{av}}{\partial x}+v\frac{\partial U_{av}}{\partial y}+w\frac{\partial U_{av}}{\partial z}+\alpha_{av}\frac{\partial p}{\partial x}$$
$$=-\sigma_x(u+V_{av}\frac{\partial q_u}{\partial y}+W_{av}\frac{\partial q_u}{\partial z}+q_u\frac{\partial U_{av}}{\partial x}+q_v\frac{\partial U_{av}}{\partial y}+q_w\frac{\partial U_{av}}{\partial z}) \tag{2.8}$$

$$\frac{\partial v}{\partial t}+U_{av}\frac{\partial v}{\partial x}+V_{av}\frac{\partial v}{\partial y}+W_{av}\frac{\partial v}{\partial z}+u\frac{\partial V_{av}}{\partial x}+v\frac{\partial V_{av}}{\partial y}+w\frac{\partial V_{av}}{\partial z}+\alpha_{av}\frac{\partial p}{\partial y}$$
$$=-\sigma_x(v+V_{av}\frac{\partial q_v}{\partial y}+W_{av}\frac{\partial q_v}{\partial z}+q_u\frac{\partial V_{av}}{\partial x}+q_v\frac{\partial V_{av}}{\partial y}+q_w\frac{\partial V_{av}}{\partial z}+\alpha_{av}\frac{\partial q_p}{\partial y}) \tag{2.9}$$

$$\frac{\partial w}{\partial t}+U_{av}\frac{\partial w}{\partial x}+V_{av}\frac{\partial w}{\partial y}+W_{av}\frac{\partial w}{\partial z}+u\frac{\partial W_{av}}{\partial x}+v\frac{\partial W_{av}}{\partial y}+w\frac{\partial W_{av}}{\partial z}+\alpha_{av}\frac{\partial p}{\partial z}$$
$$=-\sigma_x(w+V_{av}\frac{\partial q_w}{\partial y}+W_{av}\frac{\partial q_w}{\partial z}+q_u\frac{\partial W_{av}}{\partial x}+q_v\frac{\partial W_{av}}{\partial y}+q_w\frac{\partial W_{av}}{\partial z}+\alpha_{av}\frac{\partial q_p}{\partial z}) \tag{2.10}$$

$$\frac{\partial p}{\partial t}+U_{av}\frac{\partial p}{\partial x}+V_{av}\frac{\partial p}{\partial y}+W_{av}\frac{\partial p}{\partial z}+\gamma p(\frac{\partial U_{av}}{\partial x}+\frac{\partial V_{av}}{\partial y}+\frac{\partial W_{av}}{\partial z})+\gamma p_{av}(\frac{\partial u}{\partial x}+\frac{\partial v}{\partial y}+\frac{\partial w}{\partial z})$$
$$=-\sigma_x[p+V_{av}\frac{\partial q_p}{\partial y}+W_{av}\frac{\partial q_p}{\partial z}+\gamma q_p(\frac{\partial U_{av}}{\partial x}+\frac{\partial V_{av}}{\partial y}+\frac{\partial W_{av}}{\partial z})+\gamma p_{av}(\frac{\partial q_v}{\partial y}+\frac{\partial q_w}{\partial z})] \tag{2.11}$$

the PML boundary governing equations for y-direction is:

$$\frac{\partial u}{\partial t}+U_{av}\frac{\partial u}{\partial x}+V_{av}\frac{\partial u}{\partial y}+W_{av}\frac{\partial u}{\partial z}+u\frac{\partial U_{av}}{\partial x}+v\frac{\partial U_{av}}{\partial y}+w\frac{\partial U_{av}}{\partial z}+\alpha_{av}\frac{\partial p}{\partial x}$$
$$=-\sigma_y(u+U_{av}\frac{\partial q_u}{\partial x}+W_{av}\frac{\partial q_u}{\partial z}+q_u\frac{\partial U_{av}}{\partial x}+q_v\frac{\partial U_{av}}{\partial y}+q_w\frac{\partial U_{av}}{\partial z}+\alpha_{av}\frac{\partial q_p}{\partial x}) \tag{2.12}$$

$$\frac{\partial v}{\partial t}+U_{av}\frac{\partial v}{\partial x}+V_{av}\frac{\partial v}{\partial y}+W_{av}\frac{\partial v}{\partial z}+u\frac{\partial V_{av}}{\partial x}+v\frac{\partial V_{av}}{\partial y}+w\frac{\partial V_{av}}{\partial z}+\alpha_{av}\frac{\partial p}{\partial y}$$
$$=-\sigma_y(v+U_{av}\frac{\partial q_v}{\partial x}+W_{av}\frac{\partial q_v}{\partial z}+q_u\frac{\partial V_{av}}{\partial x}+q_v\frac{\partial V_{av}}{\partial y}+q_w\frac{\partial V_{av}}{\partial z}) \tag{2.13}$$

$$\frac{\partial w}{\partial t}+U_{av}\frac{\partial w}{\partial x}+V_{av}\frac{\partial w}{\partial y}+W_{av}\frac{\partial w}{\partial z}+u\frac{\partial W_{av}}{\partial x}+v\frac{\partial W_{av}}{\partial y}+w\frac{\partial W_{av}}{\partial z}+\alpha_{av}\frac{\partial p}{\partial z}$$
$$=-\sigma_y(w+U_{av}\frac{\partial q_w}{\partial x}+W_{av}\frac{\partial q_w}{\partial z}+q_u\frac{\partial W_{av}}{\partial x}+q_v\frac{\partial W_{av}}{\partial y}+q_w\frac{\partial W_{av}}{\partial z}+\alpha_{av}\frac{\partial q_p}{\partial z}) \tag{2.14}$$

$$\frac{\partial p}{\partial t}+U_{av}\frac{\partial p}{\partial x}+V_{av}\frac{\partial p}{\partial y}+W_{av}\frac{\partial p}{\partial z}+\gamma p(\frac{\partial U_{av}}{\partial x}+\frac{\partial V_{av}}{\partial y}+\frac{\partial W_{av}}{\partial z})+\gamma p_{av}(\frac{\partial u}{\partial x}+\frac{\partial v}{\partial y}+\frac{\partial w}{\partial z})$$
$$=-\sigma_y[p+U_{av}\frac{\partial q_p}{\partial x}+W_{av}\frac{\partial q_p}{\partial z}+\gamma q_p(\frac{\partial U_{av}}{\partial x}+\frac{\partial V_{av}}{\partial y}+\frac{\partial W_{av}}{\partial z})+\gamma p_{av}(\frac{\partial q_u}{\partial x}+\frac{\partial q_w}{\partial z})] \quad (2.15)$$

the PML boundary governing equations for z-direction is:

$$\frac{\partial u}{\partial t}+U_{av}\frac{\partial u}{\partial x}+V_{av}\frac{\partial u}{\partial y}+W_{av}\frac{\partial u}{\partial z}+u\frac{\partial U_{av}}{\partial x}+v\frac{\partial U_{av}}{\partial y}+w\frac{\partial U_{av}}{\partial z}+\alpha_{av}\frac{\partial p}{\partial x}$$
$$=-\sigma_z(u+U_{av}\frac{\partial q_u}{\partial x}+V_{av}\frac{\partial q_u}{\partial y}+q_u\frac{\partial U_{av}}{\partial x}+q_v\frac{\partial U_{av}}{\partial y}+q_w\frac{\partial U_{av}}{\partial z}+\alpha_{av}\frac{\partial q_p}{\partial x}) \quad (2.16)$$

$$\frac{\partial v}{\partial t}+U_{av}\frac{\partial v}{\partial x}+V_{av}\frac{\partial v}{\partial y}+W_{av}\frac{\partial v}{\partial z}+u\frac{\partial V_{av}}{\partial x}+v\frac{\partial V_{av}}{\partial y}+w\frac{\partial V_{av}}{\partial z}+\alpha_{av}\frac{\partial p}{\partial y}$$
$$=-\sigma_z(v+U_{av}\frac{\partial q_v}{\partial x}+V_{av}\frac{\partial q_v}{\partial y}+q_u\frac{\partial V_{av}}{\partial x}+q_v\frac{\partial V_{av}}{\partial y}+q_w\frac{\partial V_{av}}{\partial z}+\alpha_{av}\frac{\partial q_p}{\partial y}) \quad (2.17)$$

$$\frac{\partial w}{\partial t}+U_{av}\frac{\partial w}{\partial x}+V_{av}\frac{\partial w}{\partial y}+W_{av}\frac{\partial w}{\partial z}+u\frac{\partial W_{av}}{\partial x}+v\frac{\partial W_{av}}{\partial y}+w\frac{\partial W_{av}}{\partial z}+\alpha_{av}\frac{\partial p}{\partial z}$$
$$=-\sigma_z(w+U_{av}\frac{\partial q_w}{\partial x}+V_{av}\frac{\partial q_w}{\partial y}+q_u\frac{\partial W_{av}}{\partial x}+q_v\frac{\partial W_{av}}{\partial y}+q_w\frac{\partial W_{av}}{\partial z}) \quad (2.18)$$

$$\frac{\partial p}{\partial t}+U_{av}\frac{\partial p}{\partial x}+V_{av}\frac{\partial p}{\partial y}+W_{av}\frac{\partial p}{\partial z}+\gamma p(\frac{\partial U_{av}}{\partial x}+\frac{\partial V_{av}}{\partial y}+\frac{\partial W_{av}}{\partial z})+\gamma p_{av}(\frac{\partial u}{\partial x}+\frac{\partial v}{\partial y}+\frac{\partial w}{\partial z})$$
$$=-\sigma_z[p+U_{av}\frac{\partial q_p}{\partial x}+V_{av}\frac{\partial q_p}{\partial y}+\gamma q_p(\frac{\partial U_{av}}{\partial x}+\frac{\partial V_{av}}{\partial y}+\frac{\partial W_{av}}{\partial z})+\gamma p_{av}(\frac{\partial q_u}{\partial x}+\frac{\partial q_v}{\partial y})] \quad (2.19)$$

For an effective PML domain, a grid stretching in the layer of z-direction:

$$\frac{\partial}{\partial z}\rightarrow\frac{1}{\beta(z)}\frac{\partial}{\partial z} \quad (2.20)$$

where $\beta(z)\geq 1$ represents the smooth function:

$$\beta(z)=1+A\left|\frac{z-z_{\max}}{D}\right|^s \quad (2.21)$$

for an effective PML domain, a grid stretching in the layer of y-direction:

$$\frac{\partial}{\partial y}\rightarrow\frac{1}{\beta(y)}\frac{\partial}{\partial y} \quad (2.22)$$

where $\beta(y)\geq 1$ represents the smooth function:

$$\beta(y) = 1 + A\left|\frac{y - y_{\max}}{D}\right|^{s} \tag{2.23}$$

a grid stretching in the layer of x-direction:

$$\frac{\partial}{\partial x} \to \frac{1}{\beta(x)}\frac{\partial}{\partial x} \tag{2.24}$$

where $\beta(x) \geq 1$represents the smooth function:

$$\beta(x) = 1 + A\left|\frac{x - x_{\max}}{D}\right|^{s} \tag{2.25}$$

where D is the thickness of PML boundary, and the parameters A and s are chosen as A=25, s=2.

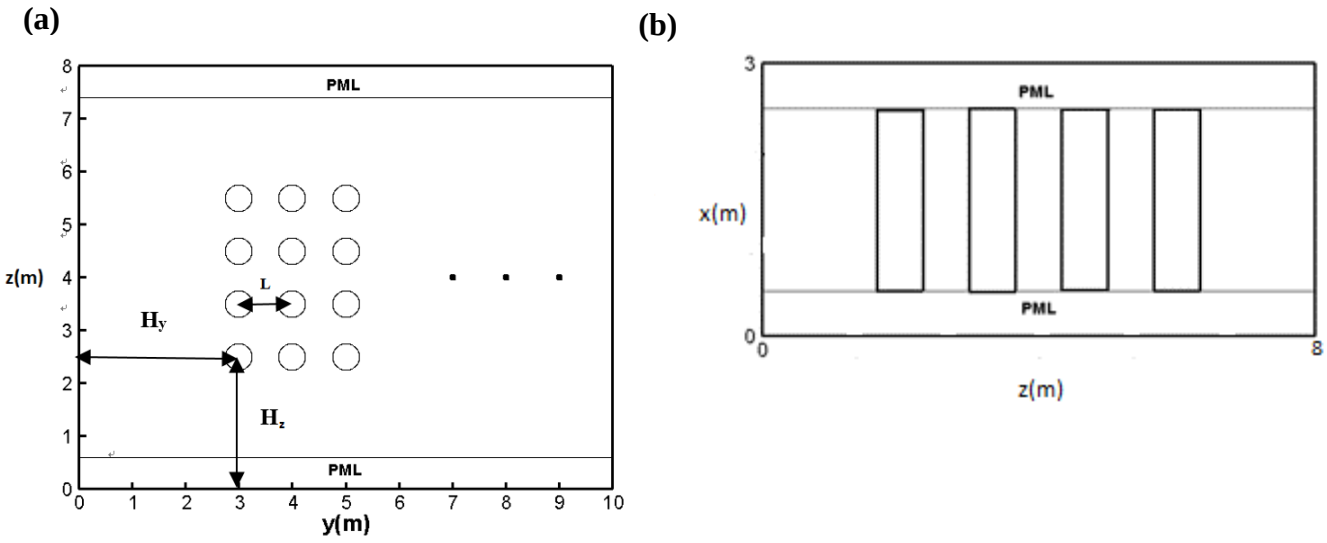

Fig. 2.7 Graphic illustration for 3D simulation geometry (a) yz-plane (b) xz-plane.

For three-dimensional sound wave propagation through sonic crystals, four different arrays are studied: 3×3, 3×4, 3×5 and 4×3. The computational domain has the dimension of $y = 10m$, $x = 3m$. The z-direction length is $z = 6m$ for the case of cylinder arrays 3×3 and 4×3, and is $z = 8m$ for the

case of cylinder arrays 3×4 and 3×5. A uniform mesh size of $0.008m$ in each direction. The radius and height of cylinder barriers is 0.25m and 1.8m, $x\in[0.6,2.4]$m, and the square lattice distance L=1m. The point sound source is set at the center of the y=0 plane, and three receivers are located at different distances from the source. Their corresponding coordinates are $(1.5,7,3)$, $(1.5,8,3)$, $(1.5,9,3)$ for the case of cylinder arrays 3×3 and 4×3, and $(1.5,7,4)$, $(1.5,8,4)$, $(1.5,9,4)$ for the case of cylinder arrays 3×4 and 3×5. The time step $\Delta t=2.5\times10^{-6}s$ and total simulation time is 27.5ms. The PML boundary conditions are specified with thickness 0.6m at the six surfaces of the domain for the cases to achieve free field. Figure 2.6 shows the geometry of the three-dimension simulation domain when cylinder barriers array is 3×4.

Table 2.2 illustrates the locations of the cylinders for each case, where the parameters Hz and Hy are the distances that are shown in figure 2.6:

Table 2-2 Parameters of different cylinder barriers array for 3D simulations

Cylinder array	H_z (m)	H_y (m)
3×3	2	3
3×4	2.5	3
3×5	2	3
4×3	2	3

Figure. 2.8 and 2.9 are the pressure contours of each cylinder arrays simulation at x-plane and z-plane. Figure. 2.8 shows the pressure distributions at the moment t=5ms that the incident sound wave starts to reach the cylinder barriers, and figure 2.9 shows the pressure distributions at the moment t=15ms that the wave almost passed through the cylinder arrays. We can clearly see the reflected wave and interactions between the cylinders.

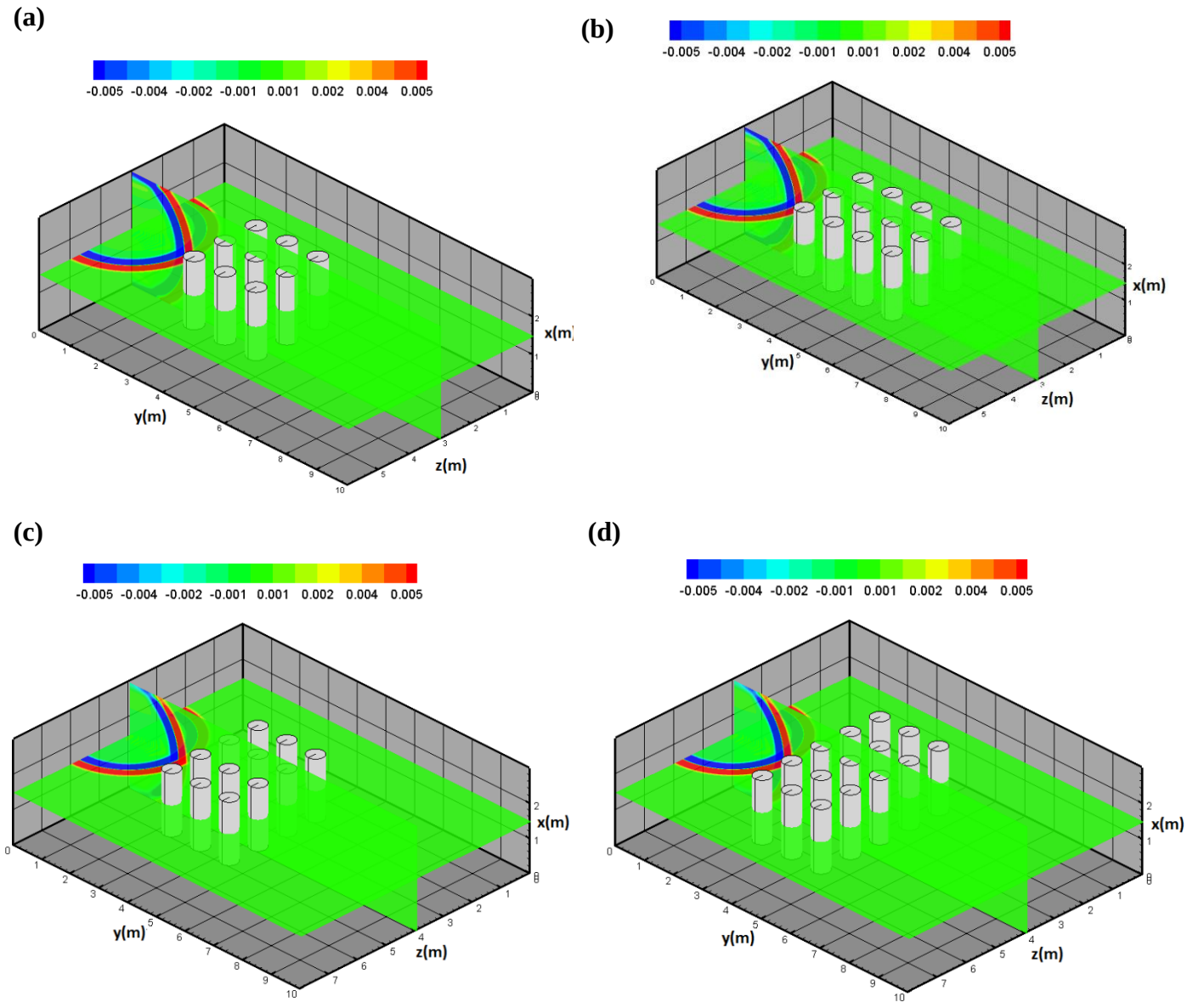

Fig. 2.8 Pressure contours at the moment t=5ms (a) 3x3 cylinders (b) 4x3 cylinders (c) 3x4 cylinders (d) 3x5 cylinders

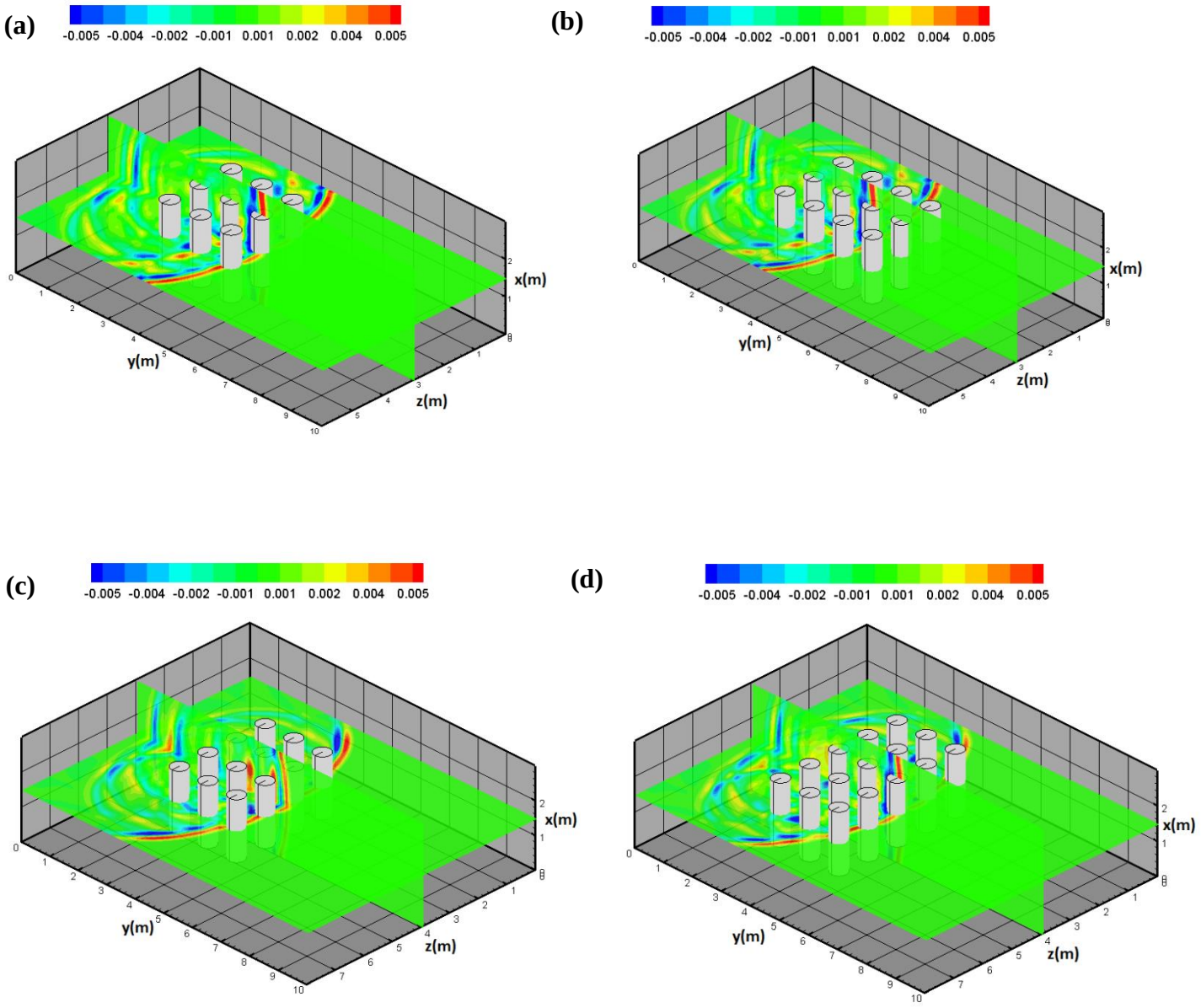

Fig. 2.9 Pressure contours at the moment t=15ms (a) 3x3 cylinders (b) 4x3 cylinders (c) 3x4 cylinders (d) 3x5 cylinders

The simulated sound attenuations of the three different receivers are given in Fig. 2.10 for each of the cylinder arrays. First of all, we can see that the farthest receiver which is at 9m away from the sound source has the highest sound attenuation than the other two receivers. When the cylinder array is 3×3 or 4×3, the farthest receiver has an attenuation peak at around frequency 350Hz, after which the sound attenuation curve decreases gradually. The simulation results of three receivers are quite similar between the two different cylinder arrays of 3×3 and 4×3. The sound attenuation of the nearest receiver which is 7m away from the sound source is much higher than the receiver at 8m at low and high frequencies, and the receiver at 8m has higher sound attenuation than the receiver at 7m at the medium frequency range.

When the cylinder array is 3×4 or 3×5 the farthest receiver also has the best sound blockage effect than the other two receivers as discussed above. However, the relative levels between the two receivers at 7m and 8m are opposite for these two cylinder arrays. For the cylinder array 3×4 the sound attenuation of receiver at 8m is slightly higher than the receiver at 7m except for several high frequencies. For the cylinder array 3×5 the sound attenuation of receiver at 8m is higher than the receiver at 7m at all the frequency range. And the sound attenuation of the receiver at 7m is below zero except for high frequencies, which means the cylinder arrays strengthens the sound pressure level instead of diminishing.

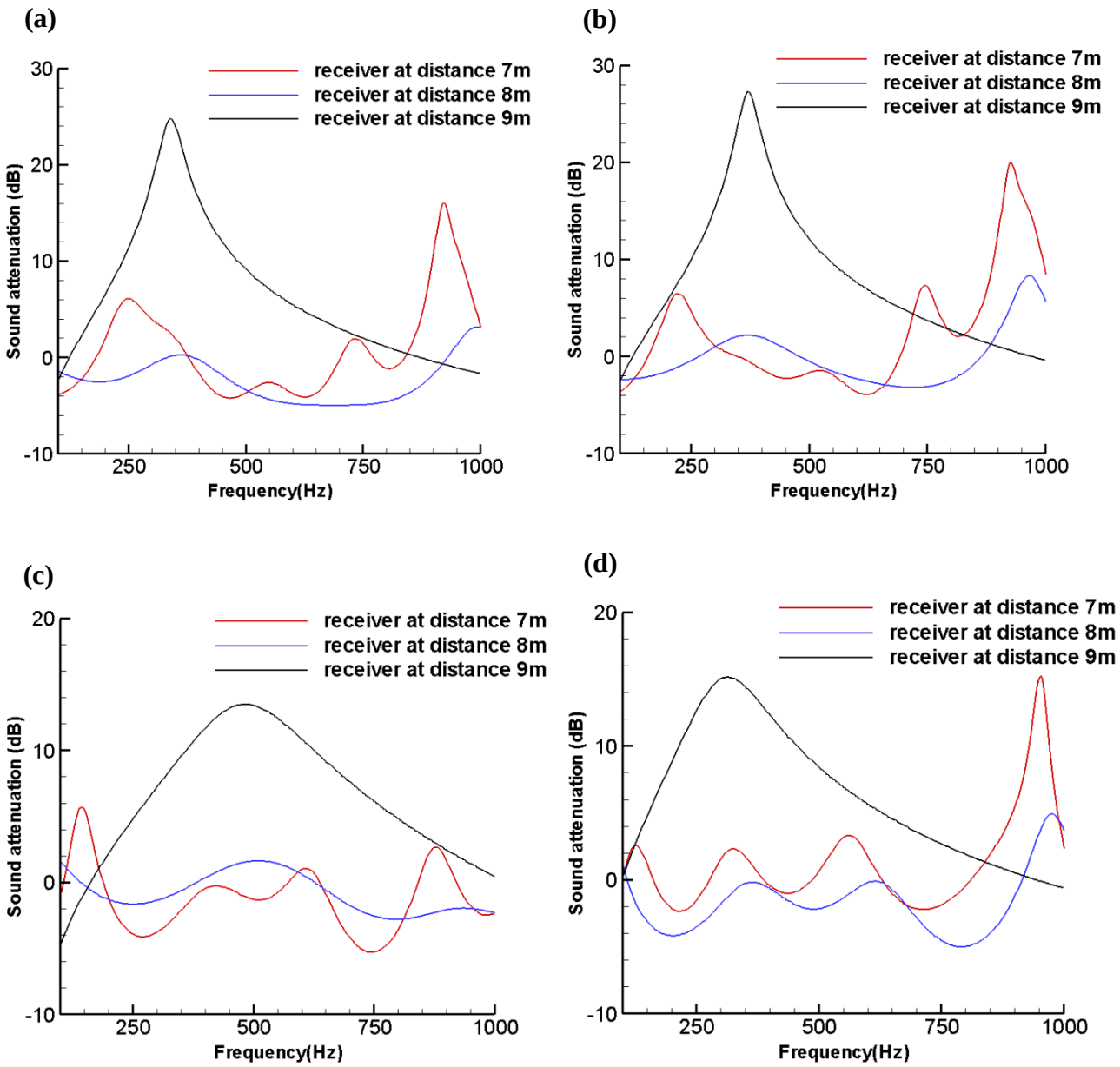

Fig. 2.10 3D sound attenuations versus frequency for three receivers

(a) 3x3 cylinders (b) 4x3 cylinders (c) 3x4 cylinders (d) 3x5 cylinders

When the number of cylinder barriers in y-direction is fixed as 3, the effect of increasing cylinder barriers at z-direction is also studies like the 2D simulations. Figure. 2.10 shows the numerical results of sound attenuations of cylinder arrays 3×3, 3×4 and 3×5.

When the receiver is at the nearest location 7m, the relation of three different simulation results is changing disorderly as the frequency increasing. For low frequency (100Hz to 350Hz), the cylinder array 3×3 has higher sound attenuation. Then the sound attenuation reaches the lowest values during medium frequency (350Hz to 700Hz). After that it becomes the highest again. The highest sound attenuation is obtained at high frequency for cylinder arrays 3×3 and 3×5, while at very low frequency for cylinder array 3×4.

When the receiver is at location 8m, the sound attenuation values are similar for the three different arrays. And the values are small, even below zero, which means the sound blockage effects of these three cylinder arrays are not good for this location.

When the receiver is at the farthest location 9m and the frequency is lower than 500Hz, the sound attenuation increases as the number of cylinders increasing. And we can see that when the frequency is greater than 500Hz, the sound attenuations of three cylinder arrays are gradually decreasing as the frequency is increasing, which means the sound blockage effect of sonic crystal becomes weak at high frequency.

The sound attenuation comparison between transposed cylinder arrays is also studied for 3D simulations. Figure. 2.12 shows the comparison between cylinder arrays 3×4 and 4×3 for the three receivers. From figure 2.12 (a) we can see that the cylinder array 4×3 has much higher sound attenuation than 3×4 at high frequency at location 7m. From figure 2.12 (b) we can see the sound attenuation values are similar for the two transposed arrays at 8m. And the values are fluctuating near zero, which means both of two cylinder arrays cannot diminish the sound pressure level at

this location. From figure 2.12 (c) we can see that the cylinder array 4×3 has much higher sound attenuation than 3×4 at frequency relative low frequency. The sound attenuation of array 4×3 has a peak at frequency about 400Hz.

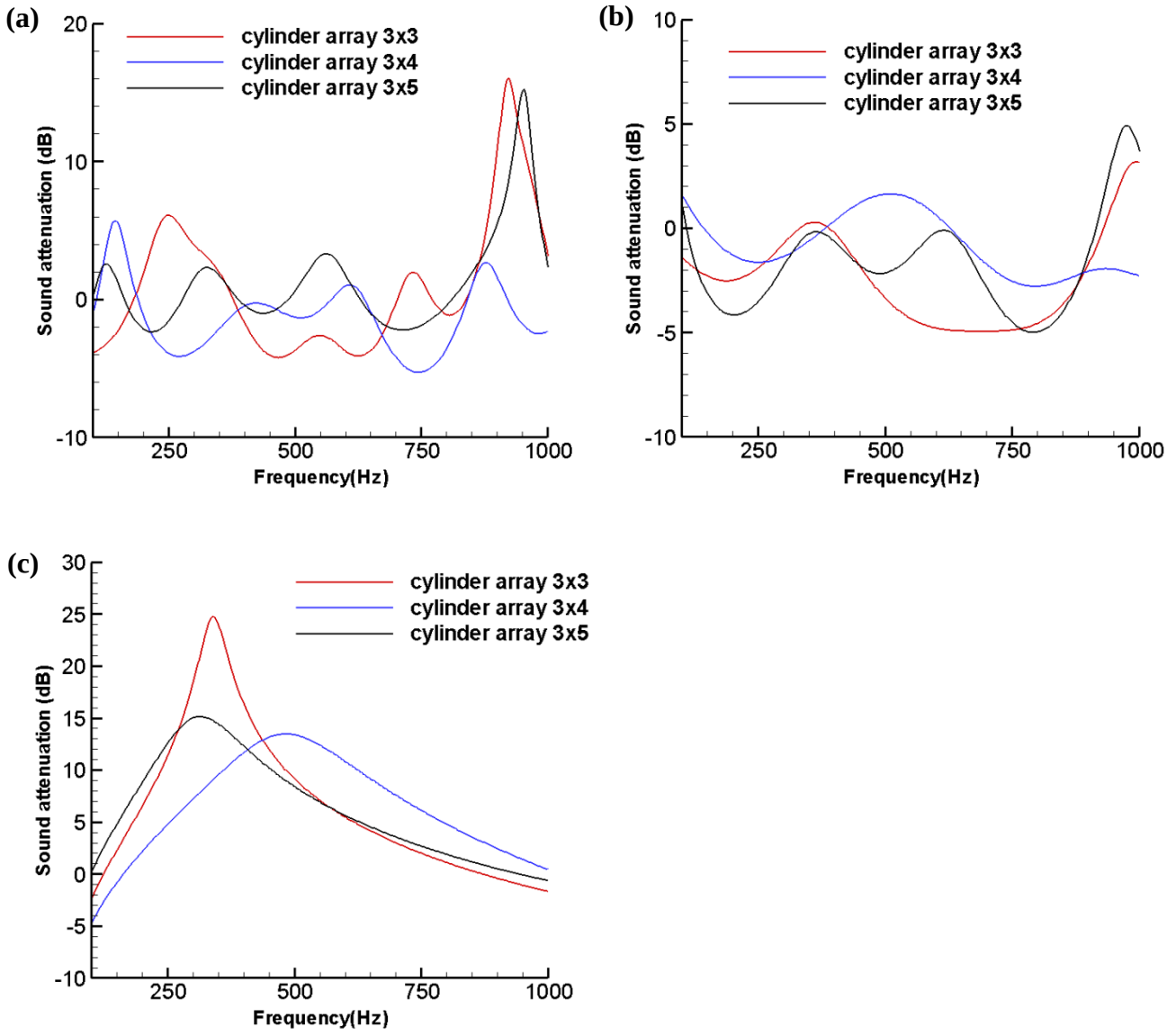

Fig. 2.11 3D sound attenuations versus frequency for different cylinder arrays (a) receiver at 7m (b) receiver at 8m (c) receiver at 9m

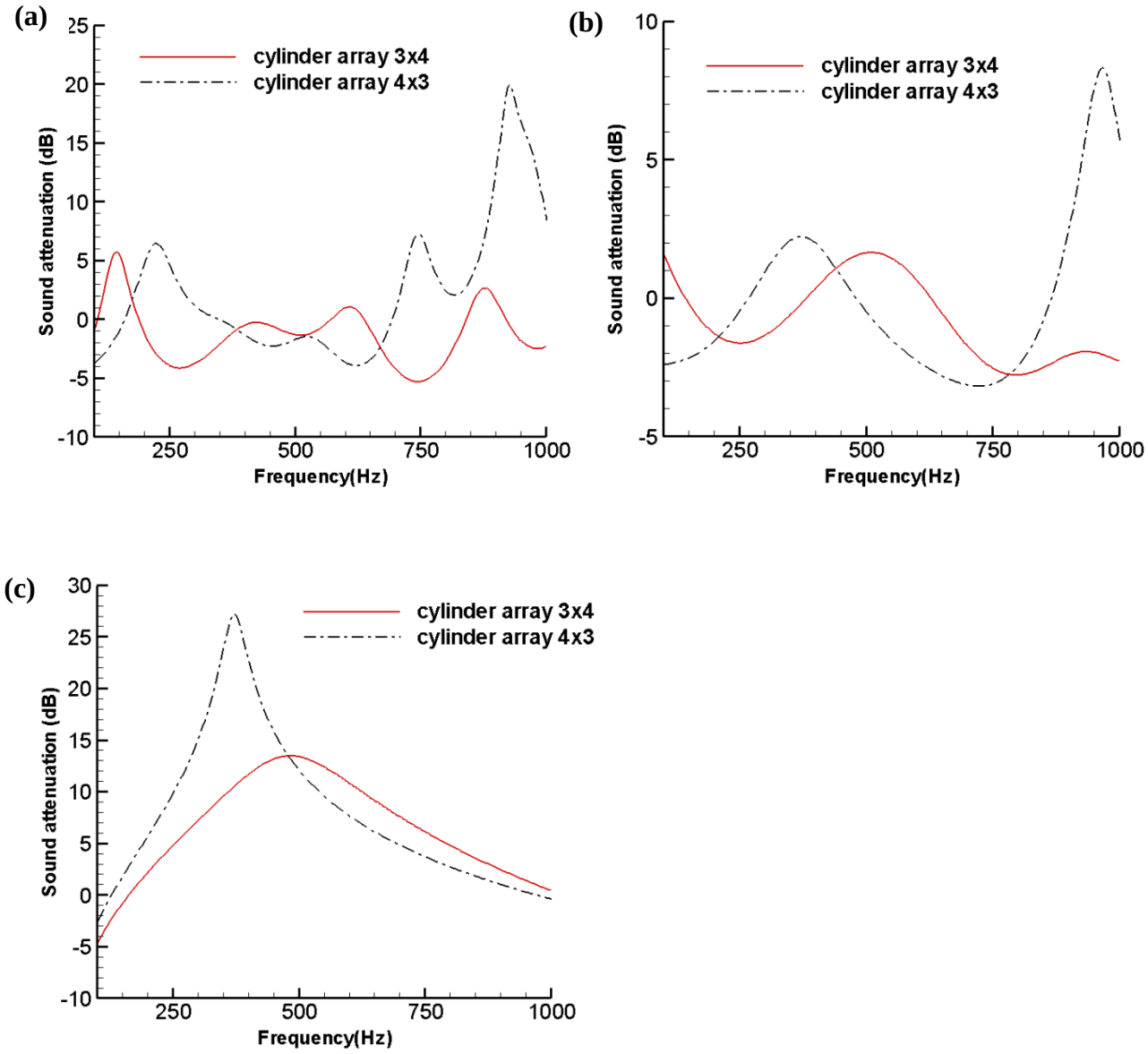

Fig. 2.12 3D sound attenuations versus frequency for transposed cylinder arrays (a) receiver at 7m (b) receiver at 8m (c) receiver at 9m

2.3.2 Ground Effect Simulations with Moving Zonal-Domain Method

Besides the study of sound blockage effect of sonic crystals in free filed, the 3D simulations with rigid ground influence are also discussed in this section.

For three-dimensional sound wave propagation through cylinder arrays with rigid ground effect, the cylinder array is chosen as 3×3. The computational domain z-direction length $z = 6m$ and the height x-direction length $x = 6m$. Uniform mesh is used for simulations and the grid size $\Delta x = \Delta y = \Delta z = 0.008m$. The radius and height of cylinder barriers is 0.2m and 1.5m, $x \in [0,1.5]$ m, and the square lattice distance L=0.5m. The coordinate of point sound source is at $(1.5,0,3)$, and four farther receivers are chosen compare with the free filed simulations. The coordinates of the four receivers are $(1.5,10.5,3)$, $(1.5,11,3)$, $(1.5,11.5,3)$ and $(1.5,12,3)$. Time step is the same as the simulations in free field that $\Delta t = 2.5\times10^{-6}s$ and total simulation time is 37.5ms. The PML boundary conditions are specified with thickness 1m at front, back, left and top surface. The illustration of the geometry for this simulation is in figure 2.13. For the study in this section, we need to simulate the wave propagation in long distance to reach the four receivers, and the moving zonal-domain approach in Ref. [97] is implemented.

This method is to move the computational domain with the acoustic wave. First, the size of the domain needs to be small so that the computational efficiency and be greatly improved. Meanwhile the domain should also be large enough to contain a dispersing pulse and the energy should be confined within the computational domain. Figure. 2.11 is an illustration of the moving domain method. The incident wave with initial pressure distribution, propagates until arriving at a distance from the right boundary, preferably near the center of the moving domain to minimize the boundary effect in Ref. [97]. Then the moving domain starts moving a certain distance at the same direction as the wave propagation.

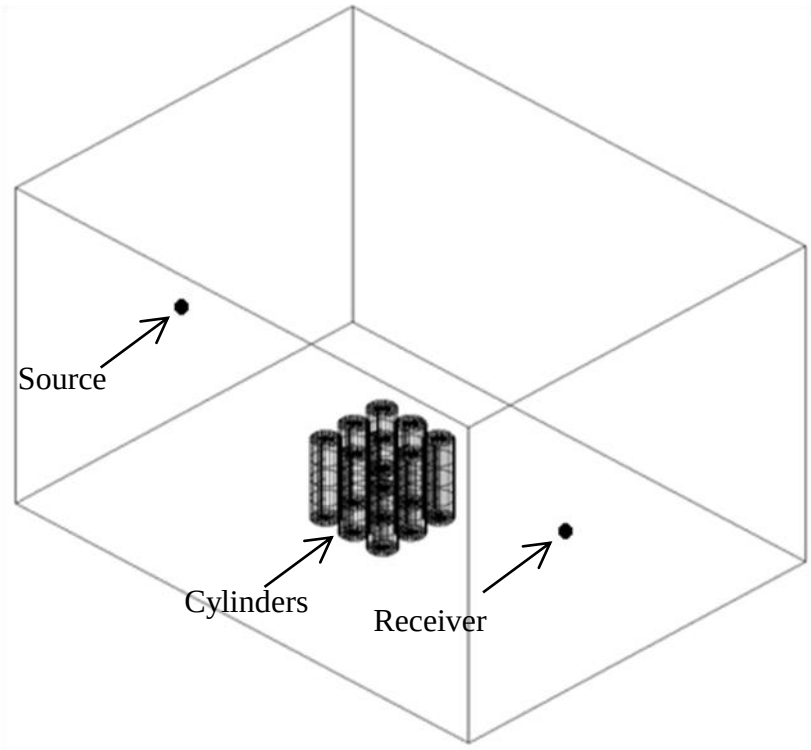

Fig. 2.13 Geometry of sound propagation through 3*3 sonic crystal with rigid ground.

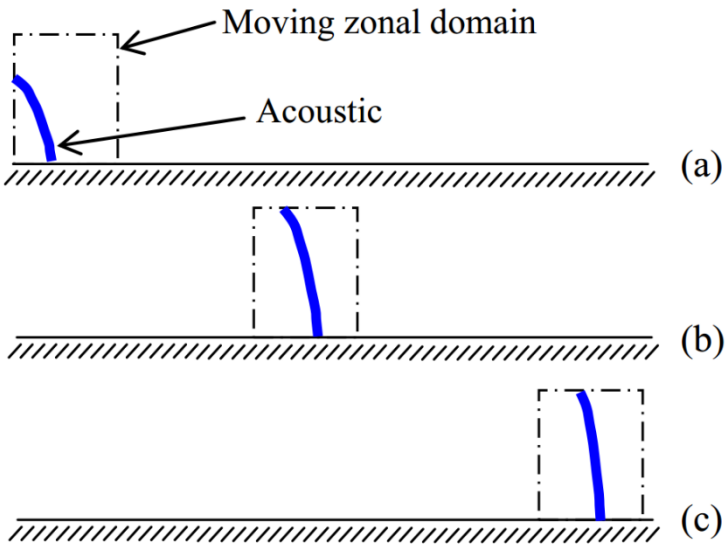

Fig. 2.14 Illustration of the moving domain method.

For the three-dimensional simulations in this section, two different moving domain scale in moving direction is used, one is 4m and the other is 5m. The simulation results with moving domain approach are also compared with the results simulated with fixed integral domain.

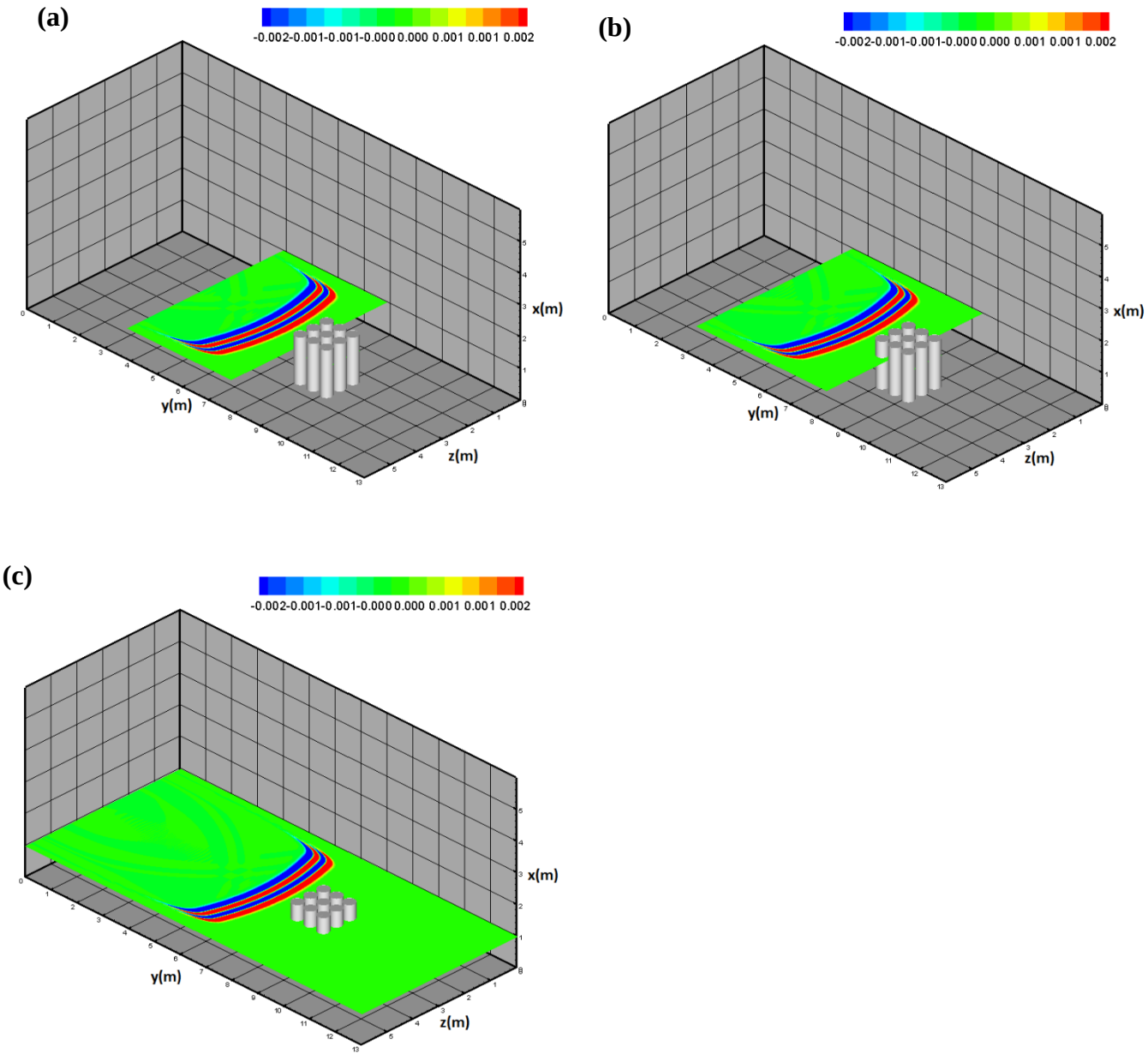

Fig. 2.15 Pressure contours at the moment t=20ms (a) moving domain with length 4m (b) moving domain with length 5m (c) non-moving domain

Figure. 2.15 shows the pressure contours of the non-moving domain simulation and the moving domain with two different length simulations at moment t=20ms. We can find that there is a wave following the incident wave, which is the reflected sound wave generated by the rigid ground.

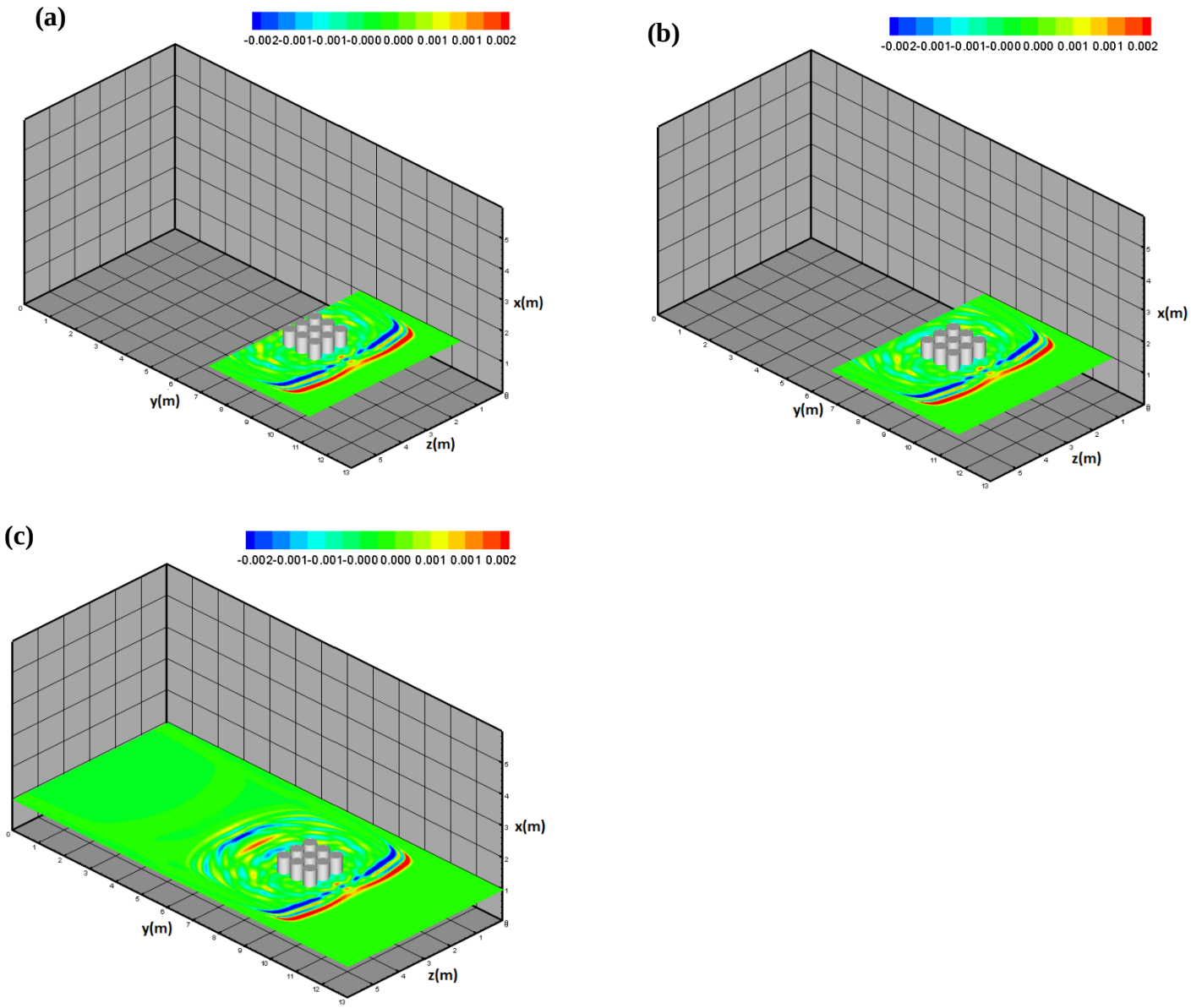

Fig. 2.16 Pressure contours at the moment t=30ms (a) moving domain with length 4m (b) moving domain with length 5m (c) non-moving domain

Figure. 2.16 shows the pressure contours of the non-moving domain simulation and the moving domain with two different length simulations at moment t=30ms. The graphs clearly show how the incident wave and the reflected wave from rigid ground are reflecting among the cylinder barriers and the interactions between the reflected waves. When the moving domain approach is used, we can see that part of the data are dumped at the area before the cylinder barriers. In contrast the non-moving simulation keeps all the data, from figure. 2.16 (c) we can see the intact reflected waves that are propagating towards back. However the wave that propagates through the cylinder arrays are kept completely in moving domain simulations and are just the same as the wave in non-moving domain. Therefore the moving domain method is feasible for the simulations of the certain locations that we are interested in.

Figure. 2.17 gives the numerical sound attenuations of the four receivers, and also the comparison between moving domain and non-moving domain. First of all, we can see that for all the four receivers, they all have the first sound attenuation peak at the frequency around 340Hz. Based on the theoretical Bragg's diffraction law $f = \frac{c}{2L}$ in Ref. [89], and the sonic crystal lattice distance $L = 0.5\text{m}$, we have the Bragg band gap frequency is $f = \frac{340}{2 \times 0.5} = 340\text{Hz}$, which matches with the numerical results well just like the two-dimensional simulations. In another word we know that the rigid ground does not have great influence on the band gap frequency in these three-dimensional simulations. By observing the magnitude of sound attenuation at the band gap frequency, we find that the nearest receiver which is 10.5m away from the source has the sound attenuation about 10dB at the band gap frequency, and the furthest receiver which is 12m away from the source has the sound attenuation about 23dB at the band gap frequency. Another conclusion can be drawn that when the receiver if further, the magnitude of sound attenuation at

band gap frequency is higher. When the receivers are 11m and 11.5m away, they also have another sound attenuation peak at high frequency about 1500Hz, but the sound attenuation of the furthest receiver is much lower at the same frequency than the other three. The values are even below zero, which means the sonic crystal is ineffective for sound blockage for high frequency sound wave at this location.

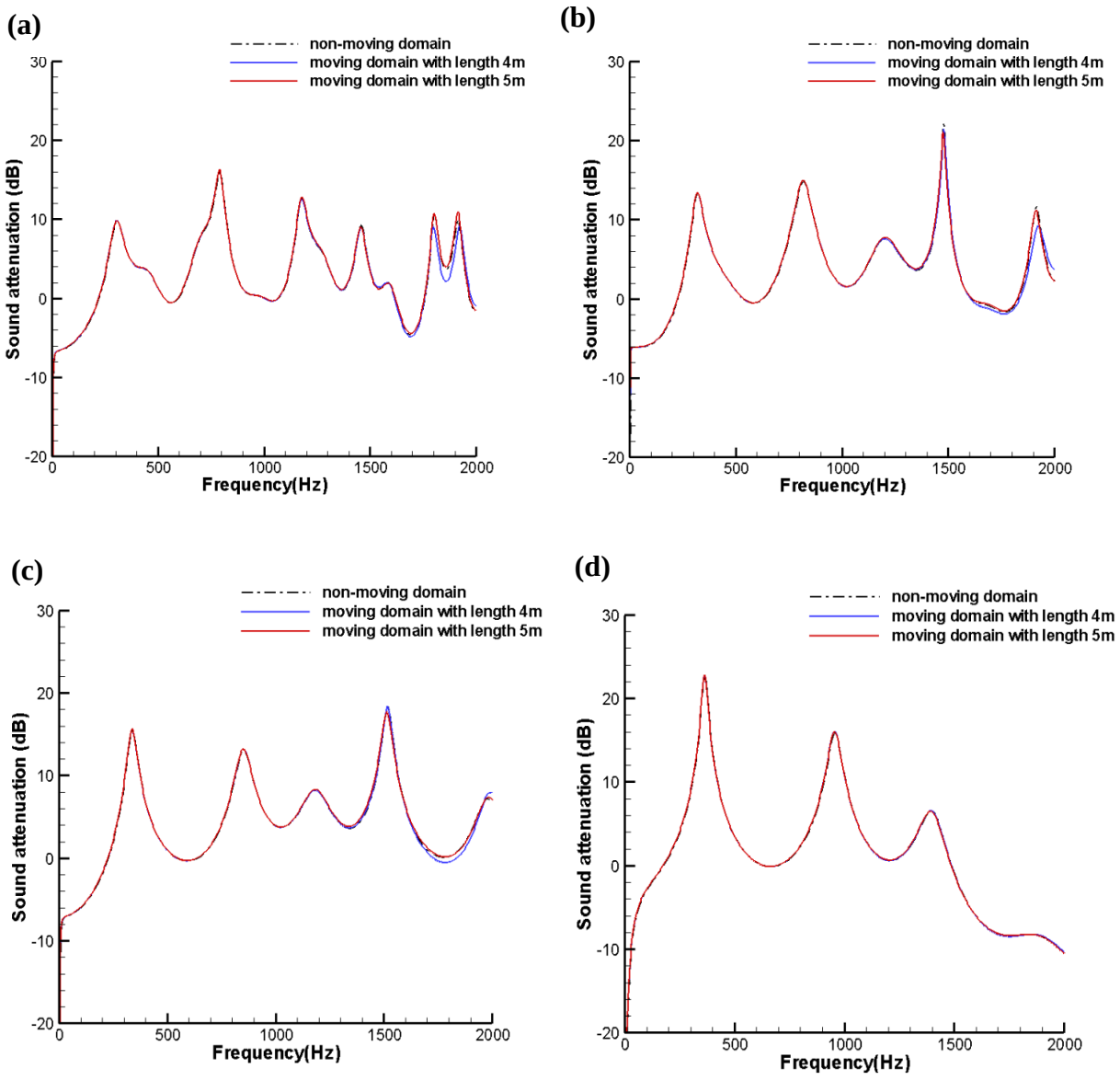

Fig. 2.17 Sound attenuations versus frequency for four receivers

(a) (3, 10.5, 1.5) (b) (3, 11, 1.5) (c) (3, 11.5, 1.5) (d) (3, 12, 1.5)

From the results comparison between moving domain and non-moving domain in figure. 2.17, we can find that for all the four receivers, at relative low and medium frequency the numerical sound attenuations from moving domain match extremely well with the results of non-moving domain, the three curves are almost identical.

Figure. 2.17 (a)-(c) show that when the receivers are at location (1.5, 10.5, 3), (1.5, 11, 3) and (1.5, 11.5, 3), at high frequency (higher than 1500Hz), the numerical result of moving domain with length 5m is still the same as the result of non-moving domain, but the result of moving domain with length 4m has slightly difference with the other two. And the greater the distance between the receiver and the cylinder barriers, the smaller the difference is. One main reason to explain this discrepancy is that moving domain method is dumping parts of the data while the domain is marching forward. Thus several small wave reflections and interactions between cylinders or between cylinders and receivers that are shown in figure. 2.16 (c) are no longer exist. When frequency is high, which means the time interval is short, the results from moving domain method is slightly different with the non-moving domain because a number of wave reflections that happened in short time are lost in moving domain.

Another factor can influence the accuracy is the moving domain size. When the moving domain size is small, which means the space left between the wave and cylinders is not big enough, consequently the data is not complete enough. When the domain size increases, the results of moving domain match much better with the results of fixed domain.

2.3.2 Simulations Based on Published Experiment

In this section, the three-dimensional simulations are conducted based on an experiment for sonic crystals in Ref. [88], [93] and [94]. The experiment consists of sound wave propagating through only one array of five rigid cylinders. The outer diameter of cylinder is 3cm and distance between the centers of cylinders in the sound propagation direction is 8.5cm. The height of the cylinders is 25cm. A speaker (Philips FWB-MX970RS) was used as the sound source in Ref. [88]. The distance between the speaker and first cylinder was 80cm so that the wave front that interacts with cylinder is close to a plane wave front and sound propagation is unidirectional. Acoustics foam was also used in regions around the source and receiver to prevent the reflections. The microphone which was used as a receiver was kept at a distance of 10cm from the last cylinder. The sound pressure level obtained from the microphone was averaged 50 times to obtain a consistent experimental reading, and this process is performed over a range of frequencies from 500Hz to 6000Hz at a frequency step of 3.5Hz in Ref. [88].

For our corresponding three-dimensional numerical simulations, the computational domain has a size of $z \in [0, 0.0425]m$, $y \in [0,1.74]m$ and $x \in [0, 0.25]m$. A uniform mesh size is implemented as 0.5mm in all the directions of the grid. The rigid cylinders are used as the sonic crystal, and the radius and height of cylinder barriers are 1.5cm and 25cm. The sound source is a periodic plane wave at the left boundary $y = 0$. The expression of the sound source is:

$$p = \sin(2\pi ft)$$

where f is the sound wave frequency. Since the sound attenuation results are relative values, we take the magnitude of plane sound wave as 1. We test five different sound source frequencies 1500Hz, 2000Hz, 3500Hz, 4000Hz and 5000Hz according to the approach used for the sound

source in the experiment in Ref. [88]. For the highest frequency 5000Hz, the corresponding wave length is:

$$\lambda = \frac{c}{f} = \frac{340}{5000} = 0.068\text{m}=68\text{mm}$$

And this smallest wave length value is 136 times of the mesh size used for simulations, thus the mesh revolution is valid for the high sound frequency. The time step $\Delta t = 2.5\times10^{-7}$s and simulation time domain t=7.5ms. According to the sonic crystals described in Ref. [88], the coordinates of the centers of the five cylinders at x=0 plane are (0cm, 80cm, 2.125cm), (0cm, 88.5cm, 2.125cm), (0cm, 97cm, 2.125cm), (0cm, 102.5cm, 2.125cm) and (0cm, 114cm, 2.125cm). The top, bottom, back and front side walls are set as rigid boundaries, and the PML boundary is set at the west surface as the acoustic foam in experiment, with a thickness 30cm.

Figure. 2.18 gives the illustration of part of the geometry in yz-plane.

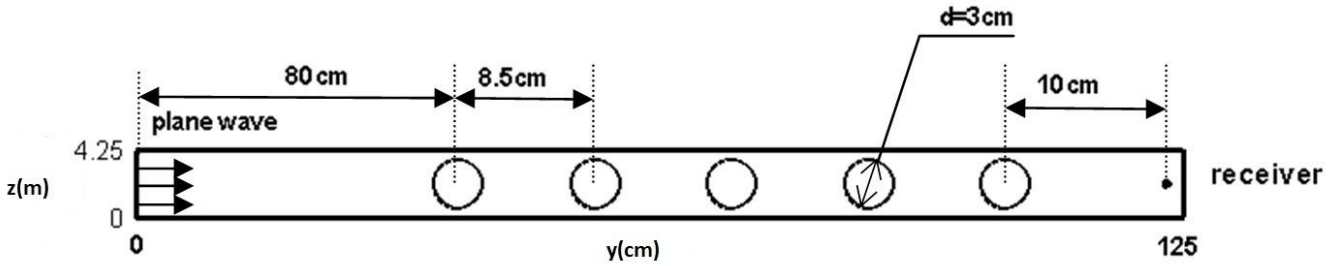

Fig. 2.18 Illustration of simulation geometry in xy-plane.

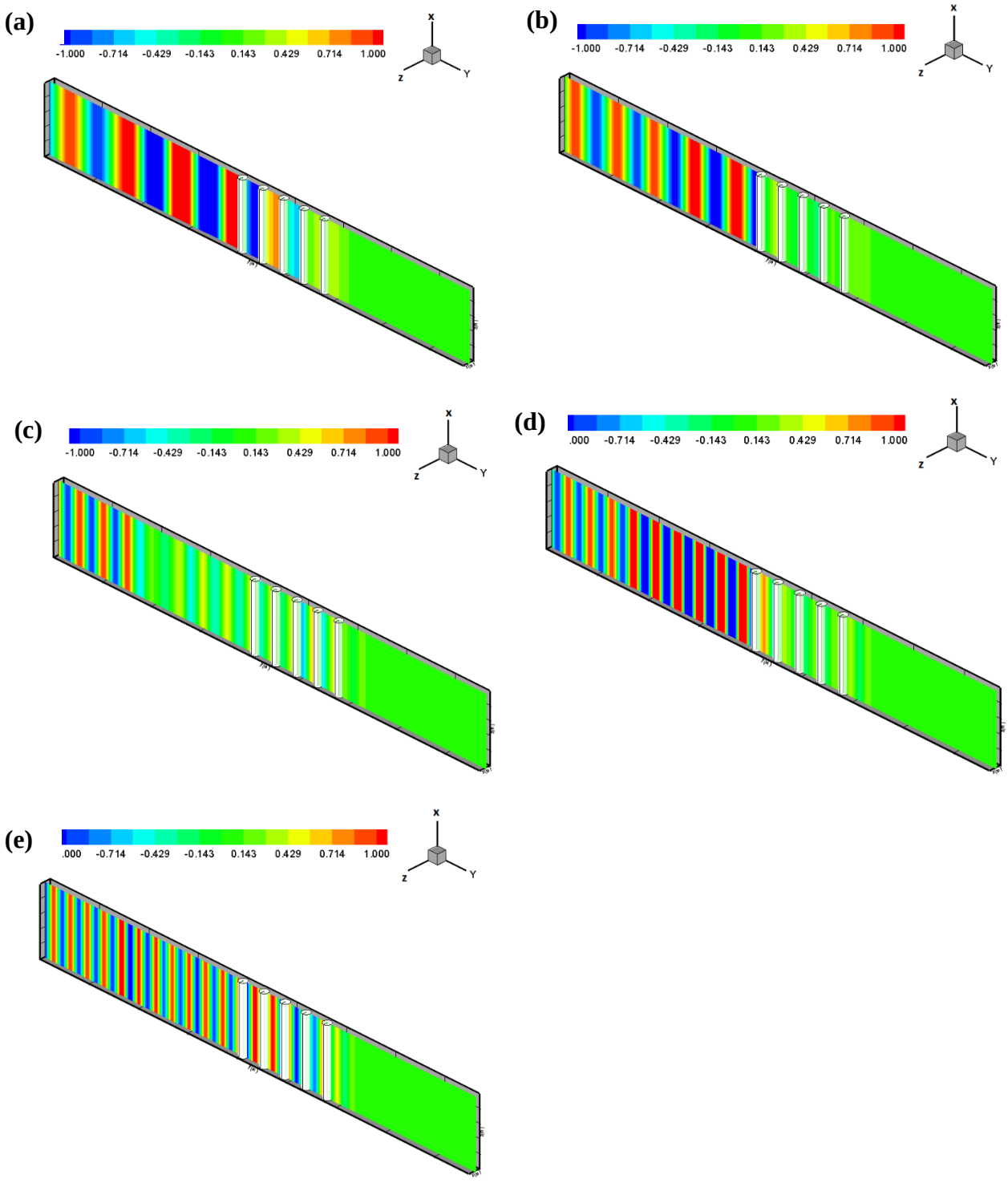

Fig. 2.19 Pressure contours at z-plane at the moment t=3.75ms of rigid sonic crystals (a) 1500Hz (b) 2000Hz (c) 3500Hz (d) 4000Hz (e) 5000Hz.

Figure. 2.19 (a)-(e) are the pressure contours at t=3.75ms of the 3D rigid sonic crystal simulations with different plane wave frequency from 1500Hz, 2000Hz, 3500Hz, 4000Hz and 5000Hz respectively. It can be seen that at this moment the sound wave is strengthened because the reflected waves, right before the first cylinder barrier when the sound frequency is 1500Hz, 2000Hz and 4000Hz. Contrarily when the sound frequency is 3500Hz the propagating sound wave is weakened by the reflected waves at t=3.75ms. From figure. 2.19 (c) we can see that the plane wave is weak before the first cylinder barrier. Different from the four simulations, when the sound wave has the highest frequency 5000Hz the incident wave propagation is not obviously strengthened or weakened by the reflections.

Figure. 2.20 (a)-(e) are the pressure contours at t=6ms of the 3D rigid sonic crystal simulations. From (a)-(e) we can find that when the sound source with frequency 1500Hz, 2000Hz and 3500Hz, the incident sound wave is strengthened right before the first cylinder barrier, and strongly weakened near the left boundary. On the contrary when the sound frequency is 4000Hz the incident wave is enhanced by the reflected waves all over the area before cylinder arrays. From figure. 2.20 (e) we can see that when the sound source has the highest frequency 5000Hz, the incident wave propagation is not obviously strengthened or weakened by the reflections and it can successfully pass through the cylinder arrays.

Based on figure. 2.19 and 2.20, we know that the sonic crystal is effective for sound blockage for the incident sound wave with frequency from 1500Hz to 4000Hz. But the sonic crystal is not effective for the highest sound frequency 5000Hz, since most of the incident wave could pass through the rigid cylinder barriers and reach the receiver.

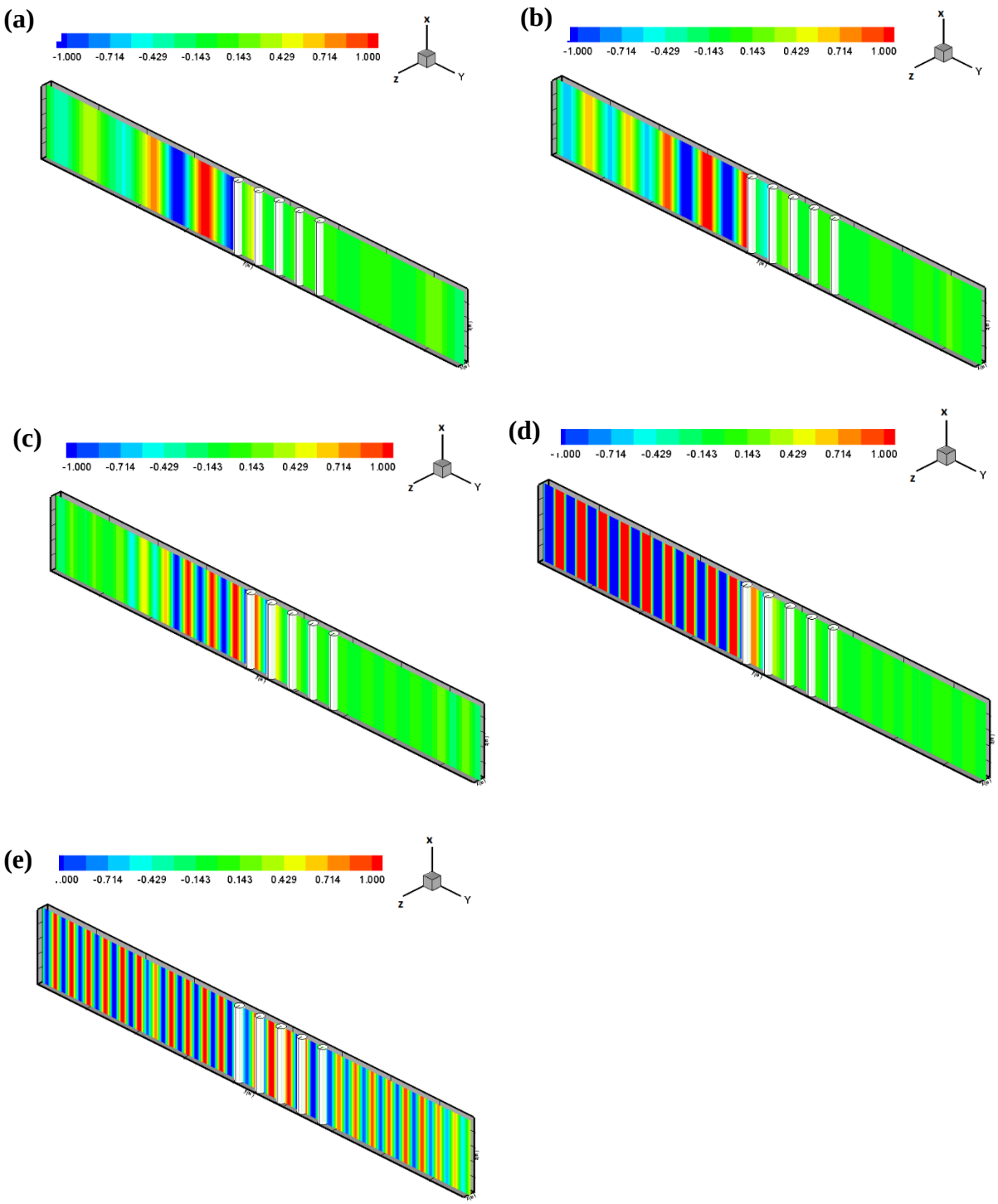

Fig. 2.20 Pressure contours at z-plane at the moment t=6ms of rigid sonic crystals (a) 1500Hz (b) 2000Hz (c) 3500Hz (d) 4000Hz (e) 5000Hz.

Figure. 2.21 (a)-(e) give the numerical sound attenuations of the simulations with different sound frequency. When the sound source has frequency from 1500Hz to 4000Hz, the numerical sound attenuations have two main band gap as same as the experimental data. And the magnitude of sound attenuation at the band gap is also close to the experiment results. When the incident wave frequency is 3500Hz or 4000Hz, the sound attenuations have more fluctuations at the high frequency domain and most of the values are below zero. Form figure. 2.21 (e) we can see that when the incident wave frequency is 5000Hz, the two band gaps shown in the other figures do not exist. And the sound attenuations are lower than zero along the frequency domain, which means the sonic crystal cannot work for sound blockage for this high source frequency. This result coincides with the conclusion that we have drawn based on the contours.

The comparison of the averaged sound attenuations between the simulation and the experimental data in Ref. [88] is given in Fig. 2.21 (f). From the comparison we can see that the simulated sound attenuations have two band gaps, around 1250Hz-2500Hz and 3500Hz-4500Hz, with the maximum sound attenuation of 30dB and 35dB respectively. The experimental results are close to the simulated results for both the two band gaps. The first maximum sound attenuation is achieved at frequency about 1950Hz. According to the Bragg's law in Ref. [88]:

$$f = \frac{c}{2a} = \frac{340}{2 \times 0.085} = 2060.6\text{Hz}$$

Therefore, the simulated band gap frequency has a very good agreement with the theoretical value.

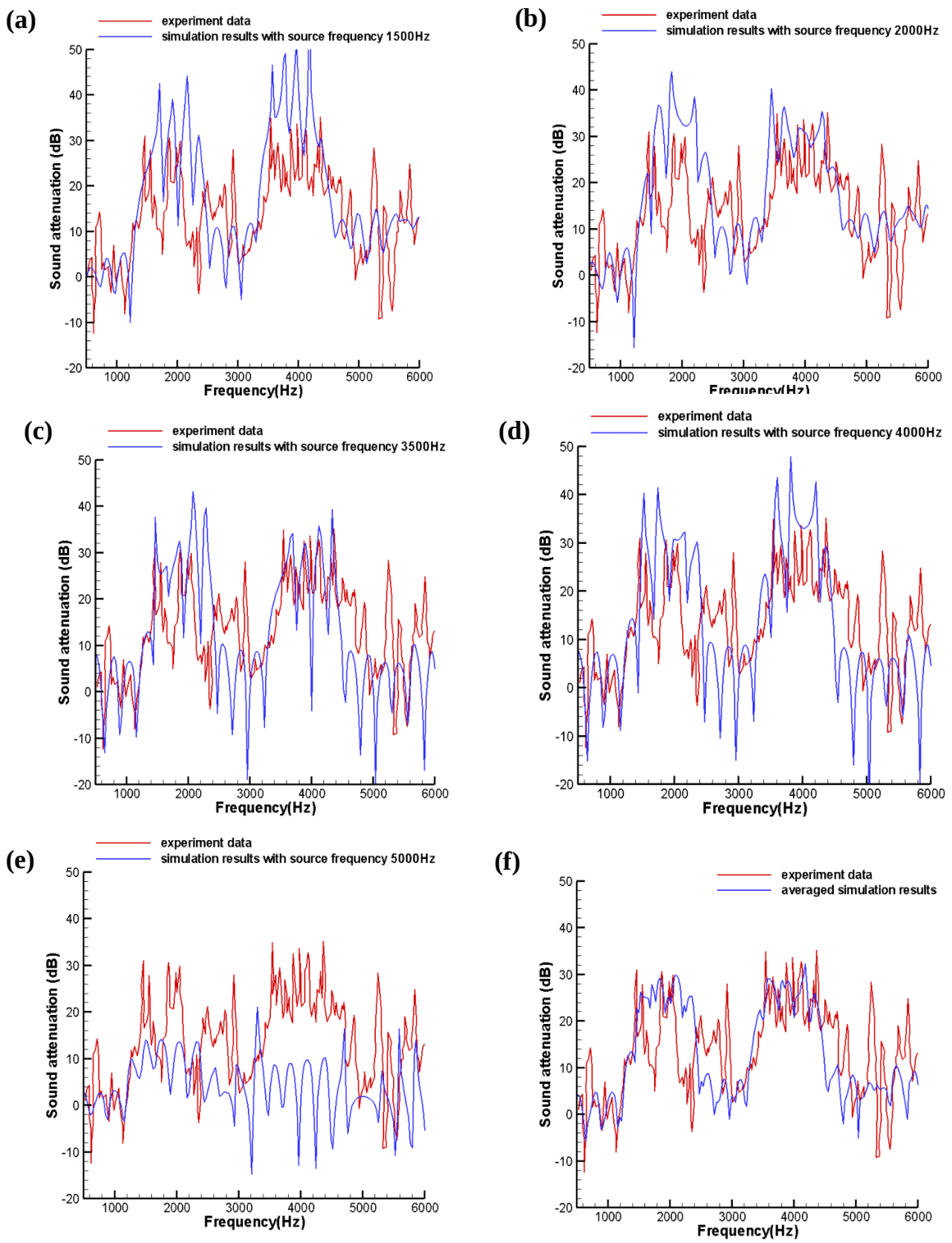

Fig. 2.21 Sound attenuations versus frequency for rigid sonic crystals with different sound frequency (a) 1500Hz (b) 2000Hz (c) 3500Hz (d) 4000Hz (e) 5000Hz (f) averaged results.

2.3.3 Effect of Porous Materials

In this section, the sound blockage effect of the sonic crystals made of porous media is studied. The geometry and all the initial conditions are remained the same as the rigid cylinder arrays simulations except that changing the material of cylinders to porous media. Two different resistivity 2kPa s m^{-2} and 50kPa s m^{-2} are tested for the porous sonic crystals, and the frequency of incident plane wave is selected as 1500Hz, 2000Hz and 3500Hz. The simulation results are also compared with the results of the corresponding rigid cylinder arrays cases.

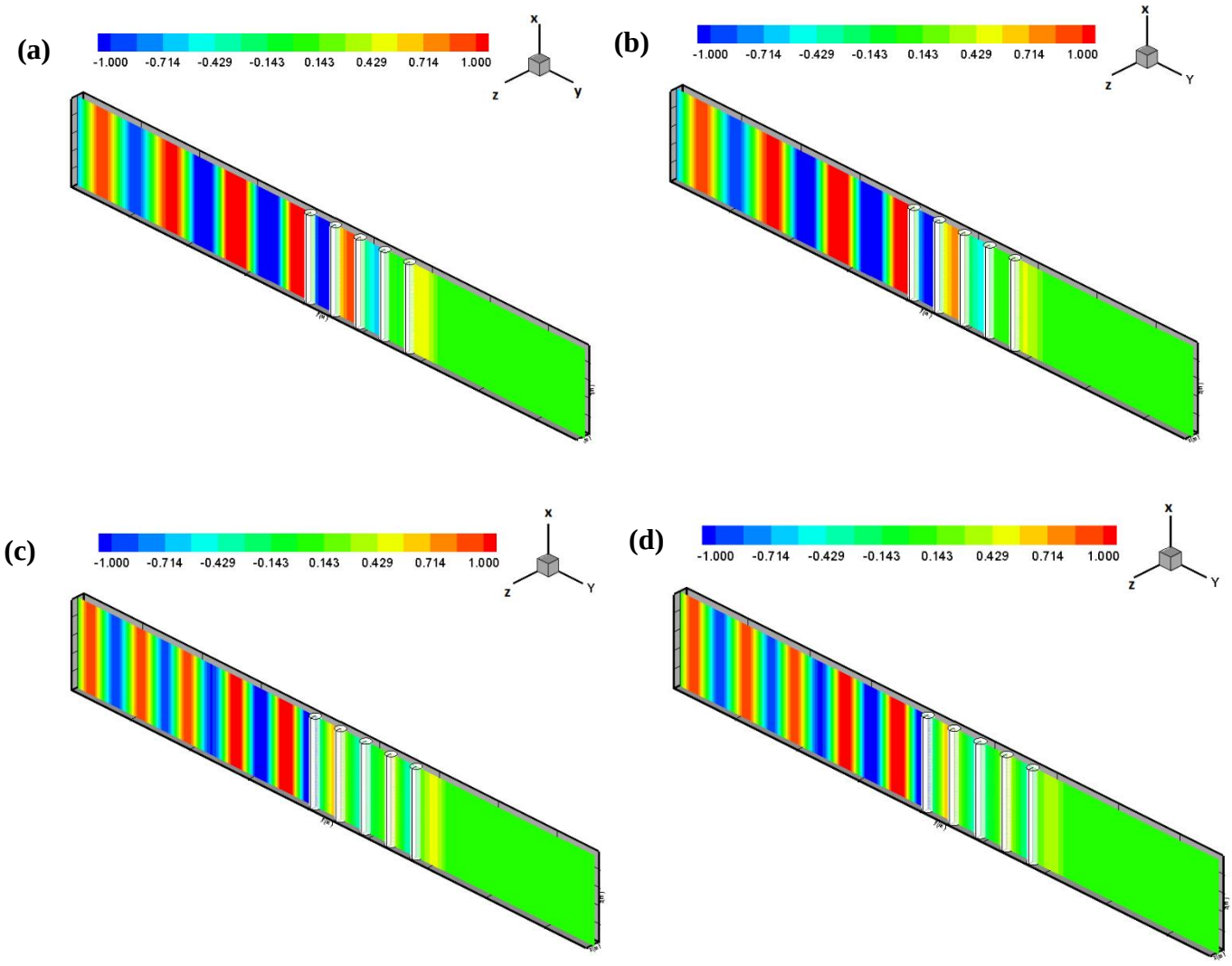

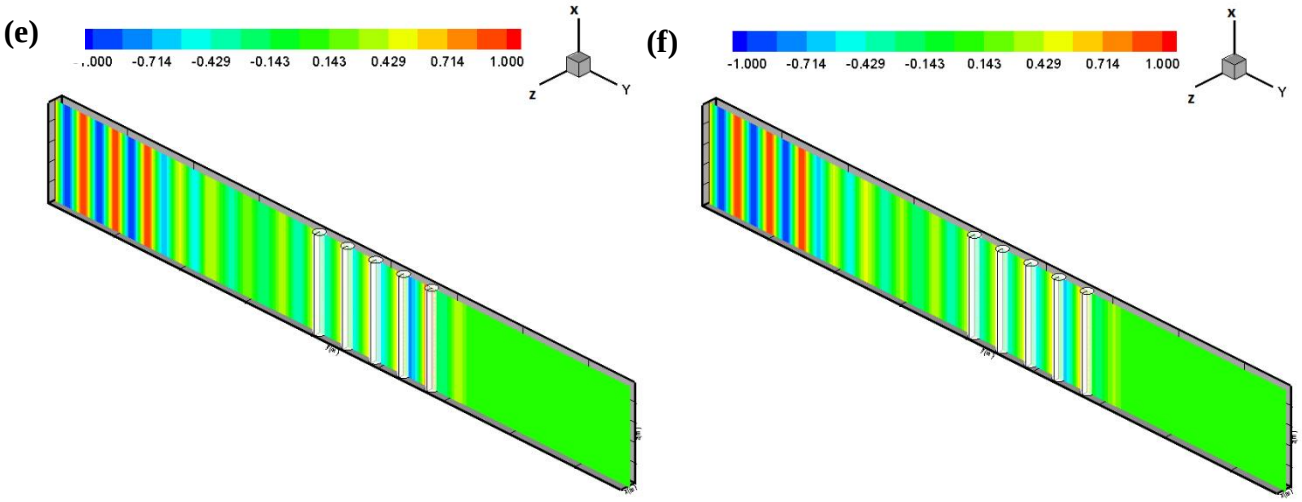

Fig. 2.22 Pressure contours at z-plane at the moment t=3.75ms of porous sonic crystals (a) 1500Hz, 2k (b) 1500Hz, 50k (c) 2000Hz, 2k (d) 2000Hz, 50k (e) 3500Hz, 2k (f) 3500Hz, 50k

Figure. 2.22 (a)-(f) are the pressure contours at t=3.75ms of the 3D porous cylinder arrays simulations with different plane wave frequency and cylinder resistivity. We can see that the pressure distributions are almost the same between the two different porous media resistivity at this moment except the area after the cylinder arrays. By comparison we can see that the pressure after the fifth cylinder is higher when the resistivity of the porous cylinders is $2\mathrm{kPa\ s\ m^{-2}}$. This phenomena can be easily explained that when the impedance of the cylinders is lower, the more of the incident wave is allowed to pass through the cylinder arrays.

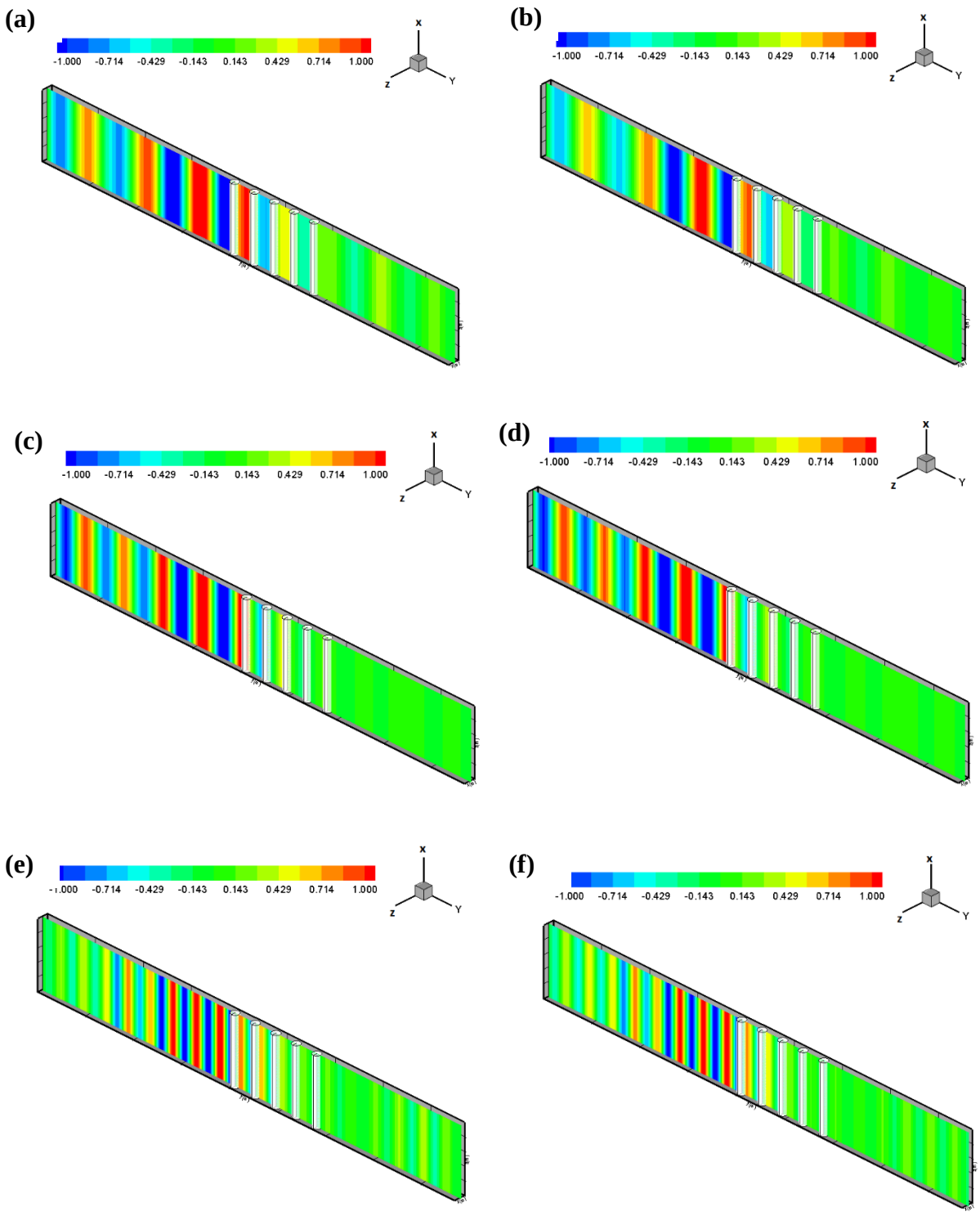

Fig. 2.23 Pressure contours at z-plane at the moment t=6ms of porous sonic crystals (a) 1500Hz, 2k (b) 1500Hz, 50k (c) 2000Hz, 2k (d) 2000Hz, 50k (e) 3500Hz, 2k (f) 3500Hz, 50k

Figure. 2.23 (a)-(f) are the pressure contours at t=6ms of the 3D porous cylinder arrays simulations. After long enough time propagation, the pressure distributions become different between the two different porous media resistivity. First, for the incident wave with frequency 1500Hz, the pressure right before the first cylinder is similar between the two different porous materials. The pressure near the left boundary is higher when the porous cylinders have lower impedance. For the incident wave with frequency 2000Hz, we can see that the phase of the propagating wave is different between two different porous materials. From figure. 2.23 (e) and (f) it can be found that when the incident wave has frequency 3500Hz, the pressure distribution is totally different between two porous materials. The wave near the left boundary is weak and is enhanced before the cylinder arrays when the porous resistivity is 2kPa s m^{-2}. On the contrary the wave is not influenced near the entrance and is diminished before the cylinder arrays when the porous resistivity is 50kPa s m^{-2}. Another noteworthy phenomenon is that when the sound wave has frequency 3500Hz the wave can reach almost the right boundary with the low flow resistivity 2kPa s m^{-2} of the cylinder arrays, but the wave is almost stopped by the cylinder arrays with flow resistivity 50kPa s m^{-2}.

The numerical sound attenuations of porous sonic crystals, and the comparison with rigid sonic crystal results are shown in figure. 2.24. Based on the averaged values and the comparison, it can be seen that the sound attenuation curves of the three different sonic crystal materials have the same number of fluctuations, but very different magnitude. The numerical sound attenuations at low and medium frequency domain are similar between the three simulations, and the values simulated with rigid sonic crystal at the two band gaps are much higher than the results of porous sonic crystal, while the porous sonic crystal with resistivity 50kPa has slightly higher attenuation than the one with resistivity 2kPa. At high frequency domain (greater than 4500Hz), the porous

sonic crystals have high sound attenuations than the rigid sonic crystal. As a result the porous sonic crystals have better sound blockage effect than the rigid sonic crystals for high frequency sound source.

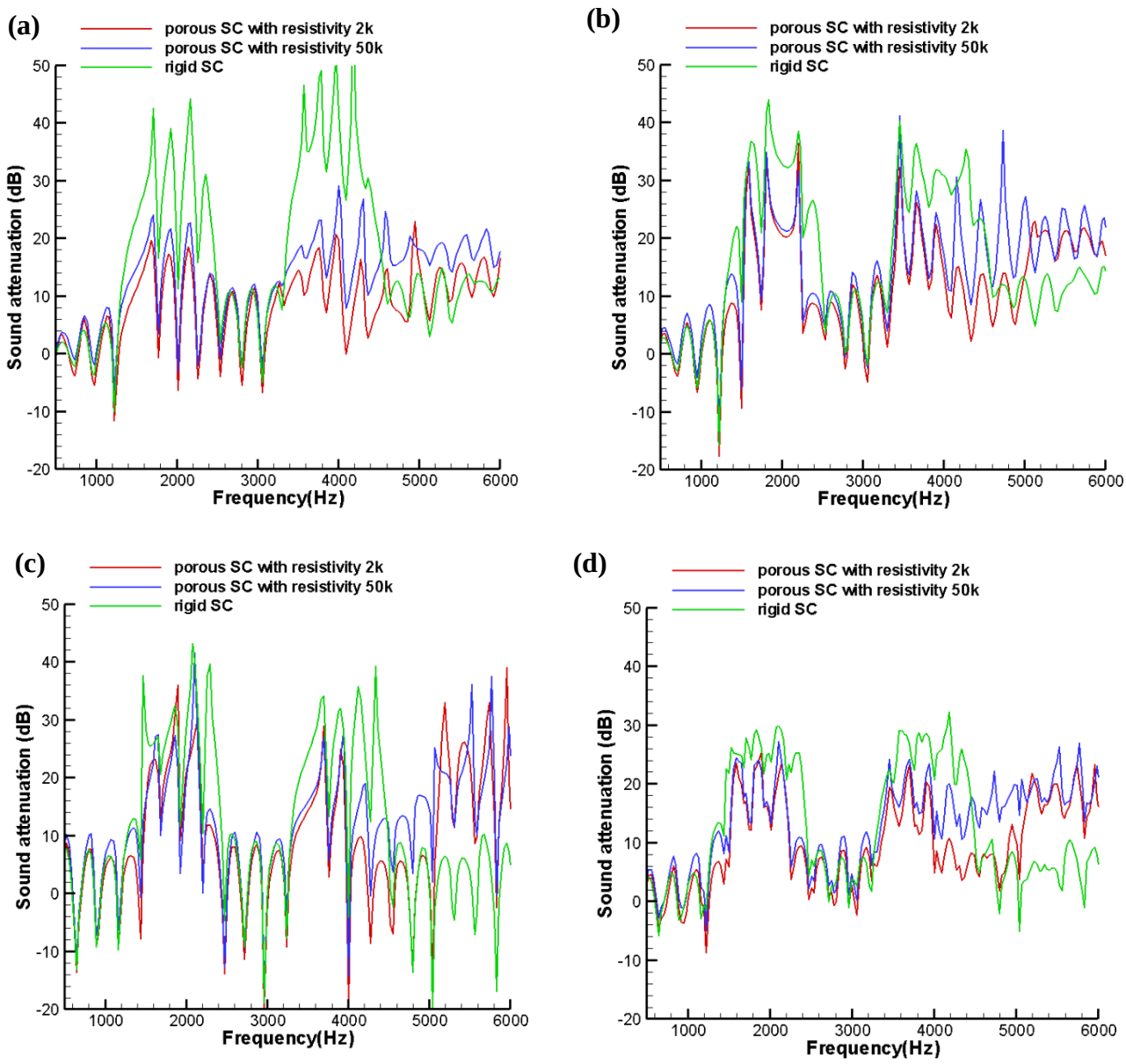

Fig. 2.24 Sound attenuations versus frequency for porous sonic crystals with different sound frequency (a) 1500Hz (b) 2000Hz (c) 3500Hz (d) averaged results

2.4 Summary

In this chapter, the sound blockage effect of cylinder arrays is studied for both two- and three-dimensional cases. Based on the discussions in this chapter we see how the array and the material of sonic crystals can influence the sound blockage effect.

It has been proved that the finite-difference time-domain method incorporated with the immersed boundary method provides a valid model for the sound propagation through sonic crystals. For the two-dimensional simulations of the sound propagates through sonic crystals perpendicularly in free filed, a very good agreement between our numerical band gap frequency and the theoretical result is found. When the number of cylinders in z-direction is fixed, the more cylinders in the wave propagation direction results in better sound blockage effect when the receiver is far. This conclusion is not necessarily valid when the receiver is close to the sonic crystal because the sound pressure level is enhanced due to the reflections.

The Euler-type moving zonal-domain approach in Ref. [97] is applied for three-dimensional simulations. The influence of moving domain size is discussed based on the comparison with the numerical results from non-moving domain. The simulation results from moving-domain agree well with the non-moving domain simulation, while the computational efficiency is greatly improved. The simulation results are also compared and agree well with the experimental data in Ref. [88]. Based on the comparison between rigid and porous sonic crystals, it is found that selecting appropriate materials is important aim at different sound source frequency. The sonic crystals made of porous material with intermediate flow impedance is effective for noise blockage.

3 Sound Propagation over Vortex Pair

In this chapter, the scattering effects of high subsonic vortex dipole on two-dimensional sound wave propagation is studied. When acoustic wave propagates through a vortex or vortex dipole, the sound field may be significantly modified by the interactions between the incident wave and the vortical flow in Ref. [99]. Both the amplitude and phase of the sound wave will be affected during the propagation through vortical flow. Knowledge of sound scattering by a vortical flow field is very important for many aeroacoustics studies. Previous studies on this topic include analytical studies in Ref. [100]-[115] and numerical simulations in Ref. [71], [72], [116] and [37]. One classical numerical calculations carried out by Colonius in Ref. [71], Navier-Stokes equations are applied to directly solve the wave propagation through a single vortex, and very good calculation results are achieved. However there are also several drawbacks appeared about this numerical model. Compared with the direct linearized Euler equations, this model requires a very high grid resolution and high order scheme to achieve accurate results. Cheinet et al. in Ref. [72] applied the linearized Euler equations to solve the problem of sound propagation over a single vortex. The second-order central finite difference method was used for the spatial derivatives, and a fourth-order Runge-Kutta was used for time integration. Their simulation was only limited to the propagation of acoustic waves of weak amplitude in low Mach number flows. The accuracy of their method for high Mach number vortical flow problem was not validated yet.

When we conduct simulations for high Mach number vortical flow, the ordinary numerical schemes are not accurate enough in dealing the convective terms because the velocity and its gradient are high. As a result great numerical errors are generated in the domain near the high speed vortical flow. A high order WENO scheme in Ref. [101]-[110] is adopted to the regions with high velocity to solve convection-dominant background flow in time domain numerical

simulation. The WENO scheme can not only achieve higher-order accuracy near the high gradient velocity regions, but also maintain a stable and non-oscillatory solution.

3.1 High Order Numerical Scheme

In the simulations for this topic, a fifth order WENO scheme in Ref. [109]-[110] is applied for the convention terms. To illustrate the implementation of the high-order upwind scheme for the convection terms in the current simulation, we take one-dimensional convection term as an example.

The expression of convection terms is written as:

$$a\frac{\partial u}{\partial x} = a^{+}u_x^{-} + a^{-}u_x^{+} \tag{3.1}$$

Where $a^{+} = \max(a, 0)$ and $a^{-} = \min(a, 0)$.

The fifth order WENO scheme for u_x^{-} and u_x^{+} is given like below:

$$u_x^{\pm} = w_1^{\pm}u_x^{1\pm} + w_2^{\pm}u_x^{2\pm} + w_3^{\pm}u_x^{3\pm} \tag{3.2}$$

Where $w_1^{\pm}$, $w_2^{\pm}$ and $w_3^{\pm}$ are the weight coefficients, and can be found in Ref. [109]. In addition, $u_x^{1\pm}$, $u_x^{2\pm}$ and $u_x^{3\pm}$ are three ENO3 stencils defined as:

$$u_x^{1\pm} = \frac{1}{3}q_1^{\pm} - \frac{7}{6}q_2^{\pm} + \frac{11}{6}q_3^{\pm} \tag{3.3}$$

$$u_x^{2\pm} = -\frac{1}{6}q_2^{\pm} + \frac{5}{6}q_3^{\pm} + \frac{1}{3}q_4^{\pm} \tag{3.4}$$

$$u_x^{3\pm} = \frac{1}{3}q_3^{\pm} + \frac{5}{6}q_4^{\pm} - \frac{1}{6}q_5^{\pm} \tag{3.5}$$

where

$$q_n^{-} = \frac{u_{i+n-3,j} - u_{i+n-4,j}}{\Delta x}, \quad n = 1, 2, ..., 5 \tag{3.6}$$

and

$$q_n^+ = \frac{u_{i-n+4,j} - u_{i-n+3,j}}{\Delta x}, \quad n = 1, 2, ..., 5 \tag{3.7}$$

In this chapter, the fifth-order WENO scheme is applied only for the regions around the vortex, and the numerical scheme in Ref. [96] is used for solving convection in the remaining regions. It should be noted that the background velocity filed generated by the vortices is assumed to be steady.

3.2 Numerical Model Description

First the sound propagation over single vortex is discussed. The description for single vortex is shown in Fig. 3.1, where θ is the angle between receiver and the center of vortex, and Γ is the circulation of vortex. The graphic illustration for the single vortex is shown in Fig. 3.1.

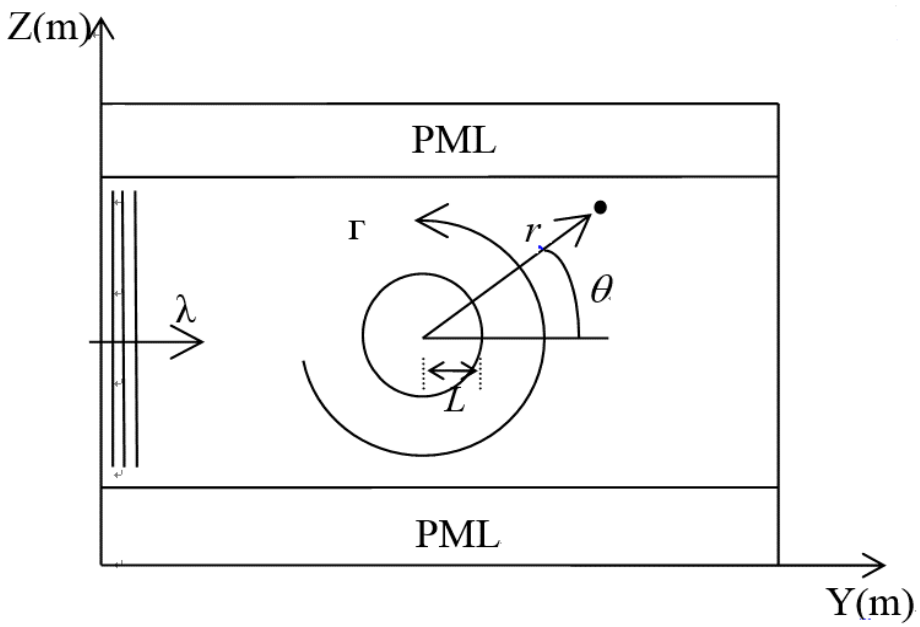

Fig. 3.1 Description of the geometry and coordinate system for the plane wave propagation over single vortex.

For a periodic plane wave given as:

$$p = \sin\left(2\pi f\right) \tag{3.8}$$

where f is wave frequency. Since we focus on low frequency plane wave, the wave frequency is set as $f = 85\text{Hz}$. For a homentropic vortex, the tangential velocity is given in Ref. [71]:

$$v_\theta = \frac{\Gamma}{2\pi R}\left[1-\exp\left(-\alpha\left(\frac{R}{L}\right)^2\right)\right] \tag{3.9}$$

where L is the length of vortex core, R is the distance from the center of vortex or vortex pair to the receiver, and α is a constant selected as 1.2564. The two length scales are related by the Mach number of the vortex, defined as the maximum vortex velocity relative to the sound speed:

$$M = \beta\frac{\Gamma}{2\pi L a_\infty} \tag{3.10}$$

where β is a numerical constant which depends on the specific distribution of tangential velocity in the core of vortex, and a_∞ is the speed of sound at infinity. Different Mach numbers and the corresponding values of Γ are listed in Table 3.1.

Table 3-1 Different Mach number and corresponding vortex circulation

M	$\Gamma(m^2/s)$
0.0625	190.4
0.125	367.2
0.25	748
0.5	1496

After simulation, the simulated pressure is normalized by calculating the root-mean-square pressure p_{rms} in Eq. (3.11):

$$p_{rms} = \sqrt{\frac{\int (p_1 - p_2)^2 \, dt}{T}} \tag{3.11}$$

where p_1 is the simulated pressure with vortex or vortex pair, and p_2 is the simulated pressure without vortical flow. According to the low frequency theories in Ref. [71], the root-mean-square pressure level p_{rms} in the far filed should scale as:

$$p_{rms} \sim p_I \varepsilon (\lambda / r)^{1/2} \tag{3.12}$$

where p_I is the amplitude of the incident wave, and the parameter ε is related to the vortex strength and the wave number of sound wave.

$$\varepsilon = \Gamma / (a_\infty \lambda) \tag{3.13}$$

Based on the discussions for sound propagation over single vortex in Ref. [98], the root-mean-square pressure level scaled by the right hand side of Eq. (3.12) is shown in Fig. 3.2.

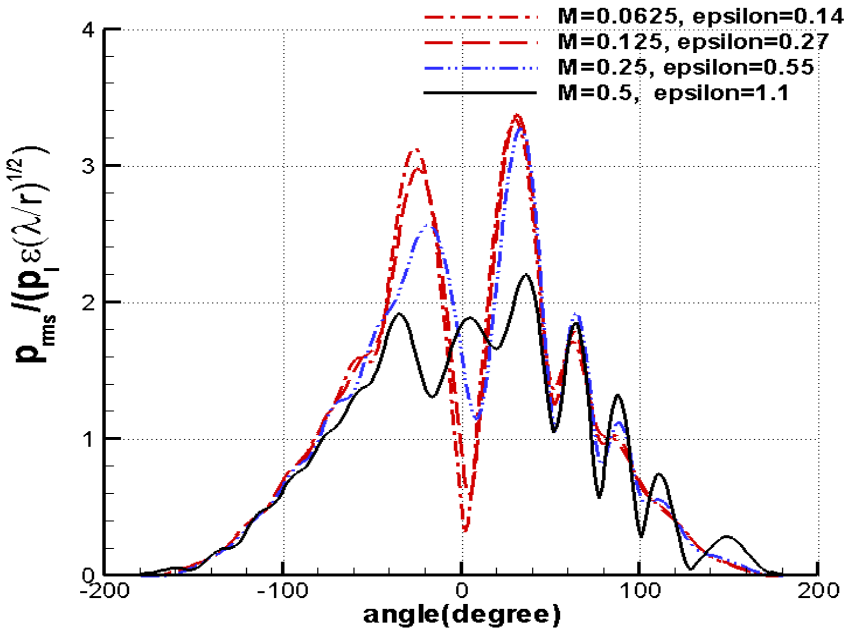

Fig. 3.2 Scaled root-mean-square pressure level for single vortex.

In the simulations in Ref. [98], the ratio λ / r is fixed as a constant 2.5, from Fig. 3.2 we can find that when ε is decreased, which means the Mach number becomes small, the curves scaling with ε appear to hold.

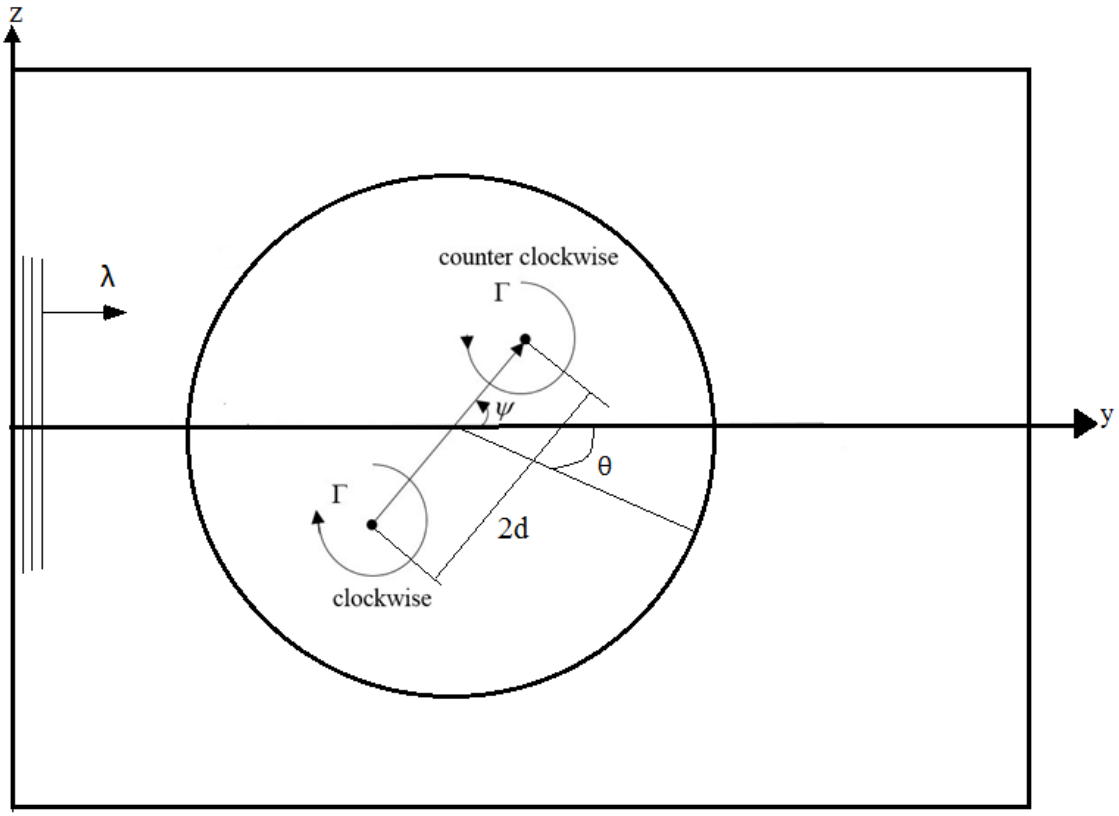

Fig. 3.3 Description of the geometry and coordinate system for the plane wave propagation over vortex pair.

For the simulations for vortex pair in this chapter, the geometry and coordinate system are shown in Fig. 3.3, where ψ is the vortex pair orientation angle. It is defined as the contour-clockwise angle between y-axis and the vector from the center of clockwise vortex to the center of counter-clockwise vortex. In our simulations, different orientations of vortex pair ψ from $0°$ to

$315°$ are tested. The *2d* is the distance between two centers of vortex pair, and it is selected as 2m, so that the core of each vortex is not overlapping with to each other.

The size of computational domain in y-direction is $y \in [0,110]m$ and $z \in [0,160]m$ in z-direction. Uniform mesh is used for simulations and grid size $\Delta y = \Delta z = 0.05m$. Two perfectly-matched-layers with thickness 20m are specified at the top and bottom boundaries. The center of the receiver circle is located at (20m, 80m), and three different values of the radius *r* are tested: 8m, 10m and 12m. Time step $\Delta t = 2 \times 10^{-6} s$ and total simulation time 0.31s. The parameters L and a_∞ given in Eq. (3.9) and (3.10) are 1m and 340m/s respectively. For each different angle ψ, the corresponding coordinates of the centers of vortex pair are given in table 3.2.

Table 3-2 Coordinates of vortex pair for different simulations

ψ (degree)	Vortex1 (clockwise)	Vortex2 (counter clockwise)
0	(19, 80)	(21,80)
45	(19.293, 79.293)	(20.707, 80.707)
90	(20, 79)	(20, 81)
135	(20.707, 79.293)	(19.293, 80.707)
180	(21, 80)	(19, 80)
225	(20.707, 80.707)	(19.293, 79.293)
270	(20, 81)	(20, 79)
315	(19.293, 80.707)	(20.707, 79.293)

3.3 Simulation Results and Discussions

The pressure distributions of each simulation, and the normalized pressure level versus different receiver locations are given in this section. Figure. 3.4, 3.6, 3.8 and 3.10 are pressure

contours for each different ψ with vortex pair Mach number 0.0625, 0.125, 0.25 and 0.5 respectively.

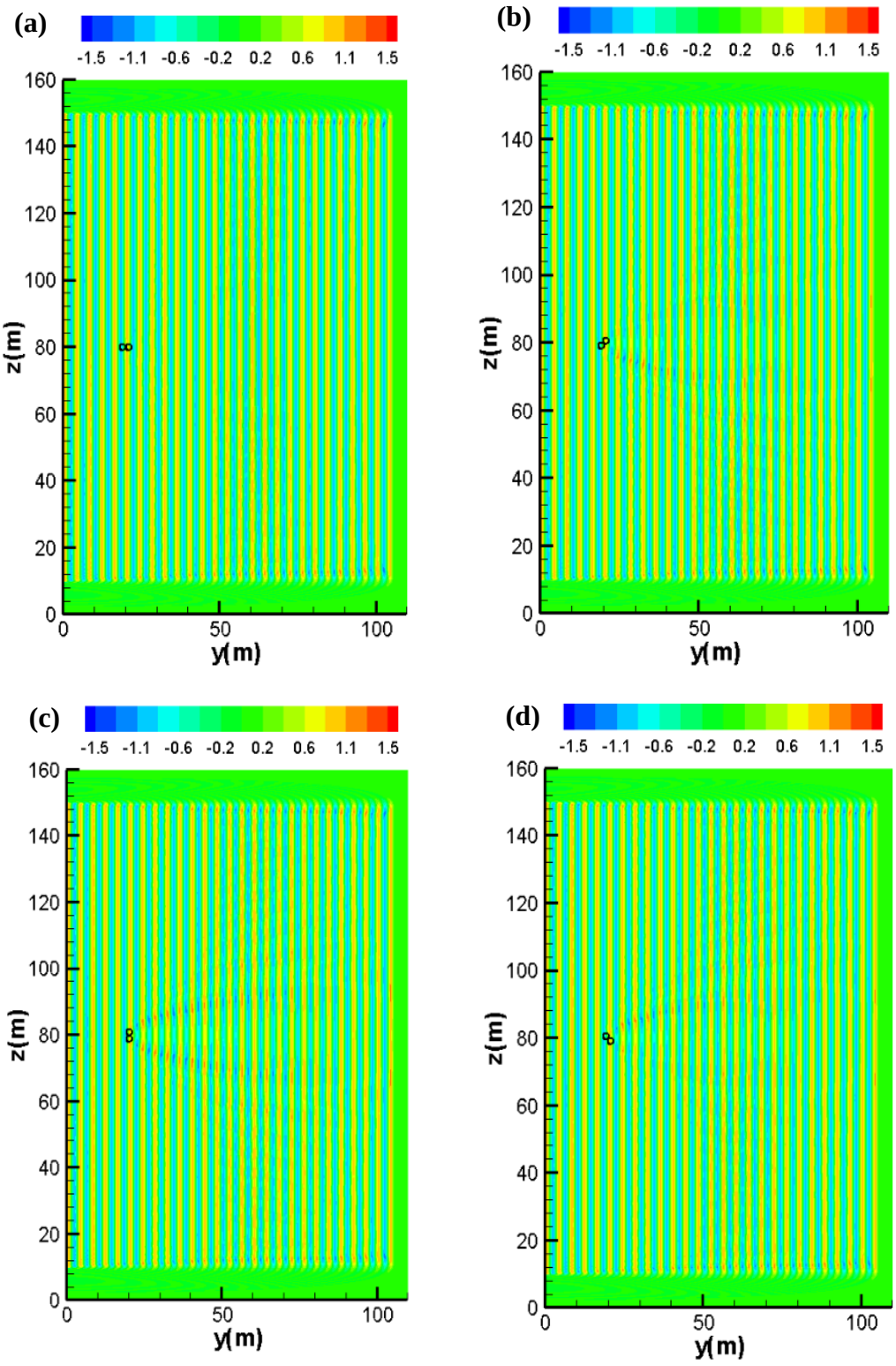

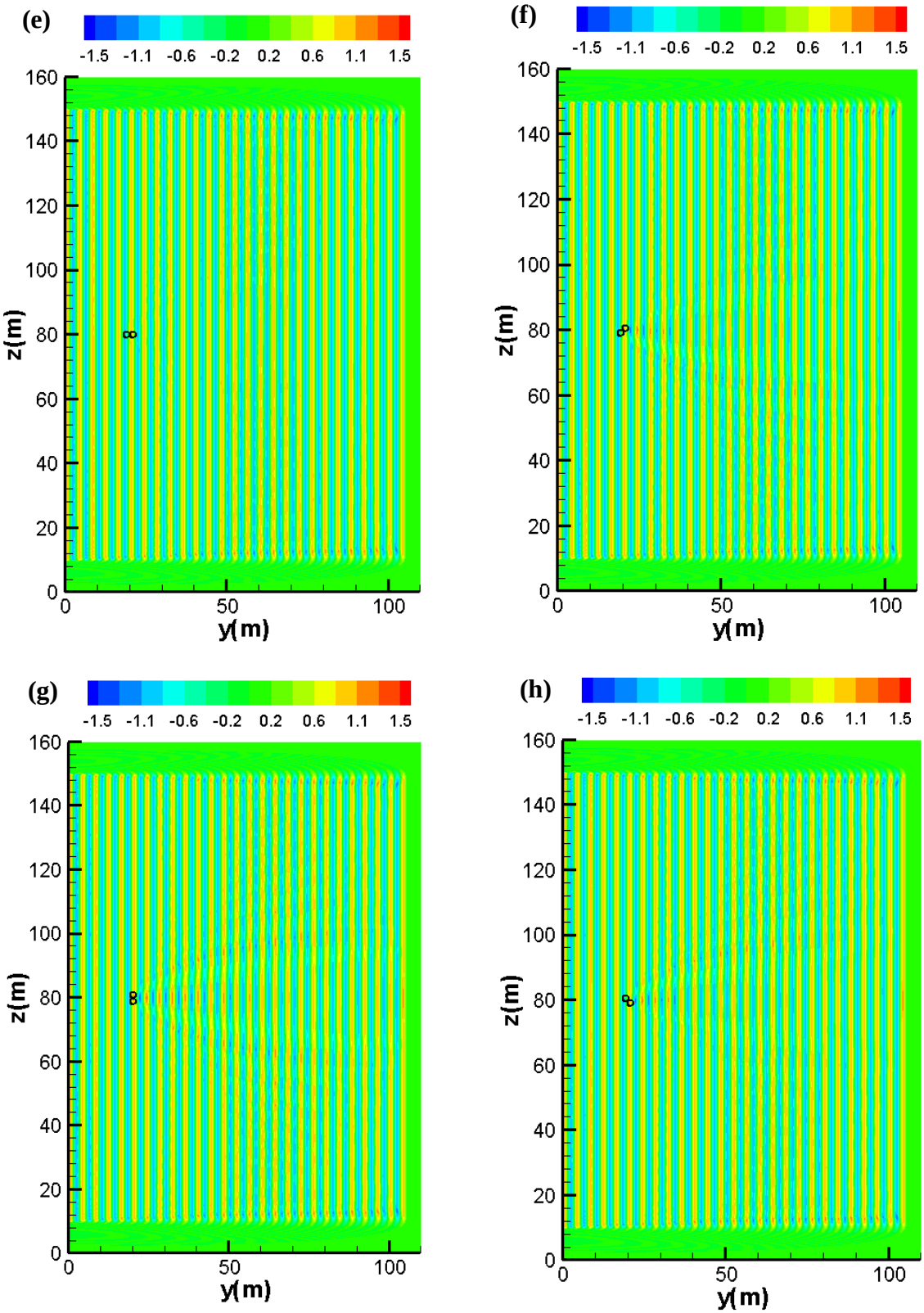

Fig. 3.4 Pressure contours at the moment t=0.31s with Mach number 0.0625 for different angle ψ (a) 0.0 (b) 45 (c) 90 (d) 135 (e) 180 (f) 225 (g) 270 (h) 315.

It can be seen in Fig. 3.4 that when the vortex pair is a low Mach flow with M=0.0625, the sound scattering effect is not relatively strong. When $\psi = 0°$ or $\psi = 180°$ the sound scattering effect is the weakest, while the sound scattering effect reaches the strongest when $\psi = 270°$. The same conclusions can also be drawn from the Fig. 3.4 which shows the normalized pressure level along the receiver circle for different ψ. We can find that when $\psi = 45°,\ 90°,\ 135°,\ 225°,\ 270°,\ 315°$ the normalized pressure level reaches the peak at $\theta = 0°$. Different from this phenomenon, when the sound scattering effect is the weakest, which means $\psi = 0°$ and $\psi = 180°$, the normalized pressure level peak locates at $\theta = -45°$ and $\theta = 45°$ respectively.

Furthermore the normalized pressure level distribution becomes symmetric about $\theta = 0°$ when $\psi = 90°$ and $\psi = 270°$. Also the three pairs of normalized pressure level curves: $\psi = 0°$ and $\psi = 180°$, $\psi = 45°$ and $\psi = 135°$, $\psi = 225°$ and $\psi = 315°$ are symmetric.

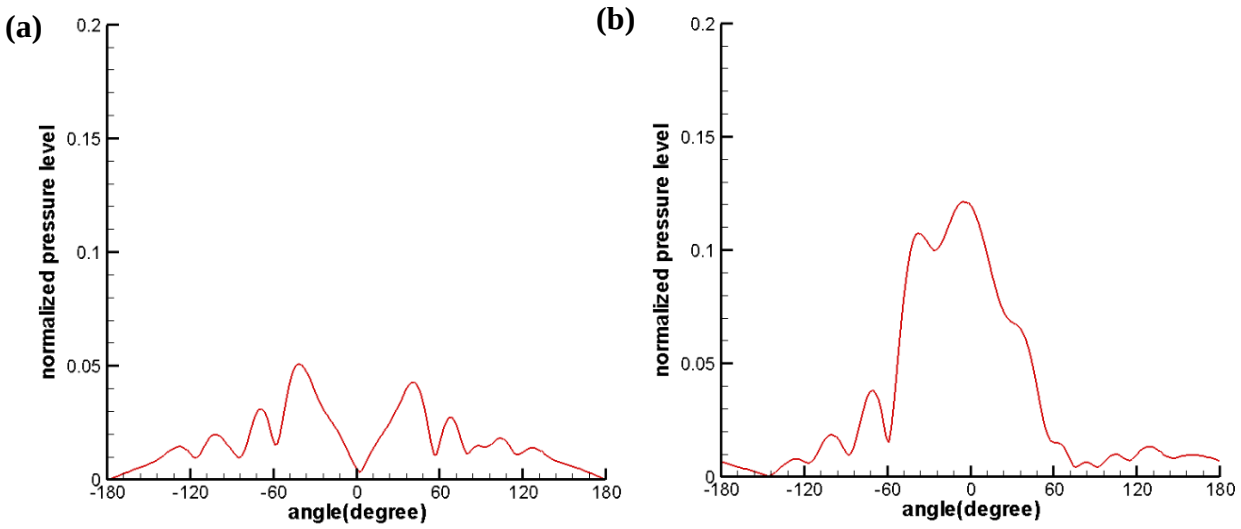

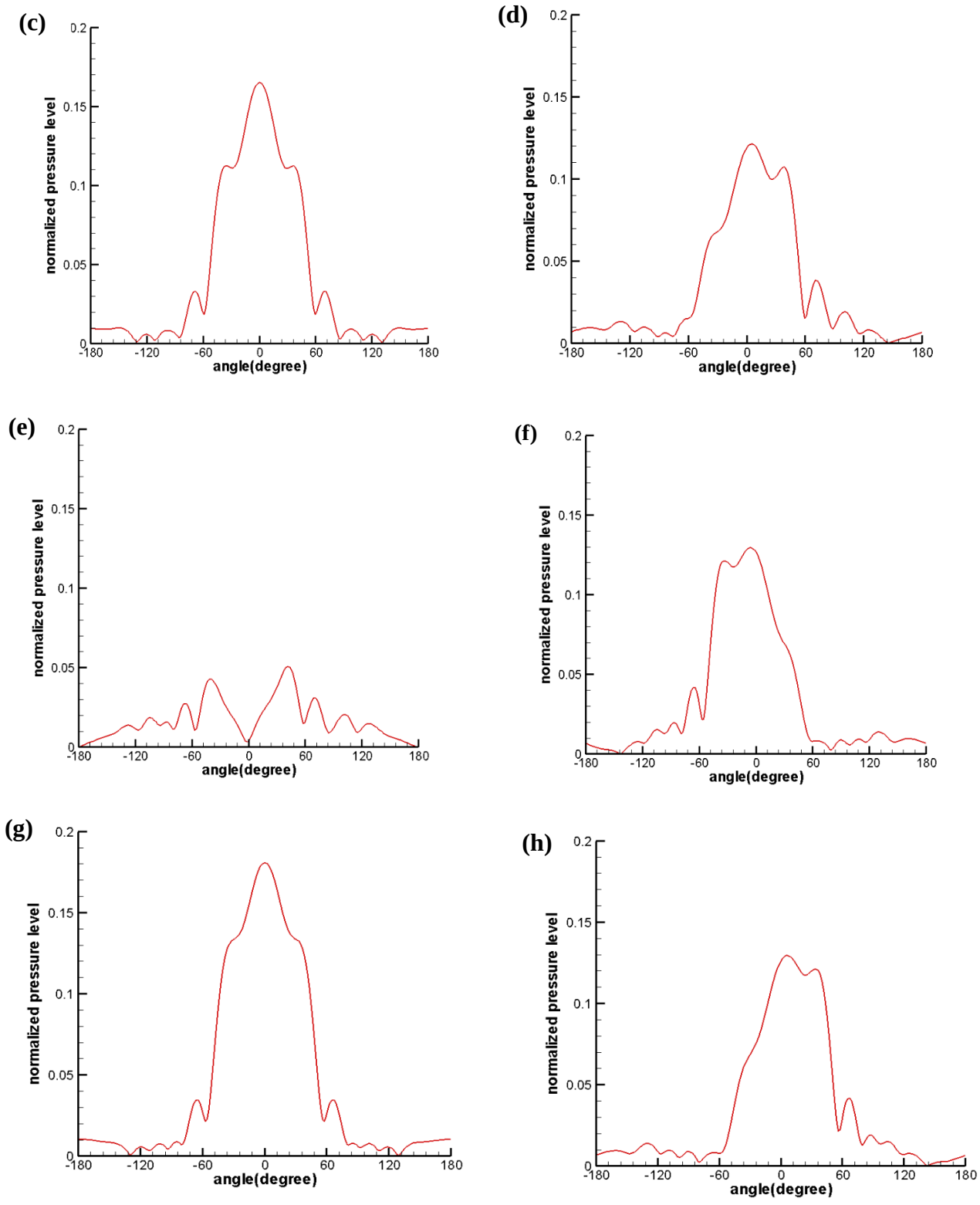

Fig. 3.5 Normalized pressure level with Mach number 0.0625 for different angle ψ (a) 0 (b) 45 (c) 90 (d) 135 (e) 180 (f) 225 (g) 270 (h) 315.

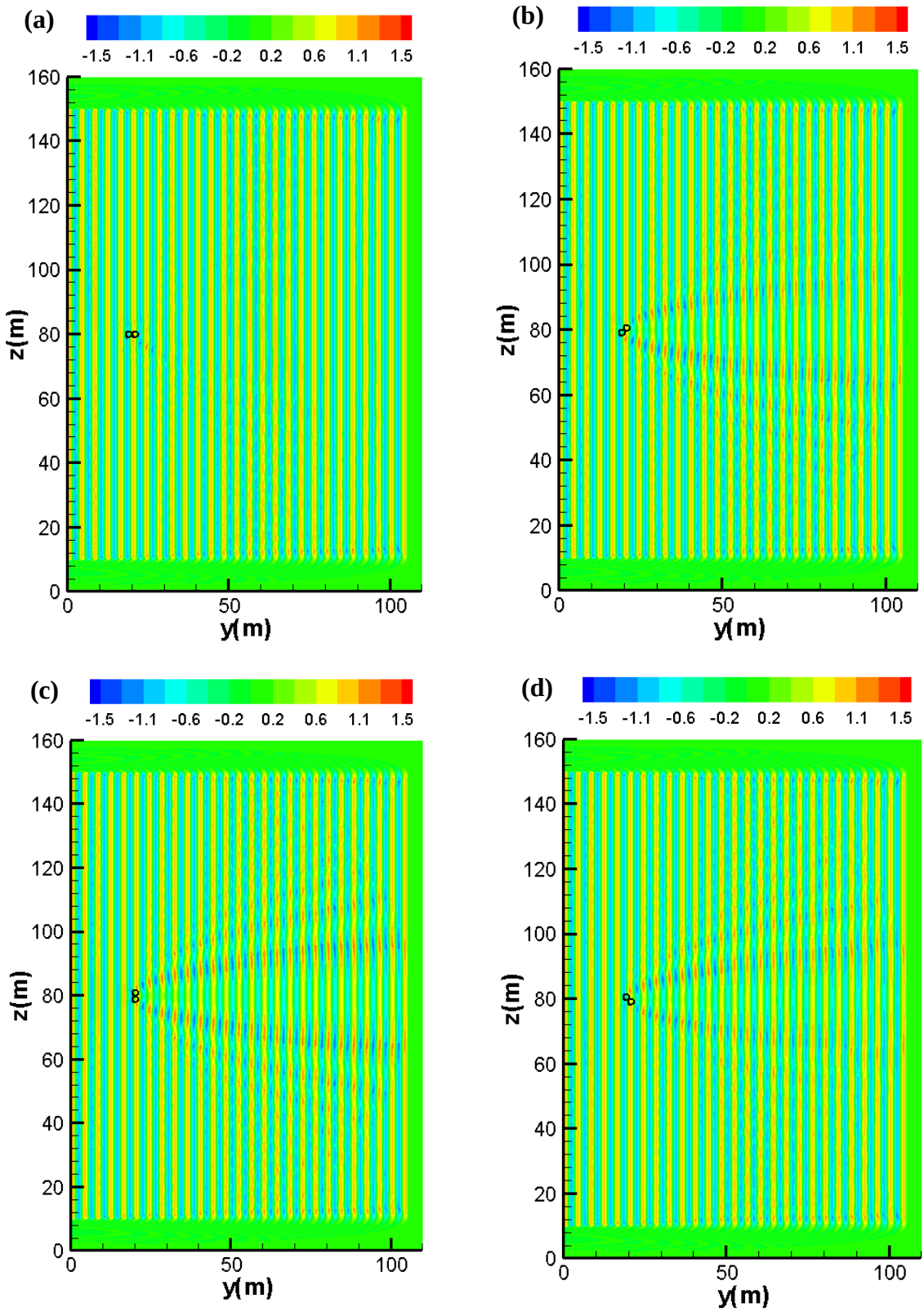
(a)
-1.5 -1.1 -0.6 -0.2 0.2 0.6 1.1 1.5
z(m)
y(m)
0 20 40 60 80 100 120 140 160
0 50 100
(b)
-1.5 -1.1 -0.6 -0.2 0.2 0.6 1.1 1.5
z(m)
y(m)
0 20 40 60 80 100 120 140 160
0 50 100
(c)
-1.5 -1.1 -0.6 -0.2 0.2 0.6 1.1 1.5
z(m)
y(m)
0 20 40 60 80 100 120 140 160
0 50 100
(d)
-1.5 -1.1 -0.6 -0.2 0.2 0.6 1.1 1.5
z(m)
y(m)
0 20 40 60 80 100 120 140 160
0 50 100

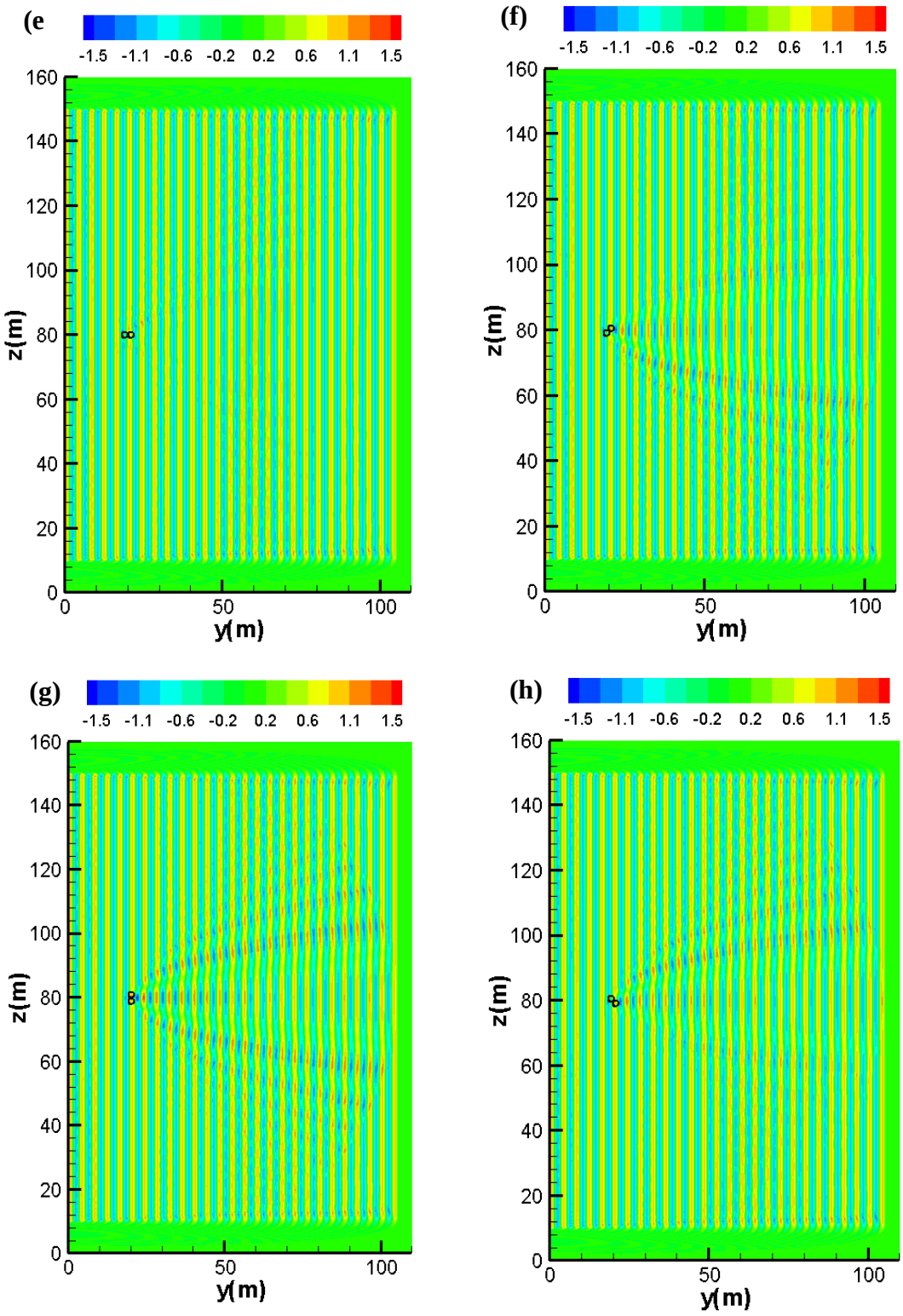

Fig. 3.6 Pressure contours at the moment t=0.31s with Mach number 0.125 for different angle ψ (a) 0.0 (b) 45 (c) 90 (d) 135 (e) 180 (f) 225 (g) 270 (h) 315.

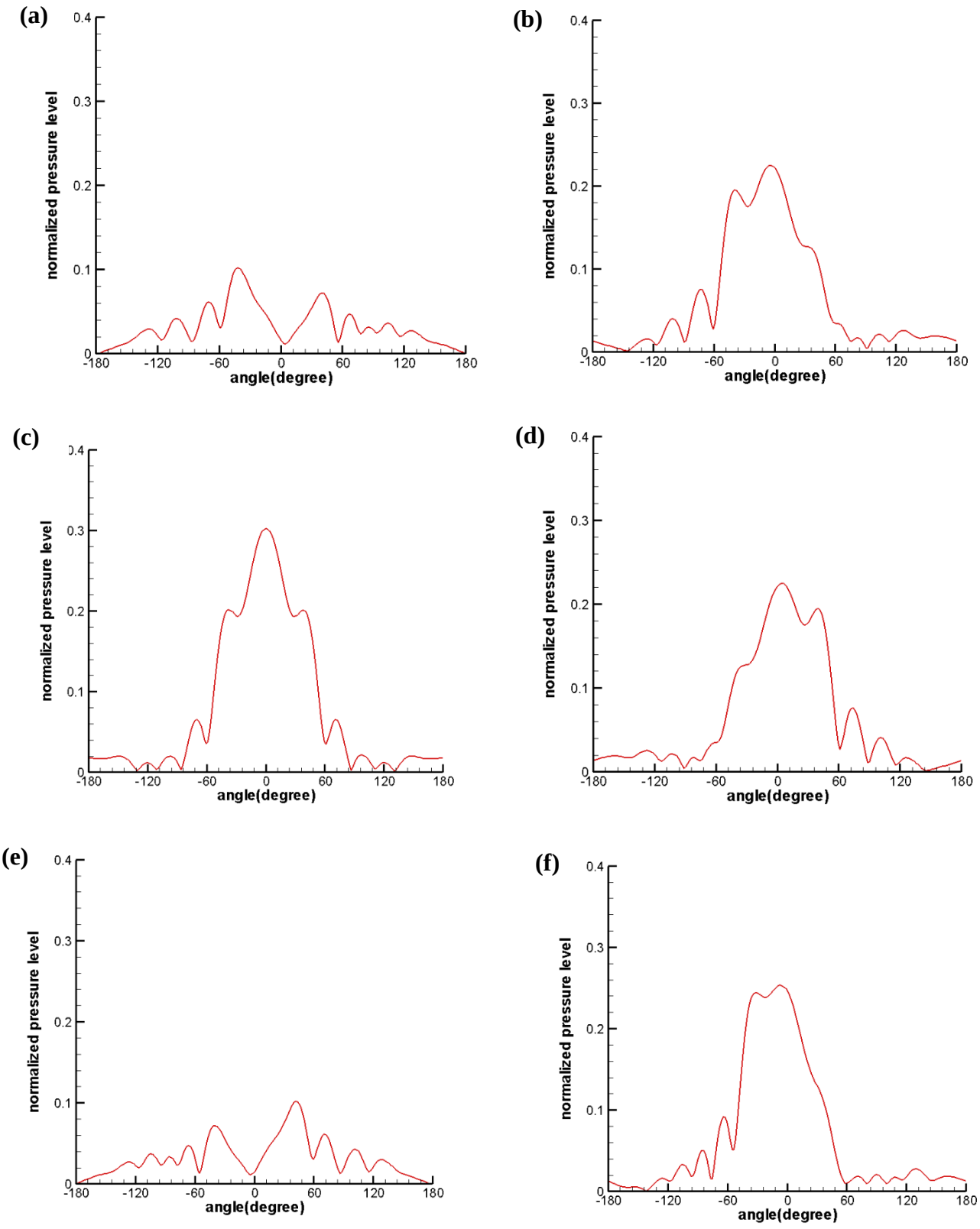
(a)
(b)
(c)
(d)
(e)
(f)
normalized pressure level
angle(degree)
0.4
0.3
0.2
0.1
0
-180
-120
-60
0
60
120
180

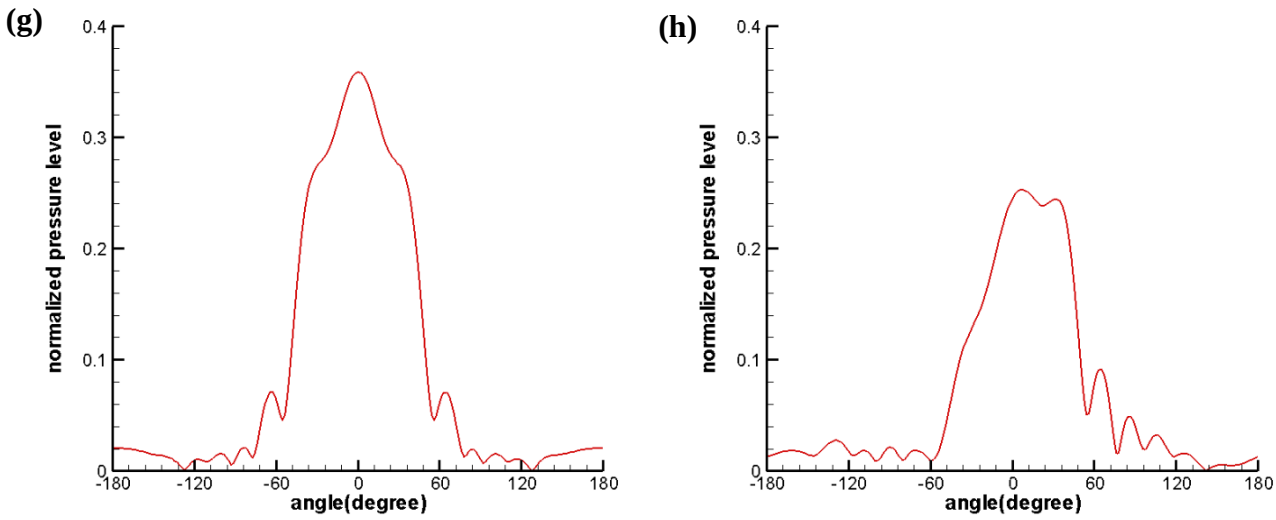

Fig. 3.7 Normalized pressure level with Mach number 0.125 for different angle ψ (a) 0 (b) 45 (c) 90 (d) 135 (e) 180 (f) 225 (g) 270 (h) 315.

Fig. 3.6-3.9 give the pressure contours and normalized pressure level curves for different angles ψ and Mach number 0.125 and 0.25, and the same conclusions discussed for Mach 0.0625 in the previous text can be found. Based on the pressure contours we can see that the sound scattering effects become stronger as the Mach number increases, and for each Mach number the sound scattering effect becomes the strongest when $\psi = 270°$ and the weakest when $\psi = 0°$ and $\psi = 180°$.

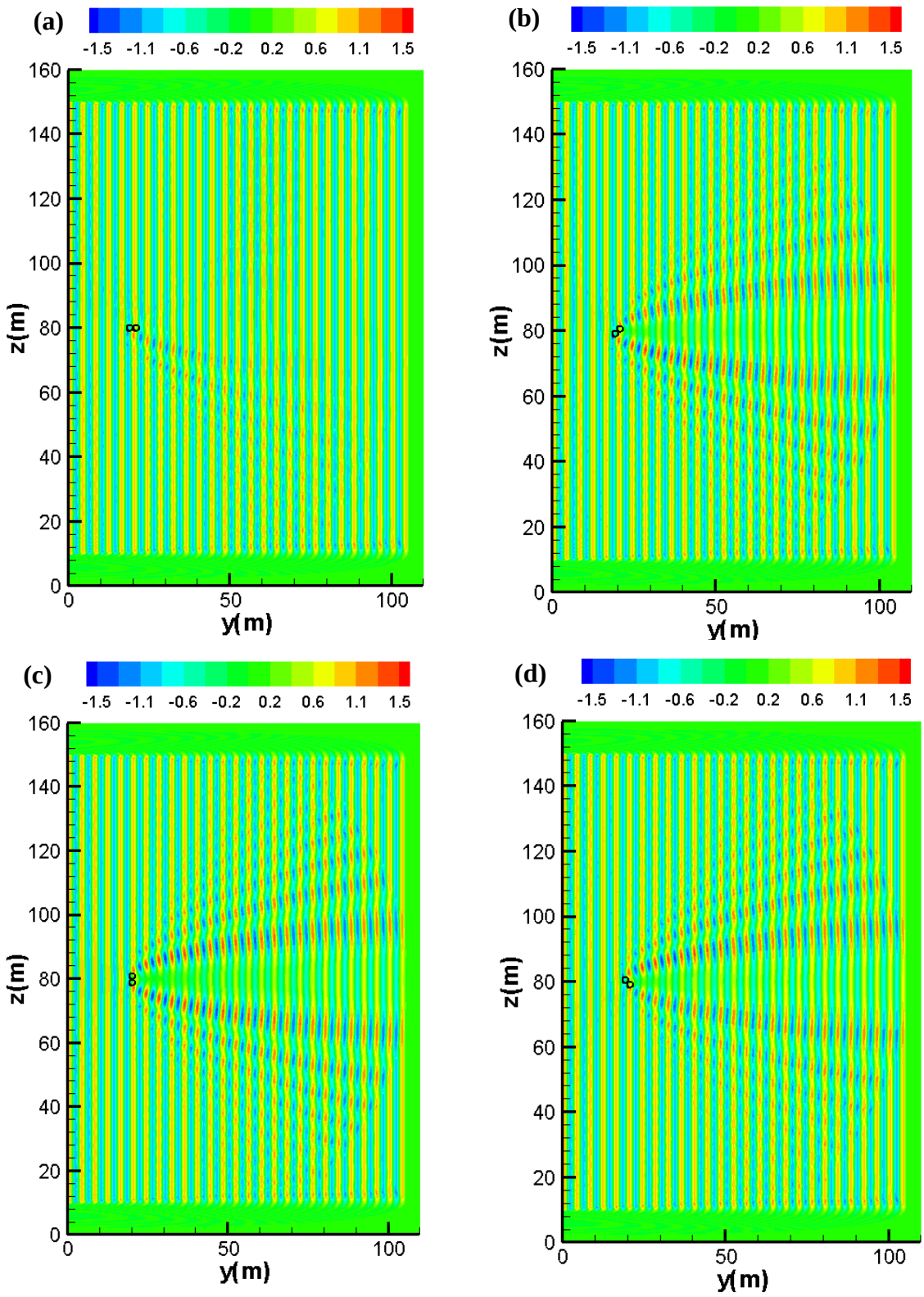
(a)
-1.5 -1.1 -0.6 -0.2 0.2 0.6 1.1 1.5
z(m)
y(m)
0 20 40 60 80 100 120 140 160
0 50 100
(b)
-1.5 -1.1 -0.6 -0.2 0.2 0.6 1.1 1.5
z(m)
y(m)
0 20 40 60 80 100 120 140 160
0 50 100
(c)
-1.5 -1.1 -0.6 -0.2 0.2 0.6 1.1 1.5
z(m)
y(m)
0 20 40 60 80 100 120 140 160
0 50 100
(d)
-1.5 -1.1 -0.6 -0.2 0.2 0.6 1.1 1.5
z(m)
y(m)
0 20 40 60 80 100 120 140 160
0 50 100

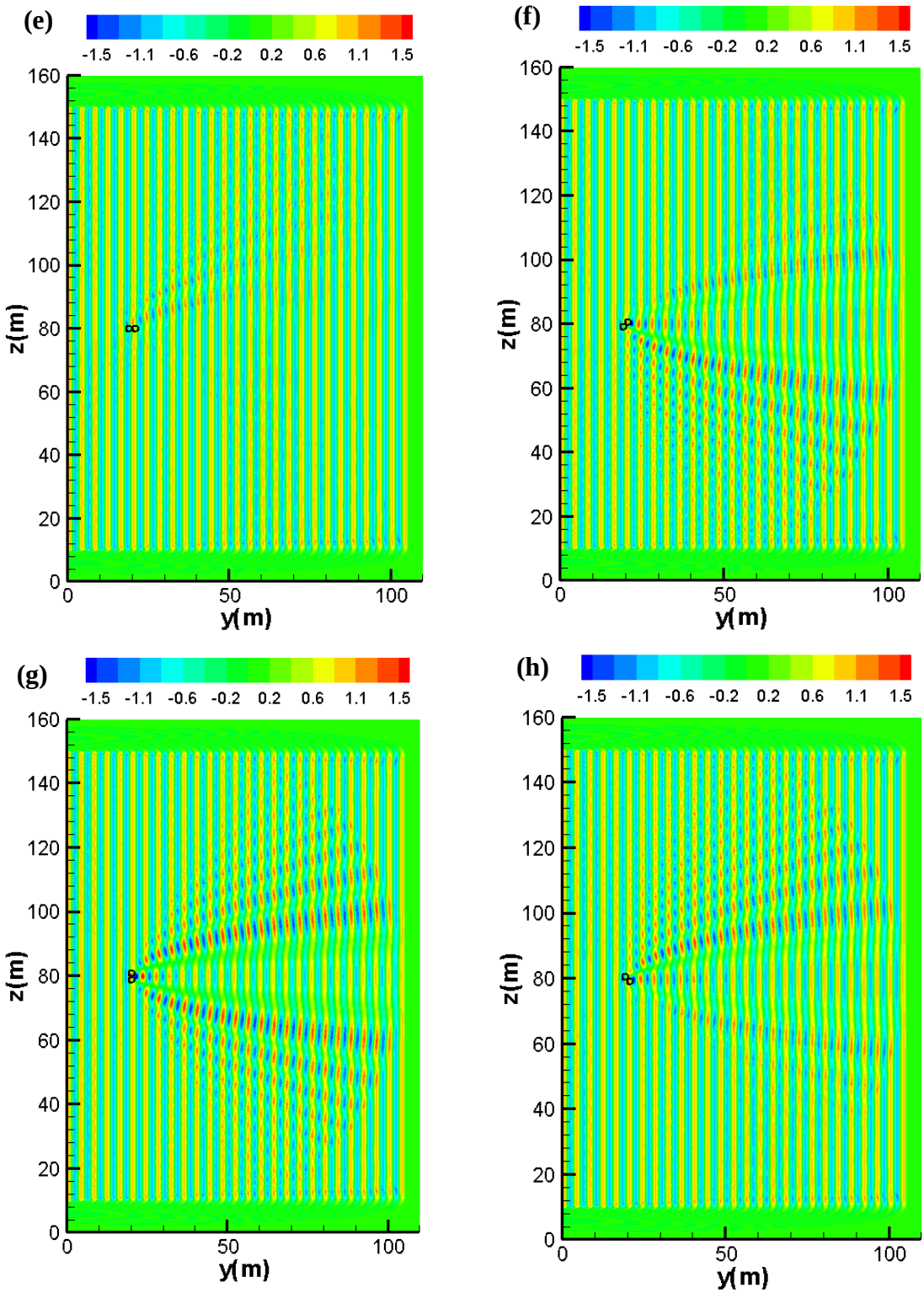

Fig. 3.8 Pressure contours at the moment t=0.31s with Mach number 0.25 for different angle ψ (a) 0.0 (b) 45 (c) 90 (d) 135 (e) 180 (f) 225 (g) 270 (h) 315.

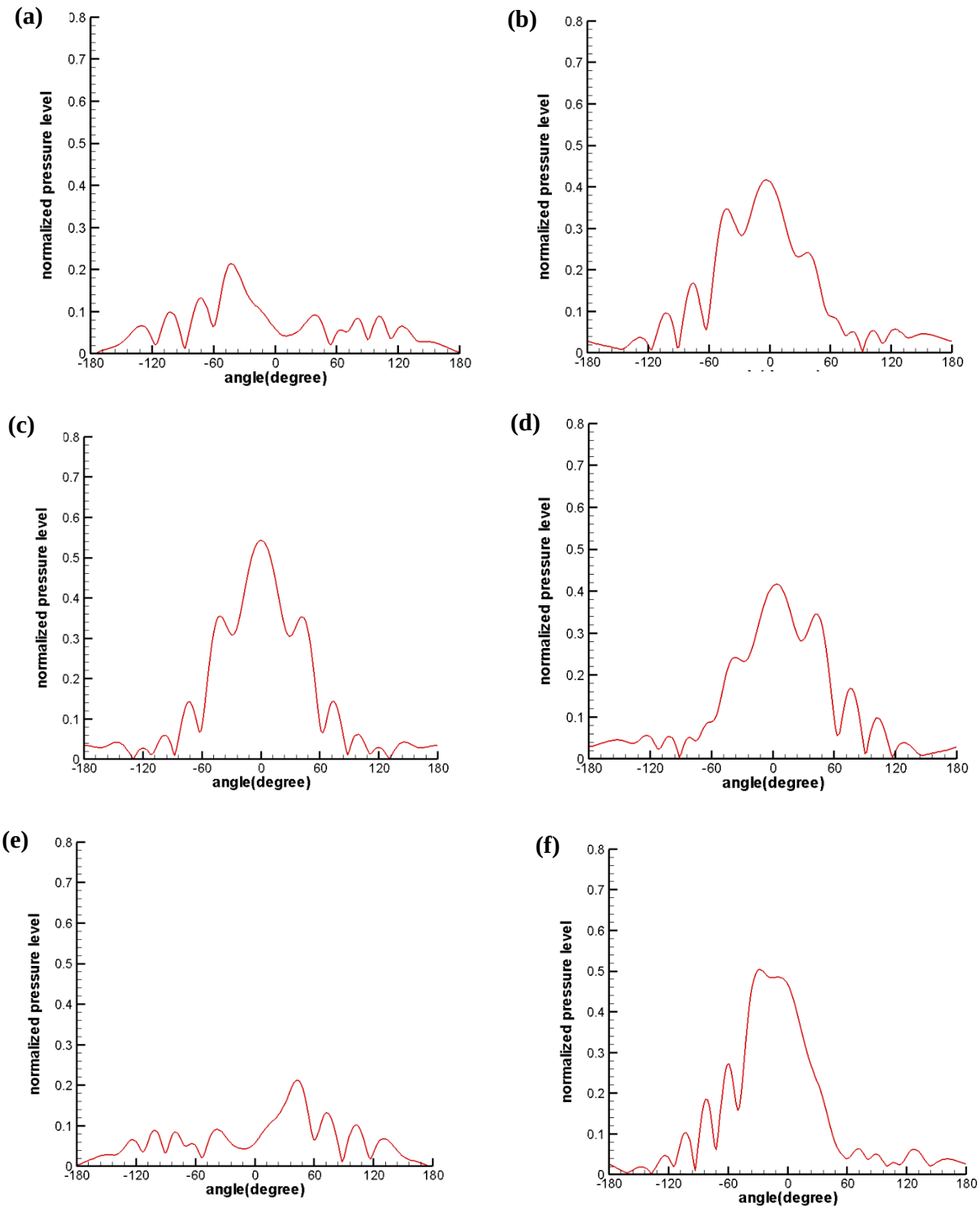
(a)
(b)
(c)
(d)
(e)
(f)
normalized pressure level
angle(degree)
0
0.1
0.2
0.3
0.4
0.5
0.6
0.7
0.8
-180
-120
-60
0
60
120
180

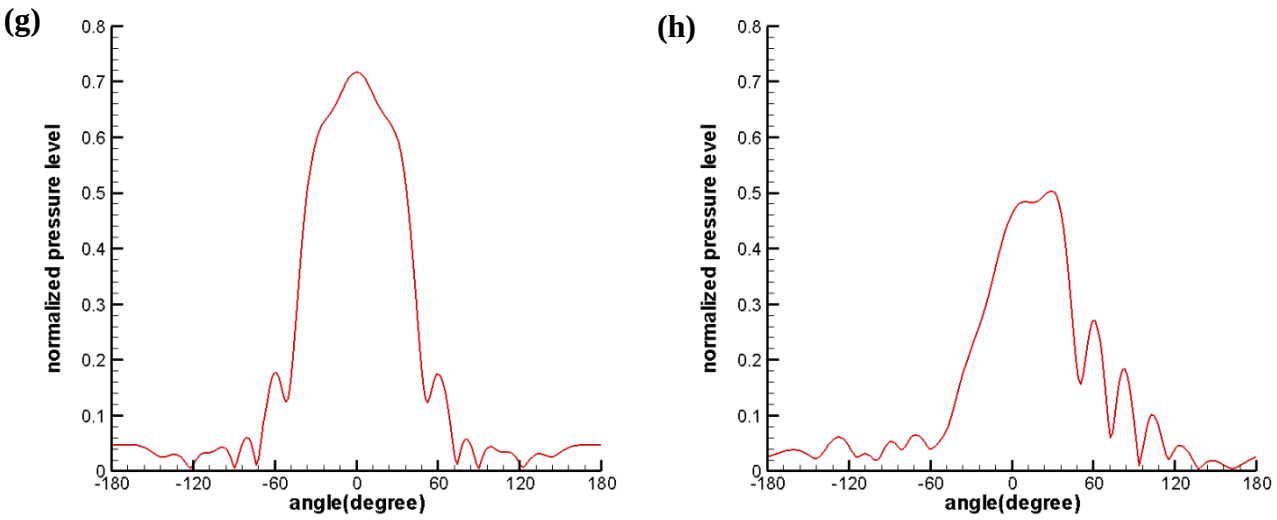

Fig. 3.9 Normalized pressure level with Mach number 0.25 for different angle ψ (a) 0 (b) 45 (c) 90 (d) 135 (e) 180 (f) 225 (g) 270 (h) 315.

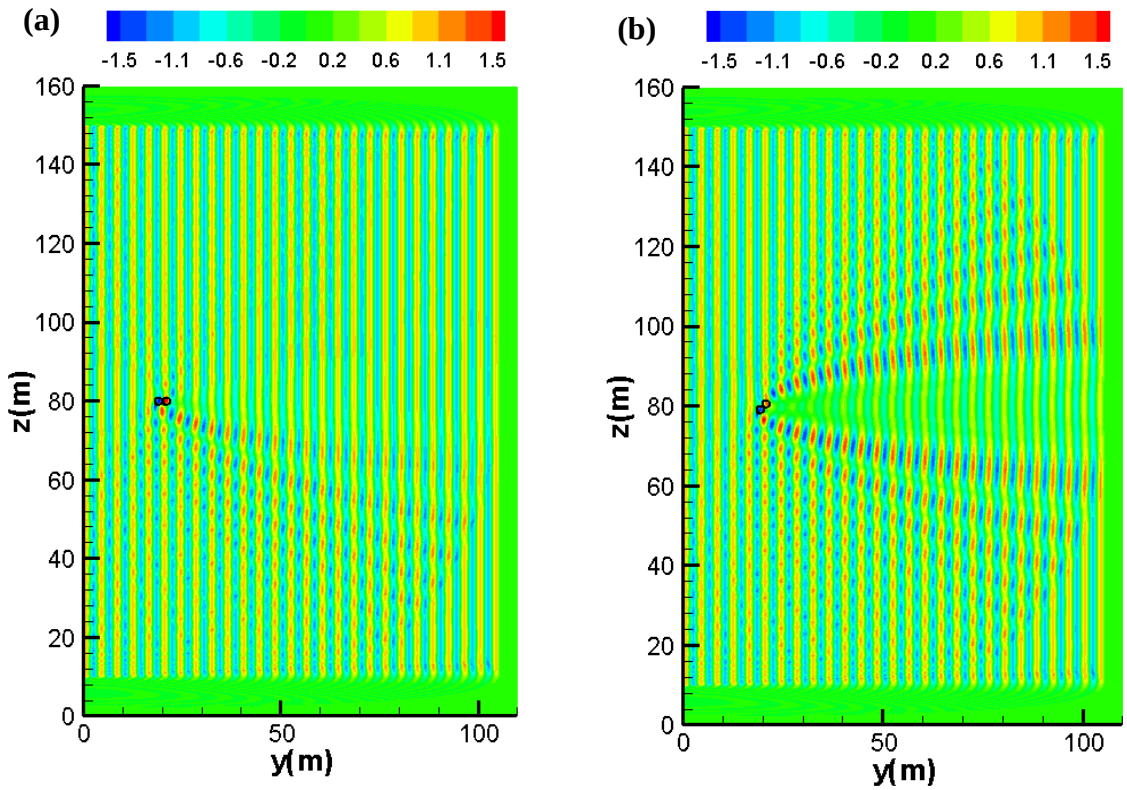

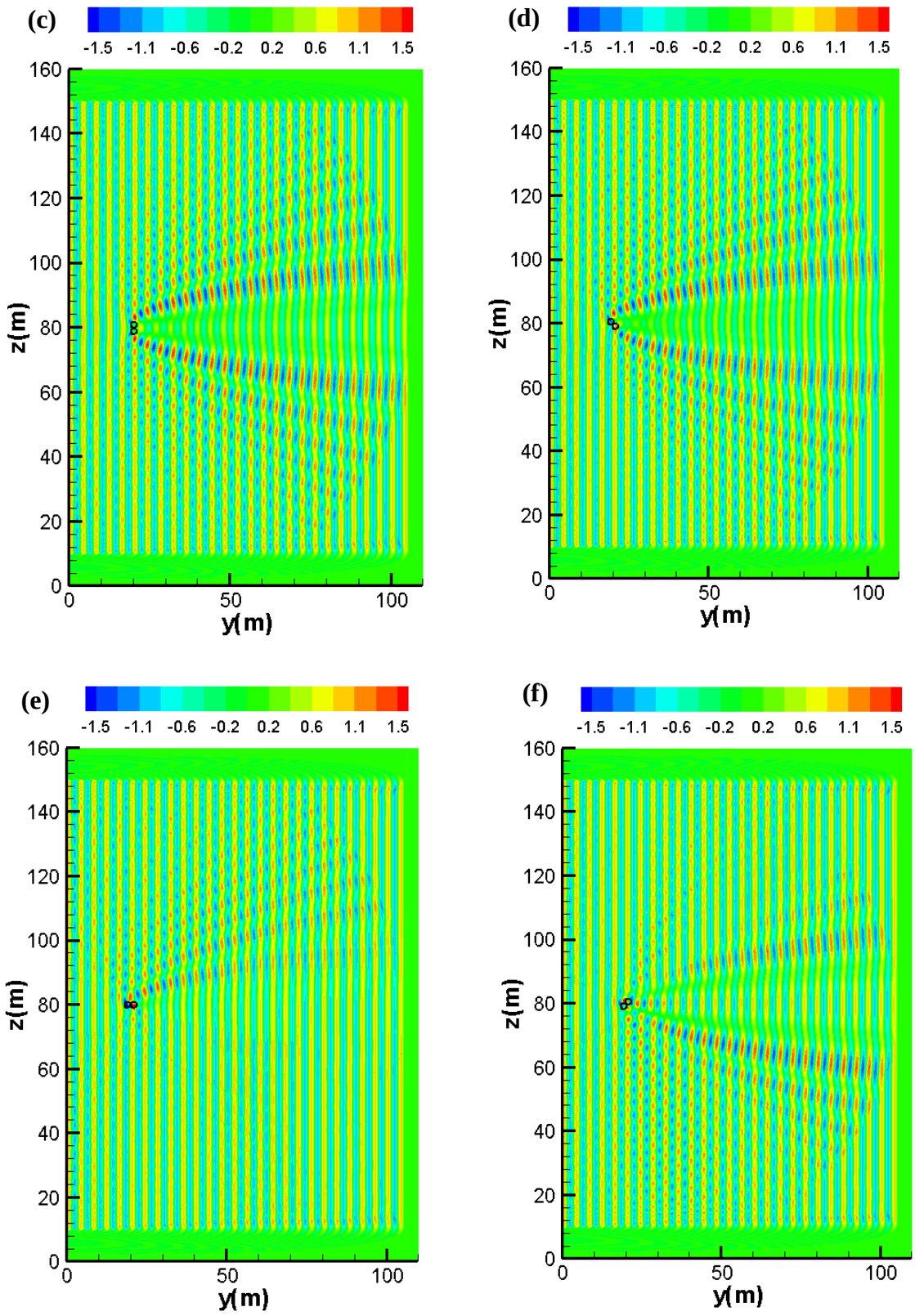
(c)
-1.5 -1.1 -0.6 -0.2 0.2 0.6 1.1 1.5
z(m)
y(m)
(d)
-1.5 -1.1 -0.6 -0.2 0.2 0.6 1.1 1.5
z(m)
y(m)
(e)
-1.5 -1.1 -0.6 -0.2 0.2 0.6 1.1 1.5
z(m)
y(m)
(f)
-1.5 -1.1 -0.6 -0.2 0.2 0.6 1.1 1.5
z(m)
y(m)

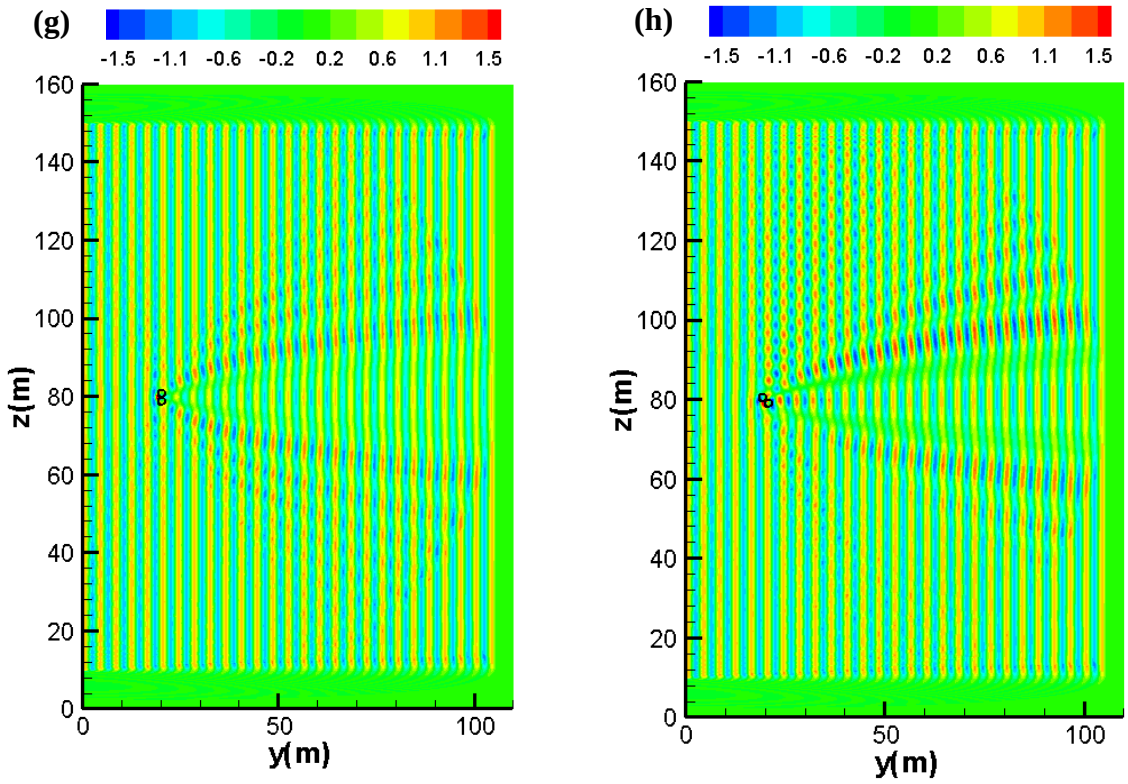

Fig. 3.10 Pressure contours at the moment t=0.31s with Mach number 0.5 for different angle ψ (a) 0.0 (b) 45 (c) 90 (d) 135 (e) 180 (f) 225 (g) 270 (h) 315.

Fig. 3.10 and 3.11 show the pressure contours and normalized pressure level curves respectively for relative high Mach number vortical flow, M=0.5. The sound scattering effects are much more obvious compared with the low Mach number vortex pair. Meanwhile the normalized pressure level distributions have the same phenomena as the low Mach number simulations except $\psi = 270°$. From Fig. 3.11 (g) we can see that when $\psi = 270°$ the normalized pressure level has a drop at location $\theta = 0°$ instead achieves the highest normalized pressure level. The explanation for this phenomenon can be found from the corresponding pressure contour. It is seen in Fig. 3.10 (g) that at the location $\theta = 0°$, in another word at (30, 80) the incident pressure is not greatly

influenced as much as the other Mach number. Thus the normalized pressure level curve no longer has the peak at $\theta = 0°$.

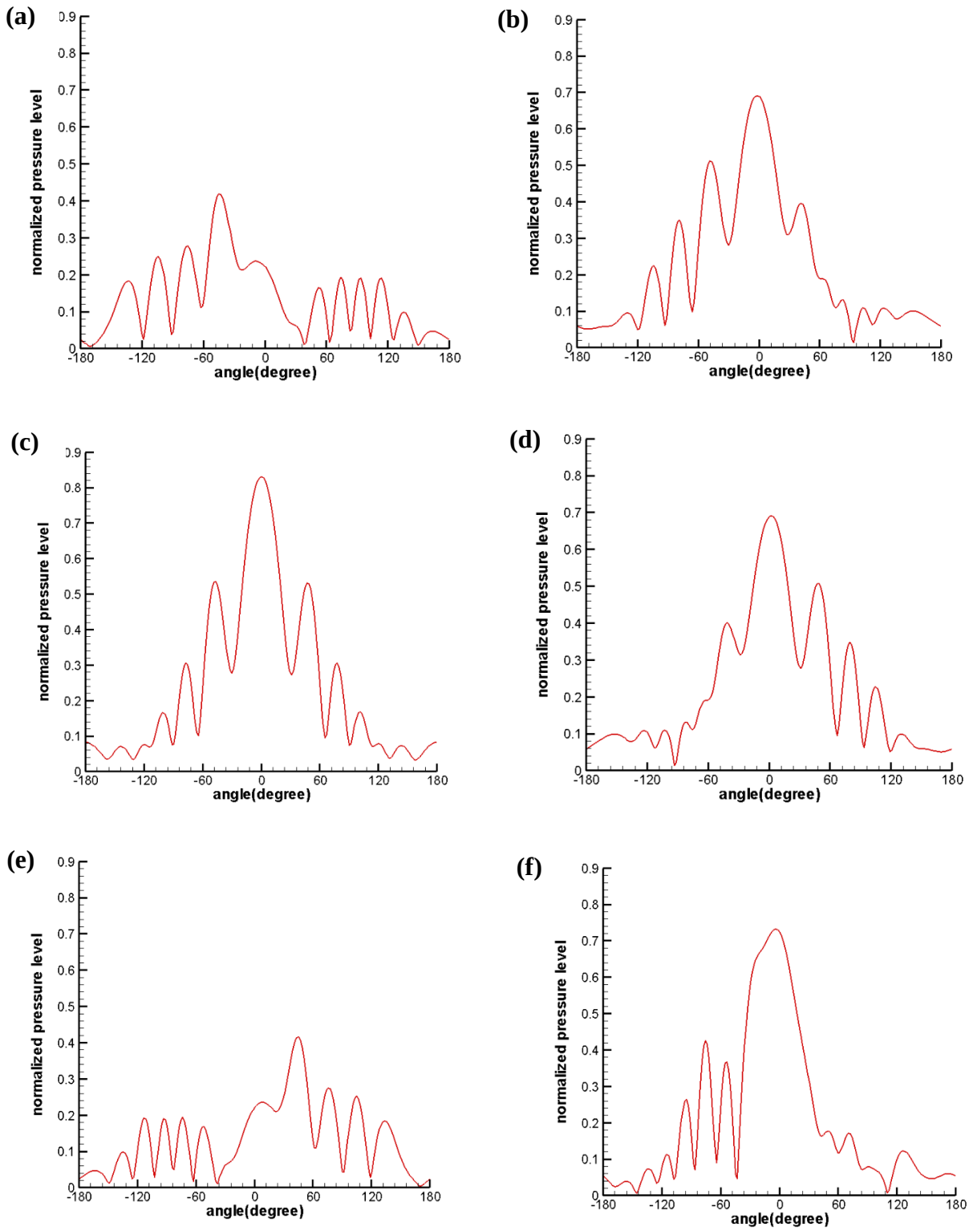

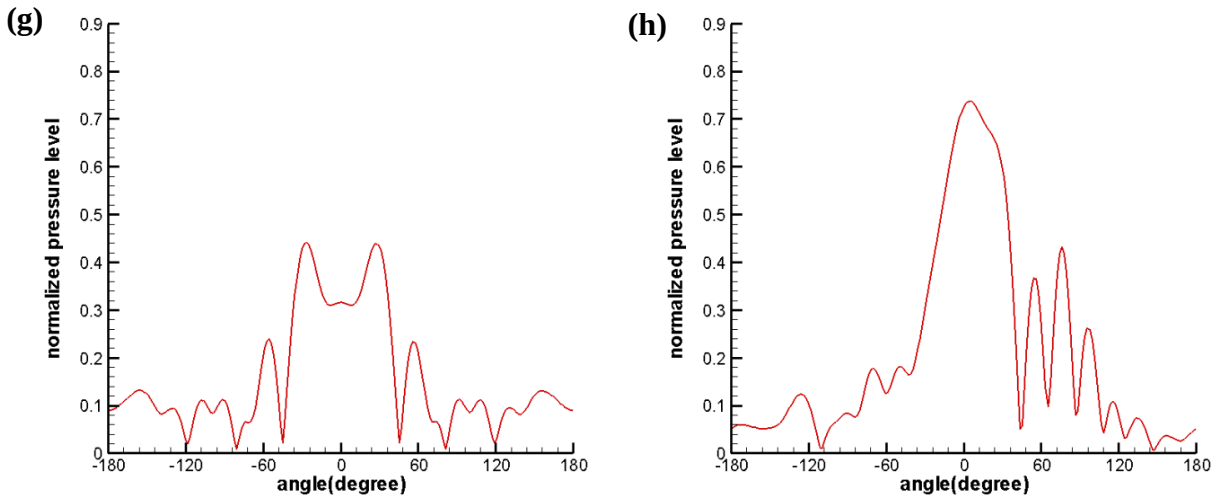

Fig. 3.11 Normalized pressure level with Mach number 0.5 for different angle ψ (a) 0 (b) 45 (c) 90 (d) 135 (e) 180 (f) 225 (g) 270 (h) 315.

Fig. 3.12 gives the relation between the Mach number of vortical flow and the normalized pressure level distributions for different ψ . Obviously the higher Mach number, the stronger sound scattering effects, which results in higher normalized pressure levels. One exception is that when $\psi = 270°$ the normalized pressure level of Mach number 0.5 at $\theta = 0°$ is lower than Mach number 0.125 and 0.5. And it has been discussed earlier.

Besides the currently receiving circle radius 10m, two different radius 8m and 12m are chosen for simulations with same vortex pair Mach number 0.25. Fig. 3.13 shows the relation between different radius and the corresponding numerical normalized pressure levels for different angle ψ from $0°$ to $180°$. This can be seen that the closer to the vortical flow, the higher normalized pressure level at the peak. Besides the magnitude, the phase of the scattered wave is also changed at different θ.

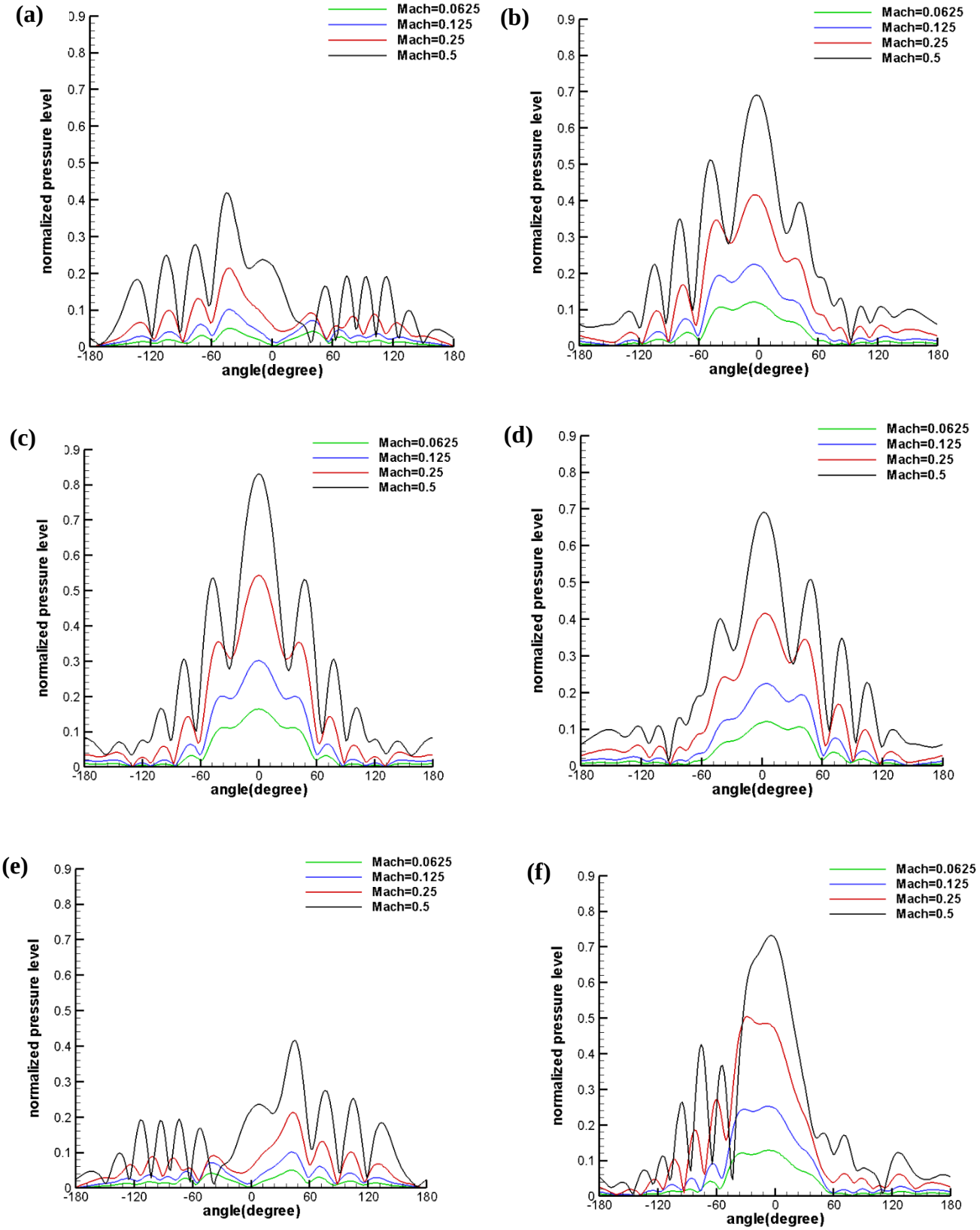
(a)
(b)
(c)
(d)
(e)
(f)
Mach=0.0625
Mach=0.125
Mach=0.25
Mach=0.5
normalized pressure level
angle(degree)
0
0.1
0.2
0.3
0.4
0.5
0.6
0.7
0.8
0.9
-180
-120
-60
0
60
120
180

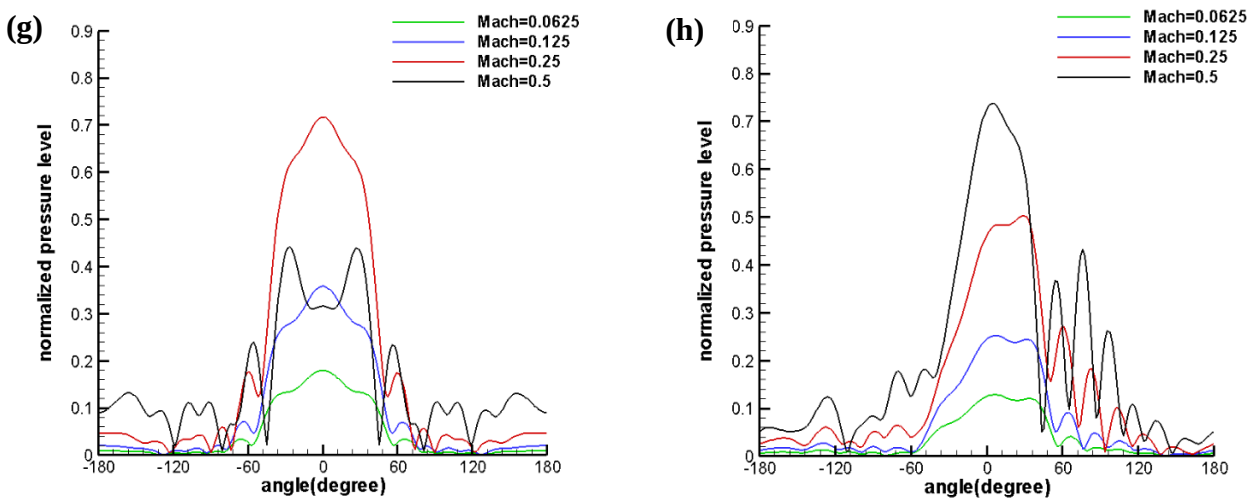

Fig. 3.12 Normalized pressure level comparison between different Mach numbers for different angle ψ (a) 0 (b) 45 (c) 90 (d) 135 (e) 180 (f) 225 (g) 270 (h) 315.

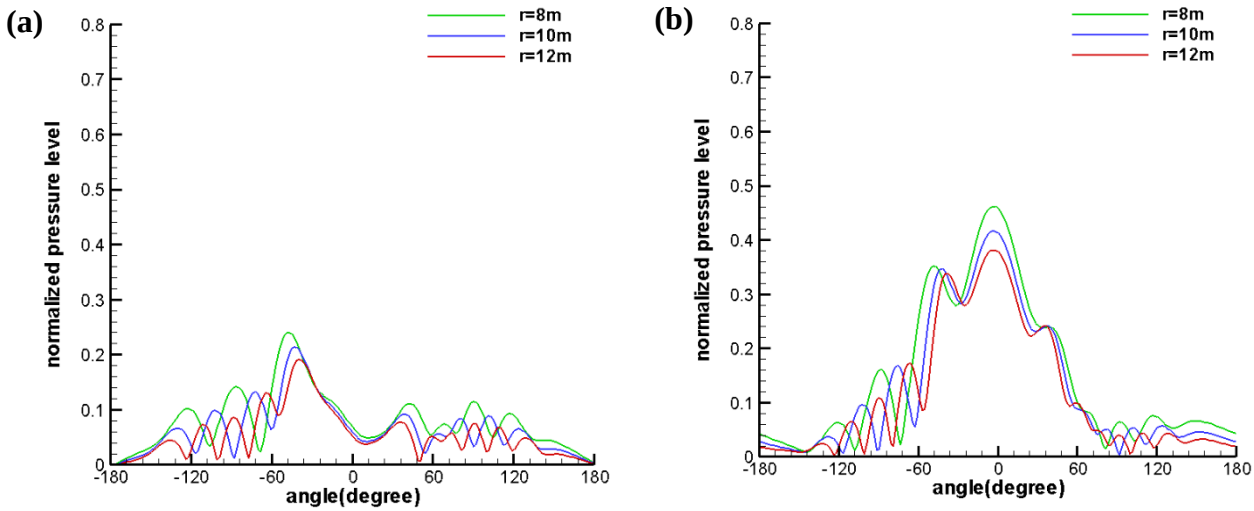

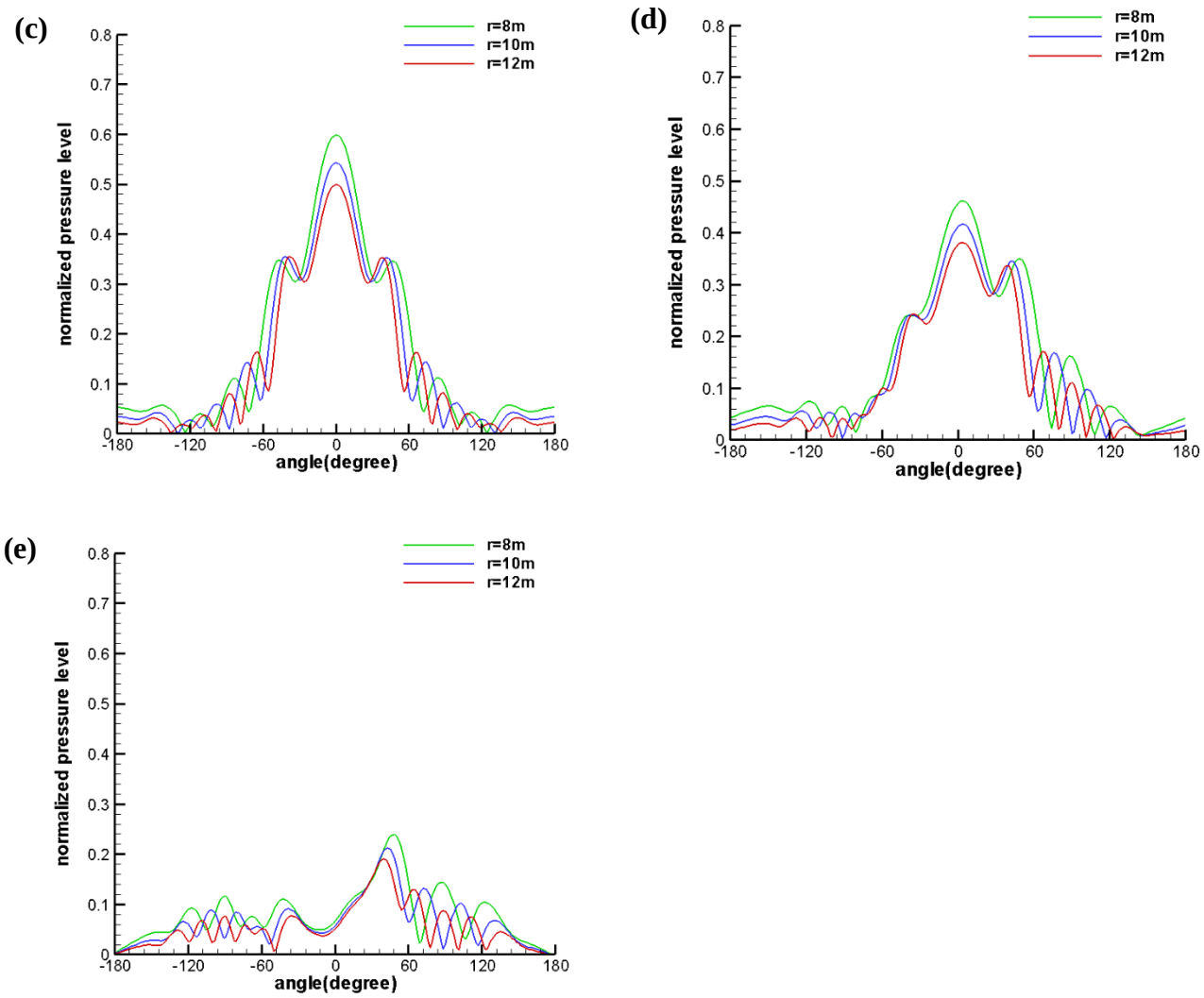

Fig. 3.13 Normalized pressure level at M=0.25 comparison between different angle ψ (a) 0 (b) 45 (c) 90 (d) 135 (e) 180.

Our single vortex results and the results in [71] indicated that for the single vortex case, when λ / r was constant, the root-mean-square pressure scaled with ε. Based on Fig. 3.14, when the ratio λ / r is a constant of 0.4 in our simulations, as ε is reduced, which means the Mach number becomes small, the curves appear to scale with ε. Based on Fig. 3.15, when Mach number is 0.0625, i.e. ε is a constant of 0.14, the curves appear to scale with the square root of λ / r when the receiver distance r is reduced. Therefore, the simulation results of the stationary vortex pair

case also agree with the low-frequency theory when the Mach number is low, as the single vortex case.

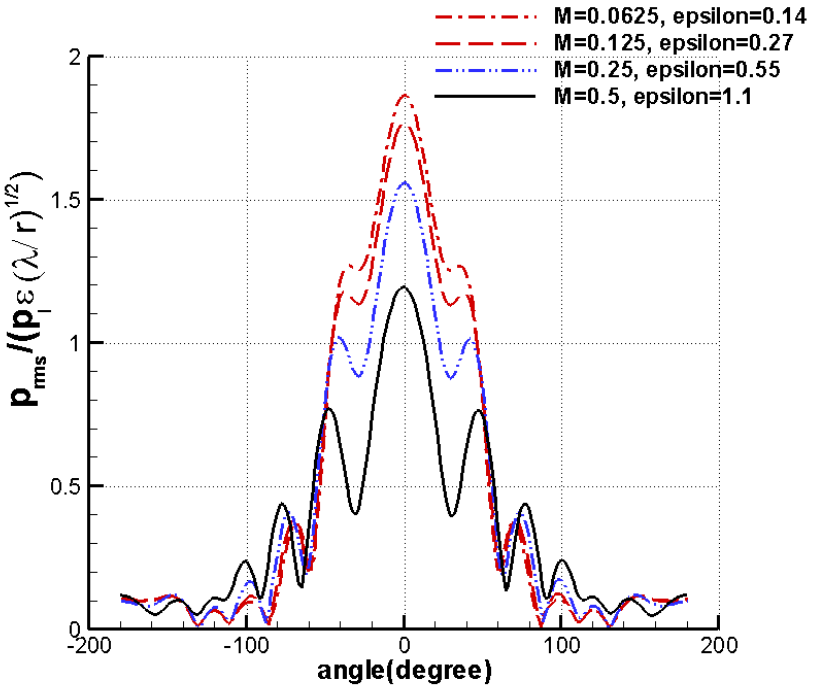

Fig. 3.14 Root-mean-square pressure level at r =10m normalized by $p_I\varepsilon(\lambda/r)^{1/2}$.

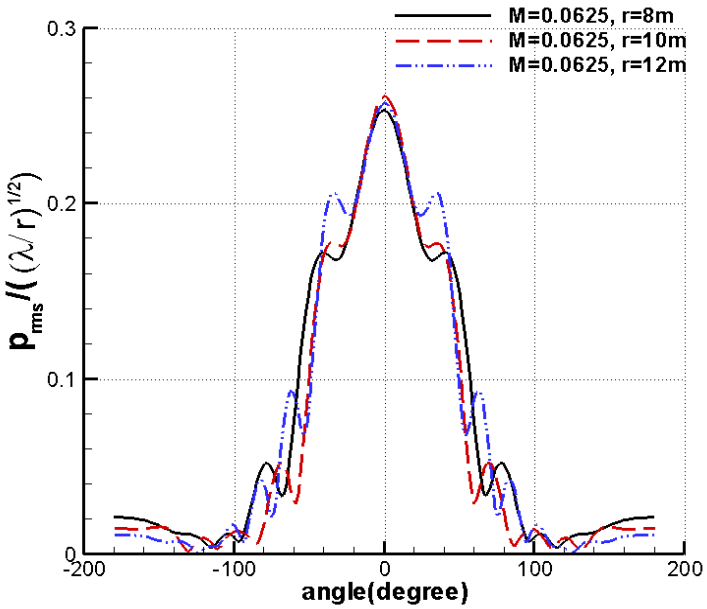

Fig. 3.15 Root-mean-square pressure level at M=0.0625 normalized by $(\lambda/r)^{1/2}$.

3.4 Moving Vortex Pair Simulation

Besides the stationary vortex pair, in this section the sound scattering effects of a moving vortex pair are studied. First, the theoretical analysis for the scattering of a plane sound wave by a moving vortex pair in Ref. [114] is represented, after that the corresponding numerical simulations are conducted and the numerical results are compared with analytical solutions.

3.4.1. Analytical Analysis

The analytical solutions represented in Ref. [114] deal with the two dimensional scattering of a plane wave by a vortex pair, in the homentropic flow where any viscous dissipation is absent. And the vortex strength is supposed to be sufficiently small in Ref. [114], in another word the analytical solution is feasible for low Mach number steady motion of the vortex pair. It is noted that the singularity of the scattering does not occur for the vortex pair, in contrast to a single vortex. An acoustic potential of the incident sound wave is assumed as:

$$\phi_1 = p_I \exp\left[i\left(\vec{k}_0 \cdot \vec{y} - \omega_0 t\right)\right] \tag{3.14}$$

where p_I is the amplitude of the incident wave, k_0 is the wave number defines as $2\pi / \lambda$, $\vec{y} = (y, z)$ is the two-dimensional Cartesian coordinates of the receiver location, and ω_0 is the angular frequency of the plane wave with $\omega_0 = 2\pi f$. When the vortex pair with strength Γ and $-\Gamma$ are located at (Vt, d) and $(Vt, -d)$ respectively at time t, the vorticity ω and the flow velocity $\vec{u} = (u_1, u_2)$ induced are given by:

$$\omega = \left(0, 0, \Gamma\delta\left(y - Vt\right)\left[\delta\left(z - d\right) - \delta\left(z + d\right)\right]\right) \tag{3.15}$$

$$u_1 = \frac{\Gamma d}{\pi} \frac{\left(y - Vt\right)^2 - z^2 + d^2}{\left[\left(y - Vt\right)^2 + \left(z - d\right)^2\right]\left[\left(y - Vt\right)^2 + \left(z + d\right)^2\right]} \tag{3.16}$$

$$u_2 = \frac{\Gamma d}{\pi} \frac{2(y-Vt)z}{\left[(y-Vt)^2+(z-d)^2\right]\left[(y-Vt)^2+(z+d)^2\right]} \tag{3.17}$$

where δ is Dirac delta function and V is defined as the vortex pair self-induced moving velocity:

$$V = \frac{\Gamma}{4\pi d} \tag{3.18}$$

and $2d$ is the distance of centers of vortex pair.

Finally we have the expression for scattered pressure p_s:

$$p_s = \exp\left(\frac{3i}{4}\right) 2\rho\omega_0 p_I M d\sqrt{2\pi k_0}\sin\left[k_0 d\left(\frac{z}{\sqrt{(y-Vt)^2+z^2}} - \sin\psi\right)\right]$$

$$\times \frac{\left[z\cos\psi-(y-Vt)\sin\psi\right]\left[(y-Vt)\cos\psi+z\sin\psi\right]}{\left[(y-Vt)^2+z^2\right]^{3/4}\left[(y-Vt)\cos\psi+z\sin\psi-\sqrt{(y-Vt)^2+z^2}\right]}$$

$$\times\exp\left[i(1-M\cos\psi)(k_0\sqrt{(y-Vt)^2+z^2}-\omega_0 t\right] \tag{3.19}$$

More details of the derivation for Eq. (3.19) can be found in Ref. [114].

3.4.2. Numerical Simulations and Results

In the numerical simulations for moving vortex pair cases, the vortex parameters are the same as the stationary vortex cases. The far field receiver location is changed to further location: *r*=50m, so that the moving vortex pair is contained inside the receiver circle. The initial simulation conditions like domain size, grid size, time step and time domain are kept the same the simulations for stationary vortex pair. The center of the receiving circle is located at (55m, 80m), and the vortex orientation angle $\psi = 90°$.

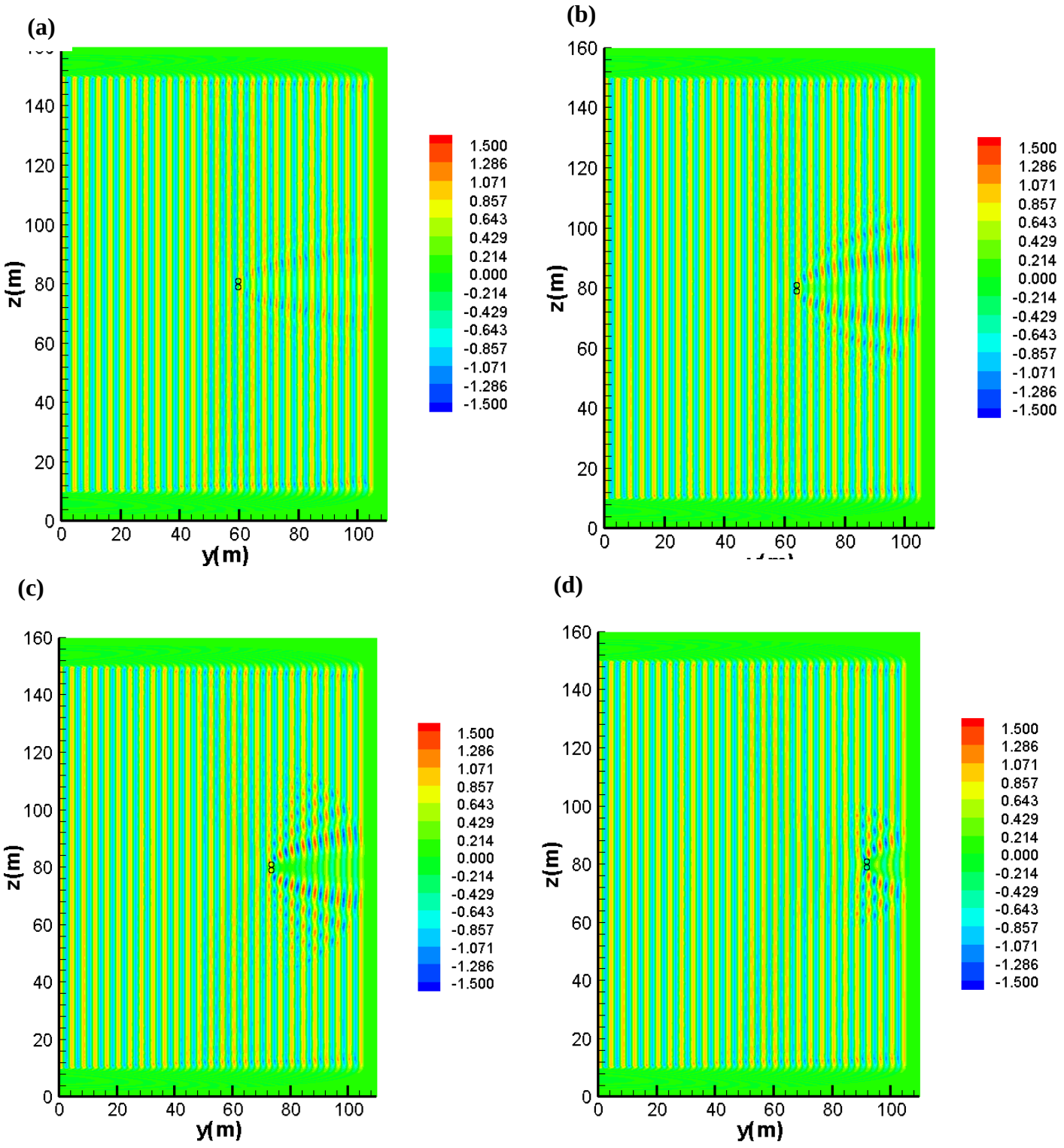

Fig. 3.16 Pressure contours of moving vortex pair at the moment *t*=0.31s

(a) M=0.0625, (b) M=0.125, (c) M=0.25, (d) M=0.5.

Pressure contours of moving vortex pair simulations at time 0.31s are provided in Figs. 3.16 (a)-(d) for the four Mach numbers. First we can find that the vortex pair with a higher Mach number has a stronger sound scattering effect. According to Eq. (3.18), the moving vortex pair with a higher Mach number has higher moving velocity. Therefore as Mach number increases, the vortex pair is closer to the receiver which is at $\theta = 0°$, and the scattered area is smaller.

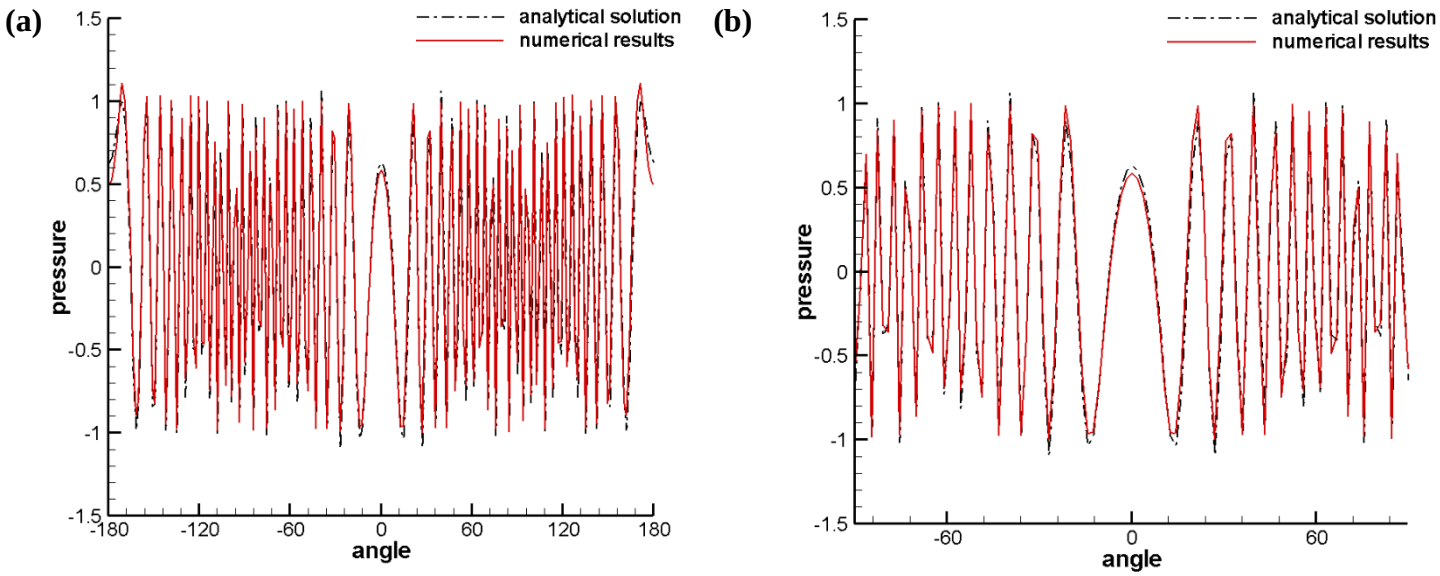

Fig. 3.17 Simulated pressure with moving vortex pair when M=0.0625 in comparison with analytical solutions

The analytical solution presented in Ref. [114] are applicable for low Mach number steady motion of the vortex pair. As a result, the simulated pressure at time *t*=0.31s of the moving vortex pair with Mach number 0.0625 is compared with the analytical solutions, and the comparison is given in Fig. 3.17. Fig. 3.17 (a) gives the pressure distributions for all the receivers, and Fig. 3.17 (b) shows the distribution at the receiver direction angle range of $-90° \le \theta \le 90°$ so that the

comparison can be observed more clearly. We can see that the numerical results have a very good agreement with the analytical solutions.

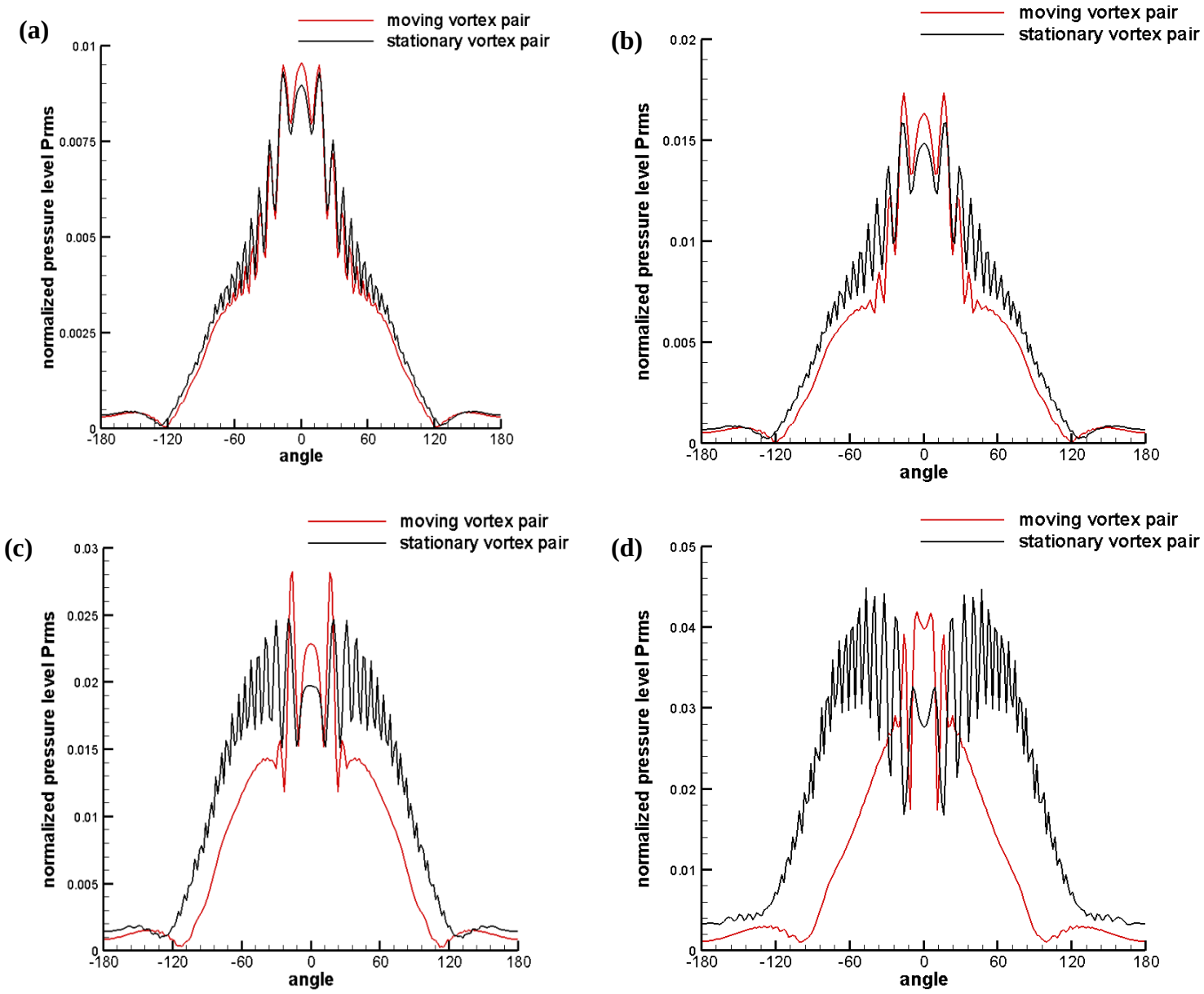

Fig. 3.18 Normalized pressure level comparison between moving vortex pair and stationary vortex pair (a) M=0.0625 (b) M=0.125 (c) M=0.25 (d) M=0.5.

Fig. 3.18 gives the normalized pressure level of the moving vortex pair cases in comparison with the stationary vortex pair cases. First, when the Mach number is lower, the two curves are closer because the distance between the stationary vortex pair and the moving vortex is smaller. For the stationary vortex pair, when the Mach number is 0.0625, the highest normalized pressure level is obtained at the location $\theta = 0°$. As the Mach number increases, the scattering effect becomes much stronger at the two sides of the location $\theta = 0°$. By observing the normalized pressure level at $\theta = 0°$, we can find that the difference between moving and stationary vortex pair cases becomes larger as the Mach number increases. This is because the moving vortex pair is closer to the receiver at $\theta = 0°$ and further away from the stationary vortex pair when the Mach number is higher.

3.5 Summary

In this chapter, propagations of plane waves through a single vortex and a vortex pair is studied. To handle with the high convection effect resulting from the background vortical flow, a fifth order WENO scheme is applied. The results of the single vortex simulations have a good agreement with the literature data. Then, the simulations are implemented for both stationary and moving vortex pair cases. For a fixed vortex pair orientation angle ψ, the results show that the sound scattering effect becomes stronger as the Mach number increases. The scaling laws for the low frequency sound wave seem to apply under the low Mach number vortical flow condition. The accuracy of the numerical scheme is validated by the good agreement between the simulated results and the analytical solutions.

4 Ultrasound Propagation Simulations in Biological Tissue

During the past decades the mechanisms and models of ultrasonics have caused a lot of interests, and the derivation of wave equations to model acoustic absorption and dispersion in biological tissue has continued to be subject of research interest. The biological tissue is considered as a kind of lossy media with acoustic attenuation, whether caused by molecular relaxations or scattered by small random particles in Ref. [127]. Many algorithms for ultrasound have been developed in Ref. [128]-[130]. Algorithms that compensate for attenuation in the background media are found in Ref. [128] and [131]. Sophisticated techniques for determining the exact values of attenuation and dispersion are given in Ref. [132]-[133]. The wave propagation in biological tissue media in which the absorption follows a frequency power law in Ref. [134] has many important applications in biomedical ultrasonics. Acoustic attenuation in biological tissue generally satisfies a power law relationship such that attenuation increases with frequency according to some noninteger exponent in Ref. [127].

In this chapter, the linearized Euler acoustic equations in Ref. [92] which used in the previous chapters are incorporated with space-fractional Laplacian operators in Ref. [135] for the ultrasound simulations. The finite forward difference scheme is applied for velocity and backward difference scheme is applied for pressure on non-fractional derivative operator terms in spatial discretization.

4.1 Theoretical Model with Fractional Laplacian Operators

For the ultrasound propagation in biological tissue simulations in this chapter, we simplify the tissue to be consisted of two kinds of media: water and bone. The governing equations for the wave propagation in water are the general Linearized Euler equations in Ref. [134] with no fractional Laplacian operators:

$$\frac{\partial \vec{u}}{\partial t} = -\frac{1}{\rho_0}\nabla p \tag{4.1}$$

$$\frac{\partial p}{\partial t} = -\rho_0 c_0^2 \nabla \cdot \vec{u} \tag{4.2}$$

where $\vec{u}$ is the acoustic velocity, ρ_0 is the density of water, and c_0 is the sound propagating speed in water. The governing equations for the wave propagation in bone material are given like below:

$$\frac{\partial \vec{u}}{\partial t} = -\frac{1}{\rho_1}\nabla p \tag{4.3}$$

$$\frac{\partial p}{\partial t} = -\rho_1 c_1^2 \nabla \cdot \vec{u} + \tau c_1^2 (-\nabla^2)^{y/2} p + \eta \rho_1 c_1^2 (-\nabla^2)^{\frac{y+1}{2}-1} (\nabla \cdot \vec{u}) \tag{4.4}$$

where ρ_1 is the density of bone, and c_1 is the sound propagating speed in bone. The y is a noninteger power law exponent for fractional Laplacian derivative, τ and η are proportionality coefficients in Ref. [134].

Table 4-1 Different power law exponent and corresponding proportionality coefficients

y	τ	η
1.5	-4.90368e-8	-9.80736e-5
1.9	-1.95732e-9	-6.20019e-7

For the two-dimensional simulations, consider the Riesz fractional derivative in Ref. [135] equals to the fractional Laplacian operator given below:

$$-(-\nabla^2)^{\alpha/2} p = \frac{\partial^\alpha p}{\partial |y|^\alpha} + \frac{\partial^\alpha p}{\partial |z|^\alpha} \tag{4.5}$$

where α is the power law exponent. If $0 < \alpha < 1$, the standard Grunwald approximation method in Ref. [135] is given as:

$$\frac{\partial^\alpha p}{\partial |y|^\alpha} = -\frac{1}{2\cos(\frac{\pi\alpha}{2})\Delta y^\alpha} (\sum_{j=0}^{l} g_j p_{l-j} + \sum_{j=0}^{N-l} g_j p_{l+j}) \tag{4.6}$$

where Δy is numerical grid size, and g_j is called weight coefficient. The expression for weight coefficient is given as:

$$g_j = \begin{cases} 1, & j = 0 \\ (-1)^j \dfrac{\alpha(\alpha-1)...(\alpha-j+1)}{j!}, & j = 1, 2, ..., N \end{cases} \tag{4.7}$$

If $0 < \alpha < 1$, the standard Grunwald approximation method in Ref. [135] is given as:

$$\frac{\partial^\alpha p}{\partial |y|^\alpha} = -\frac{1}{2\cos(\frac{\pi\alpha}{2})\Delta y^\alpha} (\sum_{j=0}^{l+1} g_j p_{l-j+1} + \sum_{j=0}^{N-l+1} g_j p_{l+j-1}) \tag{4.9}$$

And the weight coefficient is given as:

$$g_j = \begin{cases} 1, & j = 0 \\ (-1)^j \dfrac{\alpha(\alpha-1)...(\alpha-j+1)}{j!}, & j = 1, 2, ..., N \end{cases} \tag{4.10}$$

Different power law exponent values y, the corresponding proportionality coefficients are listed in Table. 4.1. For the numerical simulations in the following section, the power law exponent is chosen as 1.9.

4.2 Ultrasound Propagation in Biological Tissue Simulations

The geometry and coordinate system for the ultrasonic wave propagation in biological tissue are shown in Fig. 4.1. The computational domain size is $0.06\text{m} \times 0.06\text{m}$, and uniform grid is implemented with very small mesh size $\Delta y = \Delta z = 5 \times 10^{-5}\text{m}$. The four boundaries of computational domain are specified as rigid boundary.

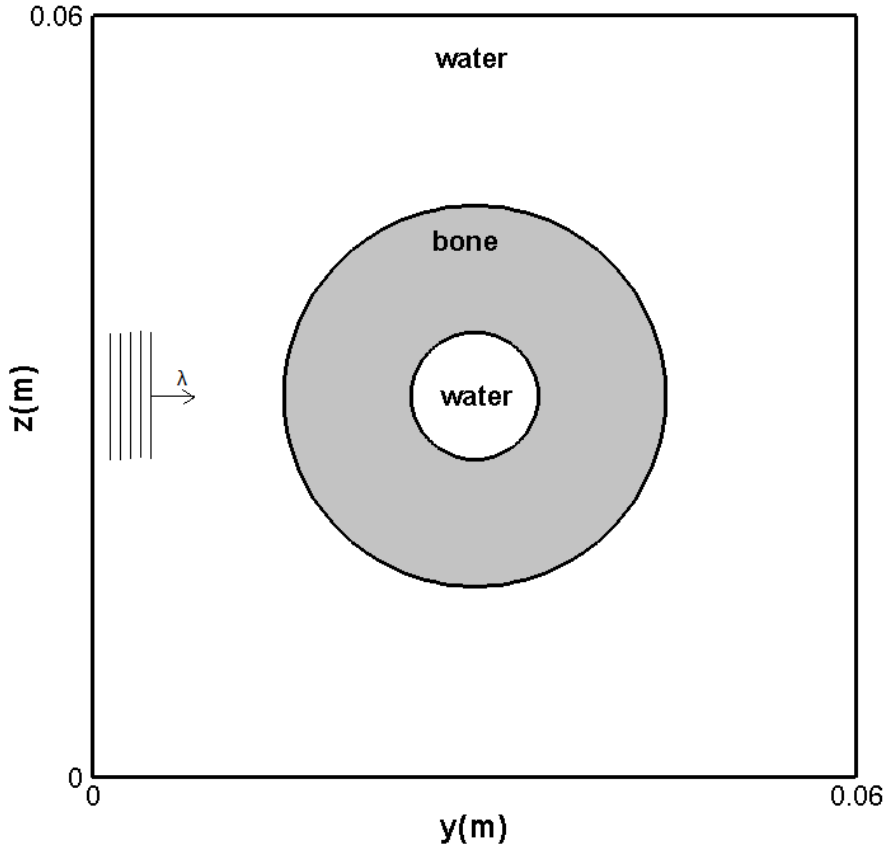

Fig. 4.1 Description of the geometry and coordinate system for the ultrasound wave propagation.

As it is shown in Fig. 4.1 the domain is consisted with two different materials water and bone. The bone area is between two concentric circles. The center of two concentric circles is at the center of the computational domain (0.03, 0.03) and radius is 0.015m and 0.005m respectively.

The ultrasound propagation speed in water and bone is 1500m/s and 2000m/s respectively, and the density of water and bone media is 1000kg/m^3 and 1500kg/m^3 respectively.

For the ultrasonic wave propagation simulations, the time step is chosen as an extremely small value $\Delta t = 5\times10^{-9}\text{s}$. Simulation step is 7600 and time domain is $t = 38\mu\text{s}$. A receiver is put at the center of the computational domain (0.03, 0.03). The ultrasonic plane wave is set at the left boundary of the domain from $z = 0.025\text{m}$ to $z = 0.035\text{m}$. The expression for ultrasonic plane wave in Ref. [127] is given as:

$$p(t) = \cos(2\pi f_0 t)[1-\cos(2\pi f_1 t)] \tag{4.11}$$

where f_0 is the center frequency which is chosen as $f_0 = 1.3\text{MHz}$, and frequency f_1 controls the plane wave bandwidth, which is chosen as $f_1 = 0.2\text{MHz}$. This input ultrasonic wave with specified frequency is shown in Fig. 4.2.

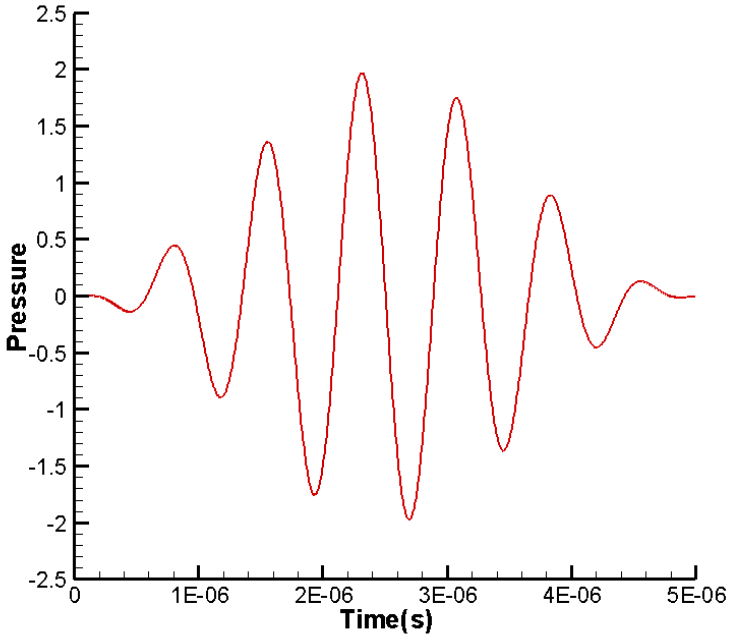

Fig. 4.2 Input ultrasonic plane wave.

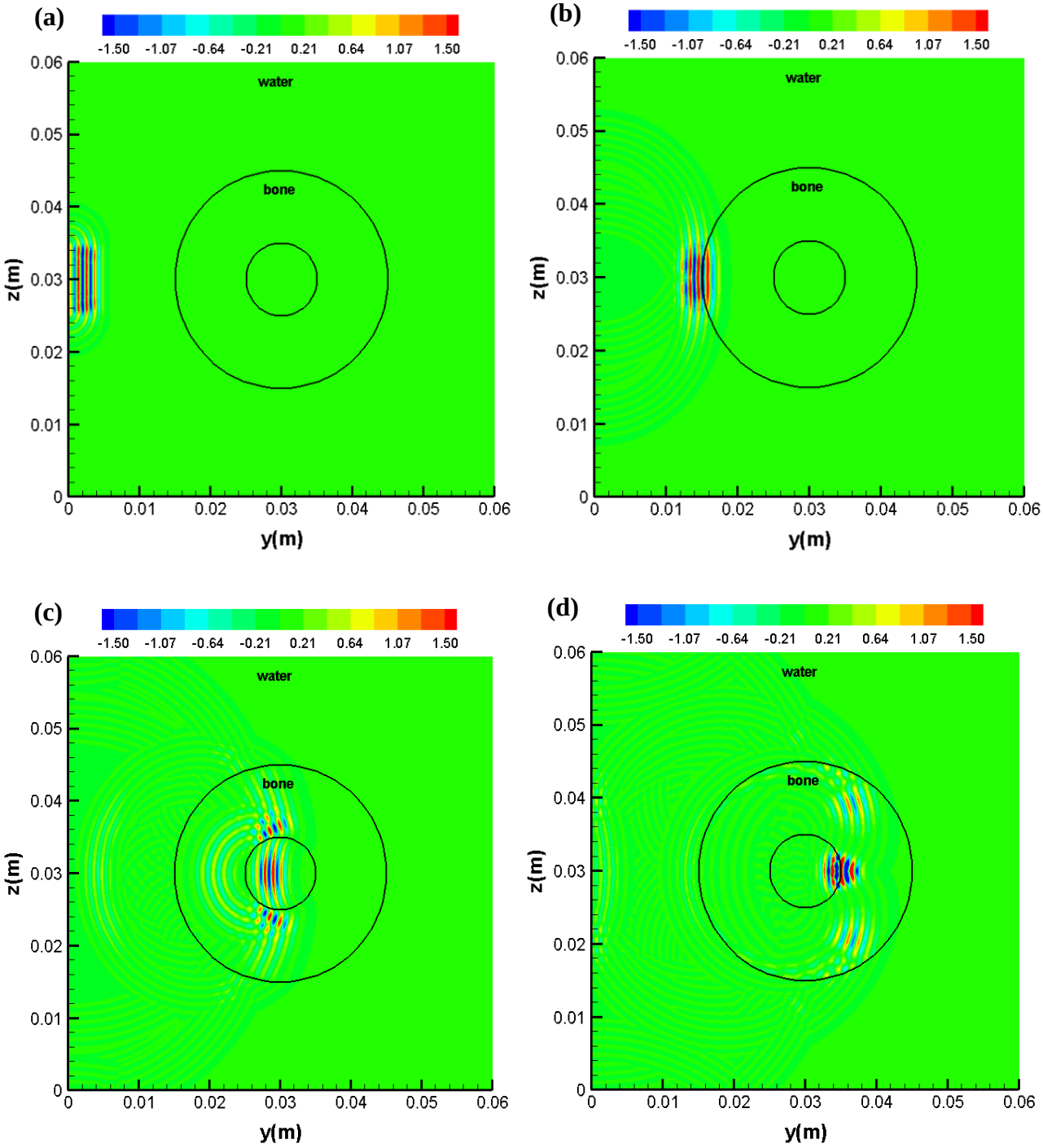
(a)
-1.50 -1.07 -0.64 -0.21 0.21 0.64 1.07 1.50
water
bone
z(m)
y(m)
0 0.01 0.02 0.03 0.04 0.05 0.06
(b)
-1.50 -1.07 -0.64 -0.21 0.21 0.64 1.07 1.50
water
bone
z(m)
y(m)
0 0.01 0.02 0.03 0.04 0.05 0.06
(c)
-1.50 -1.07 -0.64 -0.21 0.21 0.64 1.07 1.50
water
bone
z(m)
y(m)
0 0.01 0.02 0.03 0.04 0.05 0.06
(d)
-1.50 -1.07 -0.64 -0.21 0.21 0.64 1.07 1.50
water
bone
z(m)
y(m)
0 0.01 0.02 0.03 0.04 0.05 0.06

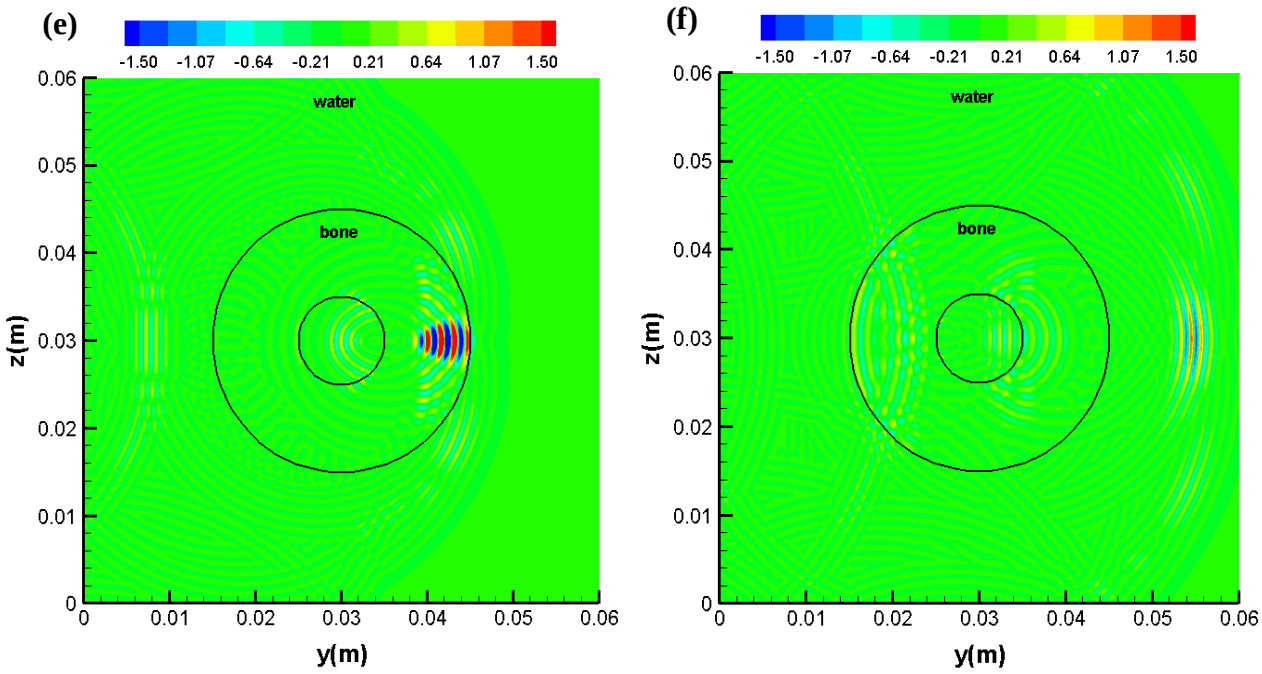

Fig. 4.3 Pressure contours of ultrasound propagation at different moments (a) $t = 4\mu s$ (b) $t = 12\mu s$ (c) $t = 20\mu s$ (d) $t = 24\mu s$ (e) $t = 28\mu s$ (f) $t = 30\mu s$.

Fig. 4.3 (a)-(f) are the pressure contours at six different moments. How the ultrasonic wave propagation and are attenuated through the biological tissue model can be clearly observed. We can find several reflections when the ultrasonic wave enters the bone media, and the absorption and dispersion of the wave inside the bone due to the fractional Laplacian. Based on Fig. 4.3 (f) it is seen that after the ultrasonic wave pass through the bone media, it becomes much weaker compared to the incident plane wave. Meanwhile there are several reflected waves remain inside the bone.

The numerical pressure versus time of the receiver (0.03, 0.03) is given in Fig. 4.4. The numerical pressure simulated without bone media is also shown in Fig. 4.4 for comparison. From

the figure we can see that the with-bone numerical pressure curve has smaller magnitude than the without-bone curve. It is due to the reflections at the interface between water and bone media, and also the dispersions inside the bone. Except the magnitude, the with-bone curve is also shifted compared with the without-bone curve. This is because the ultrasound propagation speed inside the bone is higher than the speed in water. The ultrasonic plane wave propagates to the receiver faster when the bone media is included in the computational domain.

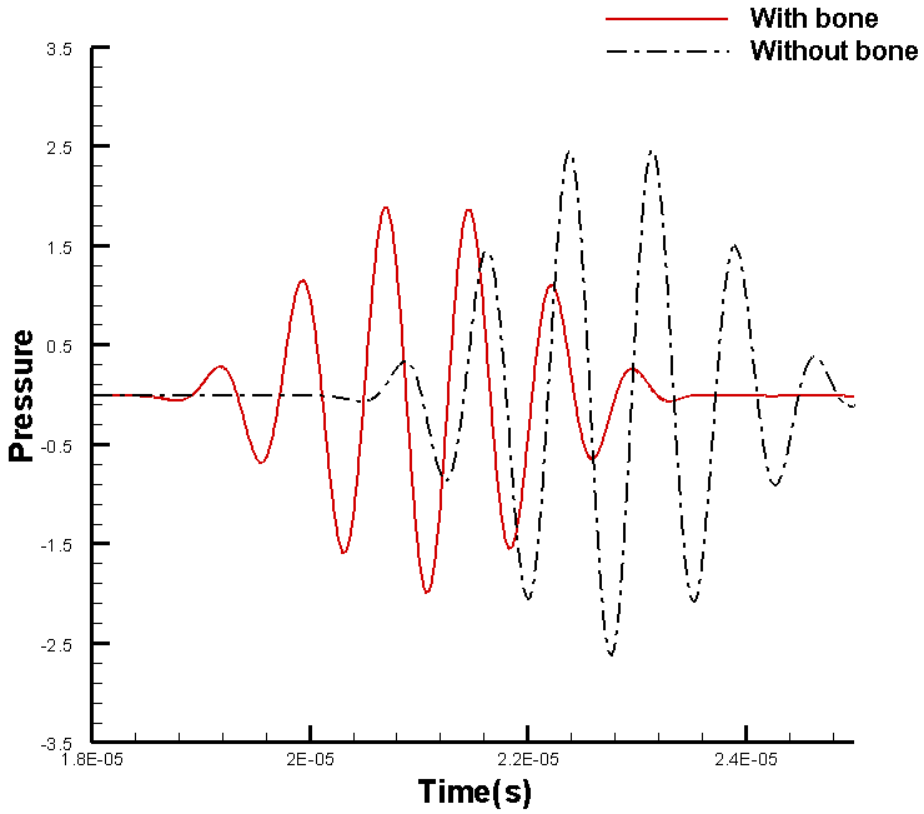

Fig. 4.4 Numerical pressure versus time of ultrasound propagation simulation.

To test if the perfectly-matched-layer in Ref. [83]-[85] can be applied for ultrasonic wave, two simulations are implemented. The governing equations for ultrasonic wave propagation in PML boundary is given as:

$$\frac{\partial v}{\partial t} = -\frac{1}{\rho_0}\left(\frac{\partial p}{\partial y} + \xi\frac{\partial q_p}{\partial y} + \xi v\right) \tag{4.12}$$

$$\frac{\partial w}{\partial t} = -\left[\frac{1}{\rho_0}\frac{\partial p}{\partial z} + \frac{1}{\rho_0}\left(\frac{1}{\beta} - 1\right)\frac{\partial q_p}{\partial z} + \xi w\right] \tag{4.13}$$

$$\frac{\partial p}{\partial t} = -\left[\rho_0 c_0^2\left(\frac{\partial v}{\partial y} + \frac{\partial w}{\partial z}\right) + \xi\left(\rho_0 c_0^2\frac{\partial q_v}{\partial y} + p\right) + \rho_0 c_0^2\left(\frac{1}{\beta} - 1\right)\frac{\partial w}{\partial z}\right] \tag{4.14}$$

where $\xi = 100\left(\frac{z - z_{\max}}{D}\right)^2$ and $\beta = 1 + 25\left(\frac{z - z_{\max}}{D}\right)^2$. D is the PML boundary layer thickness.

(a)

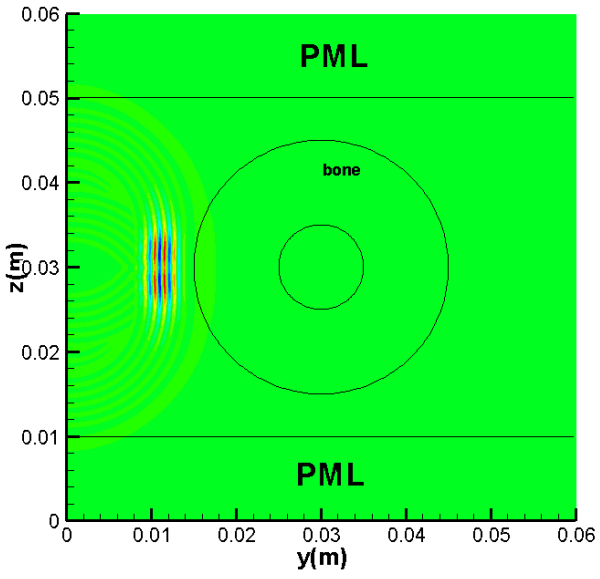

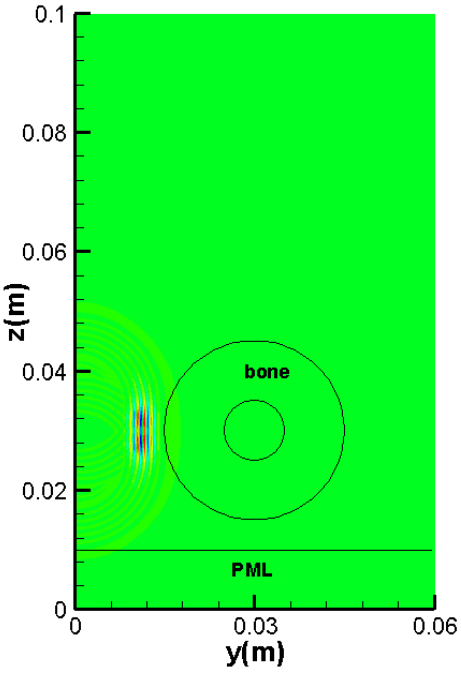

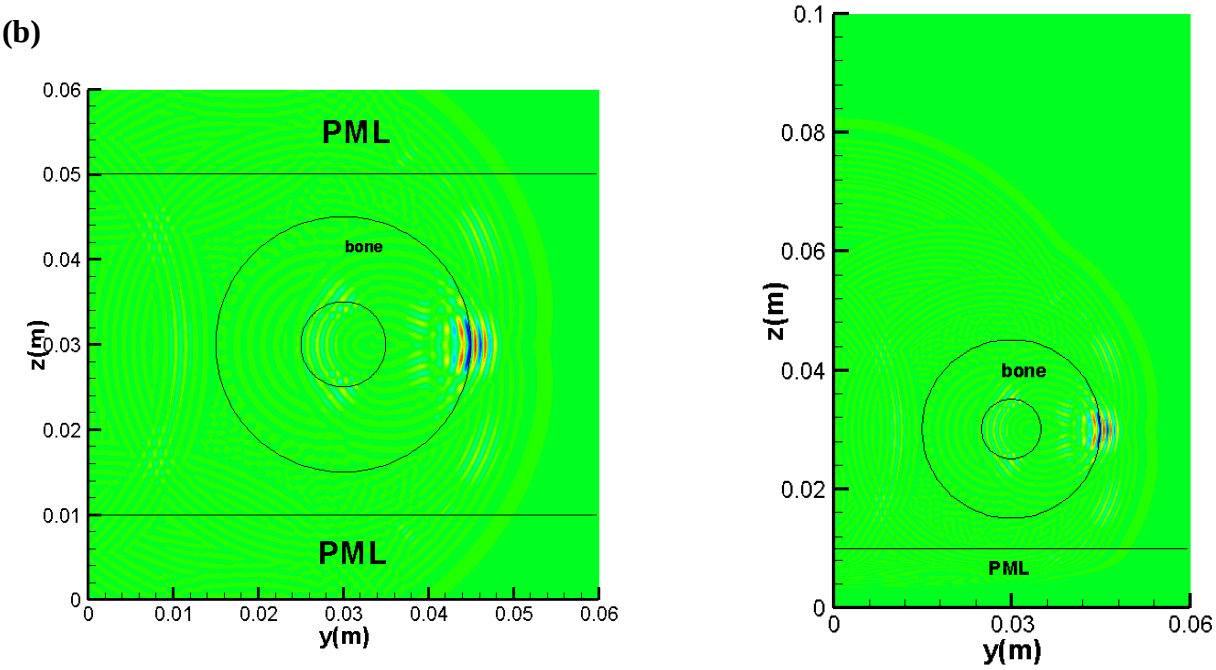

Fig. 4.5 Pressure contours of ultrasound propagation with PML boundary (a) $t = 10\mu s$ (b) $t = 30\mu s$.

One simulation is adding two PML boundaries at both top and bottom of the domain that shown in Fig. 4.1. The other is adding the PML boundary only at the bottom of the domain, but enlarge the domain size in z-direction to 0.1m. Thickness of PML boundary is 0.01m and all the other simulation parameters are kept the same as the previous simulations. The receiver is put at (0.005, 0.049) for both simulations which is near the top PML boundary. The pressure contours of these two different cases are shown in Fig. 4.5, and the numerical pressure of two simulations are given in Fig. 4.6. Based on the comparison in Fig. 4.6 we can see that the two numerical curves match very well, which means there are no reflections back from the PML boundary, and the wave propagation is just like in the free field. As a result it is known that the PML boundary works well for ultrasonic wave.

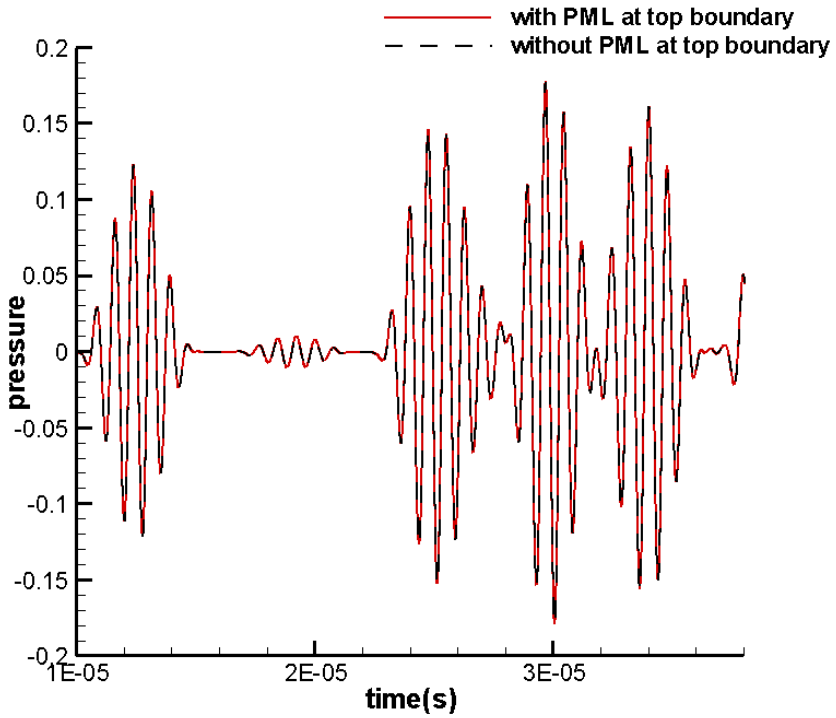

Fig. 4.6 Numerical pressure versus time of ultrasound propagation simulation with PML

To observe the interactions between several ultrasonic plane waves, another simulation is conducted. The ultrasound is set at the four boundaries of the domain, instead of only coming from the left side. Meanwhile all the other initial conditions and parameters are kept the same as the one wave simulations. Fig. 4.7 gives the pressure contours of the four ultrasonic plane wave simulations with bone media. Based on the pressure distributions we can clearly see that the ultrasound comes from the four directions, meet each other near the center of the domain, and how they are interacted. A lot of small reflections and dispersions can be observed all over the biological tissue.

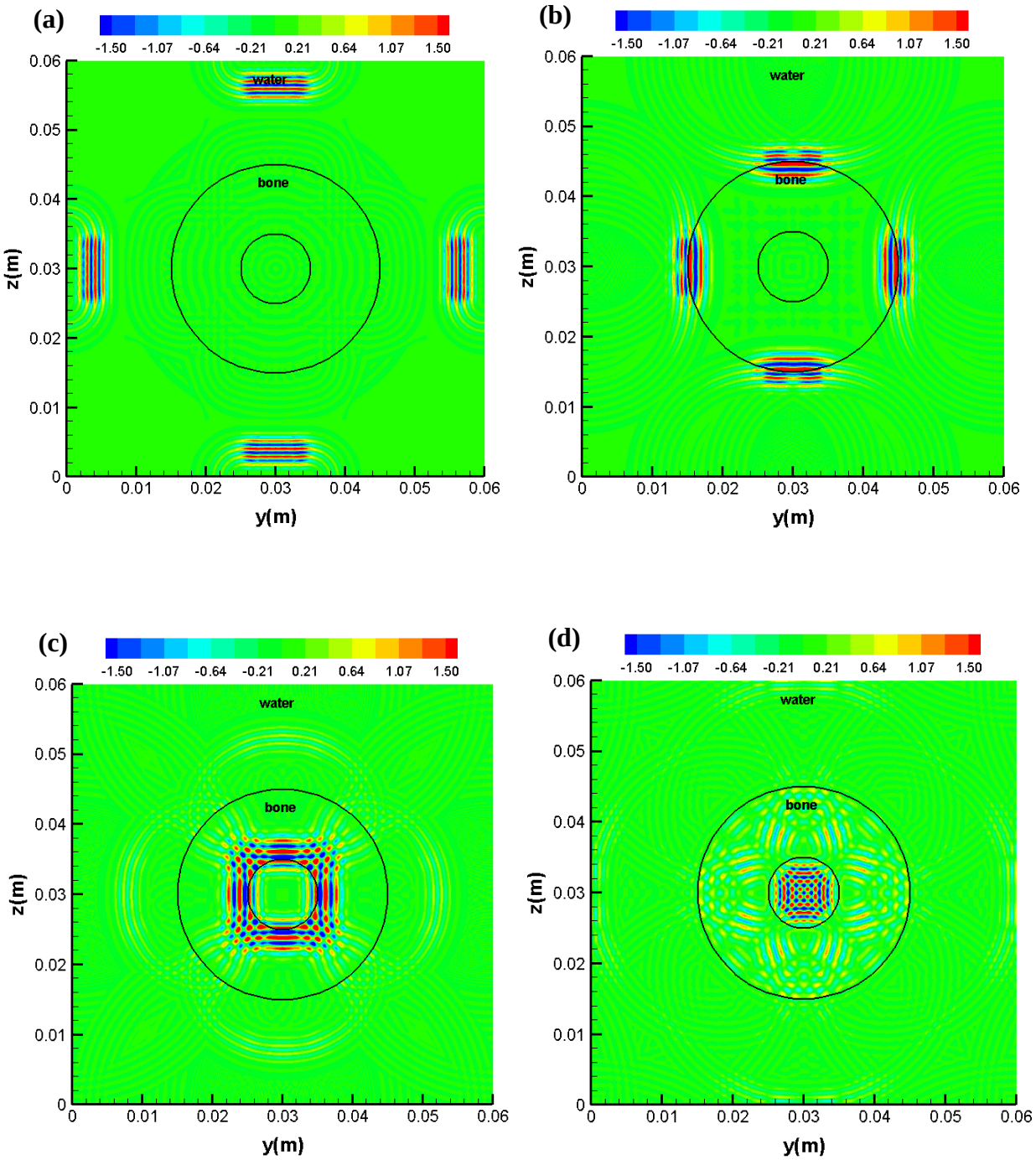
(a)
-1.50 -1.07 -0.64 -0.21 0.21 0.64 1.07 1.50
water
bone
z(m)
y(m)
0 0.01 0.02 0.03 0.04 0.05 0.06
(b)
-1.50 -1.07 -0.64 -0.21 0.21 0.64 1.07 1.50
water
bone
z(m)
y(m)
0 0.01 0.02 0.03 0.04 0.05 0.06
(c)
-1.50 -1.07 -0.64 -0.21 0.21 0.64 1.07 1.50
water
bone
z(m)
y(m)
0 0.01 0.02 0.03 0.04 0.05 0.06
(d)
-1.50 -1.07 -0.64 -0.21 0.21 0.64 1.07 1.50
water
bone
z(m)
y(m)
0 0.01 0.02 0.03 0.04 0.05 0.06

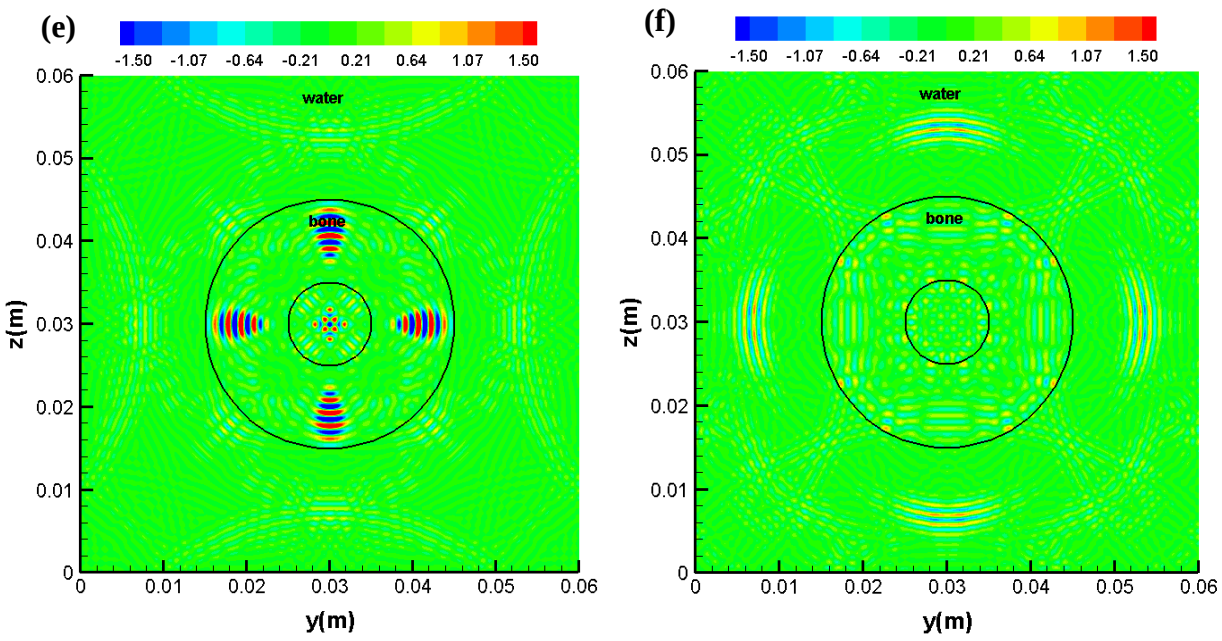

Fig. 4.7 Pressure contours of four ultrasonic wave propagations with bone at different moments (a) $t = 5\mu s$ (b) $t = 12.5\mu s$ (c) $t = 17.5\mu s$ (d) $t = 22.5\mu s$ (e) $t = 27.5\mu s$ (f) $t = 35\mu s$.

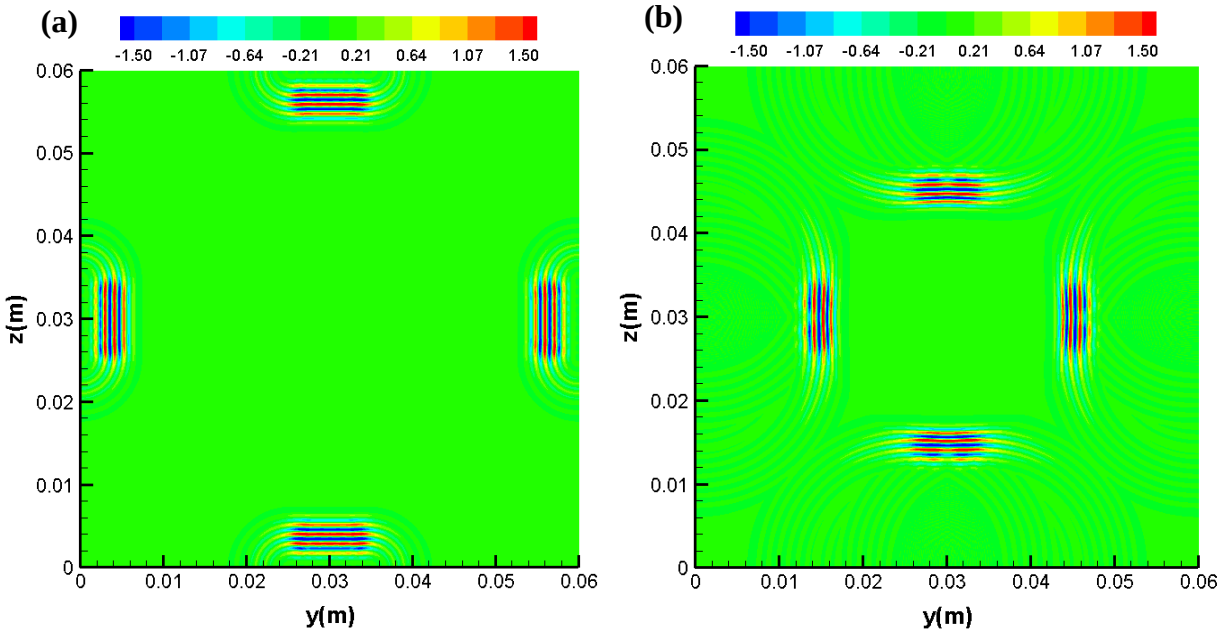

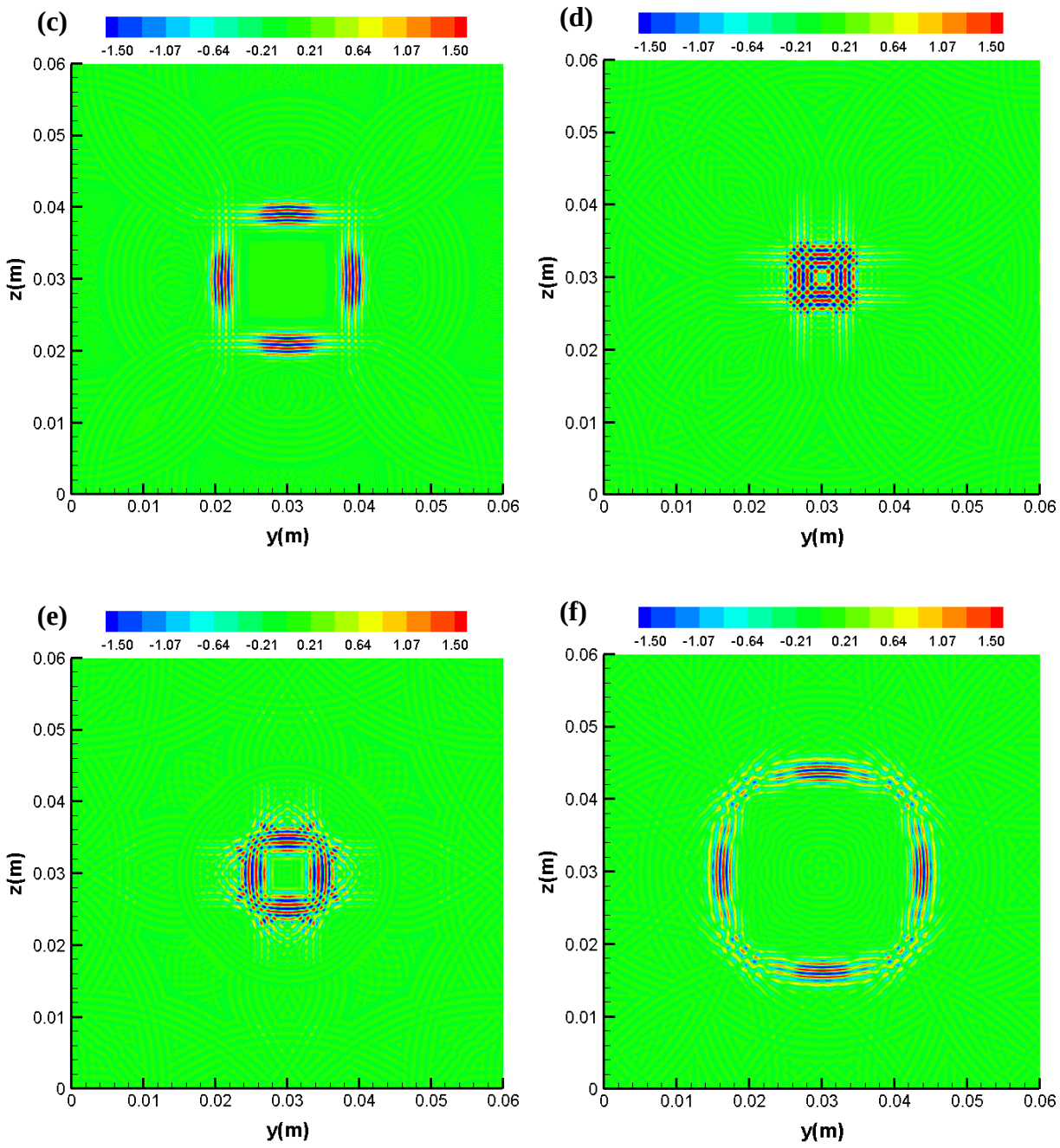

Fig. 4.8 Pressure contours of four ultrasonic wave propagations without bone at different moments(a) $t = 5\mu s$ (b) $t = 12.5\mu s$ (c) $t = 17.5\mu s$ (d) $t = 22.5\mu s$ (e) $t = 27.5\mu s$ (f) $t = 35\mu s$.

When the computational domain only contains water and there are no power law attenuations for the ultrasonic wave, the corresponding pressure contours are shown in Fig. 4.8. Different from the pressure distributions in Fig. 4.7, the four ultrasonic waves meet each other at the center of the domain and pass by. There are no reflections spread in the domain. Meanwhile the shapes and the magnitudes of four ultrasonic waves are not greatly influenced.

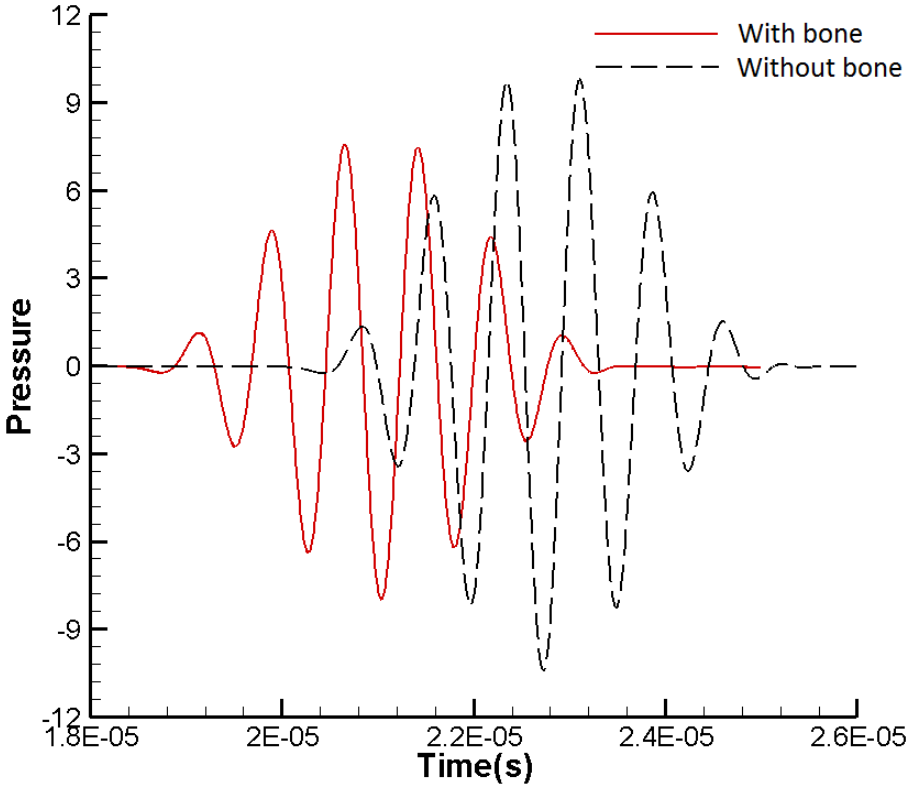

Fig. 4.9 Numerical pressure versus time of four ultrasonic wave propagations.

4.3 Ultrasound Propagation with Sonic Crystals

The sound blockage effect of sonic crystals has been studied for both point sound source and low frequency plane wave in chapter 2. In this section the ultrasonic plane wave propagation through cylinder arrays are simulated and the sound attenuating effect for ultrasound are studied.

The geometry for the ultrasonic wave propagation through cylinder arrays simulations are shown in Fig. 4.1. The computational domain size is $0.35\text{m} \times 0.06\text{m}$, and the other simulation parameters like grid size, time step, media density, propagation speed and fractional Laplacian power law exponent are the same as the ultrasonic plane wave propagation through biological tissue simulations in section 2 except the time domain is increased to 0.19ms. The same ultrasonic plane wave in section 2 is set at the left boundary of the domain from $z = 0.025\text{m}$ to $z = 0.35\text{m}$.

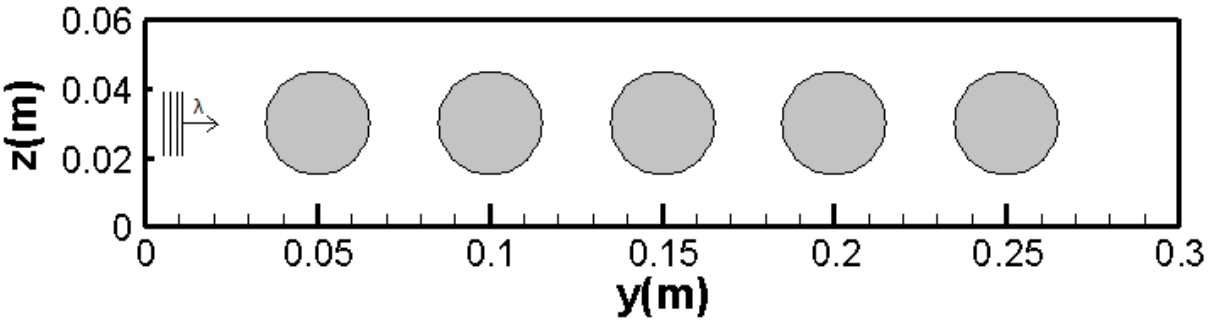

Fig. 4.10 Description of the geometry and coordinate system for the ultrasound wave propagation through sonic crystals propagations.

The sonic crystal for ultrasound propagation is consisted of five solid bone media that evenly placed along the wave propagation direction. The coordinates of the centers of five cylinders are (0.05, 0.03), (0.1, 0.03), (0.15, 0.03), (0.2, 0.03) and (0.25, 0.03), and the radius is 0.015m. Five receivers are placed after each cylinder, and the corresponding coordinates are (0.075, 0.03), (0.125, 0.03), (0.175, 0.03), (0.225, 0.03) and (0.275, 0.03).

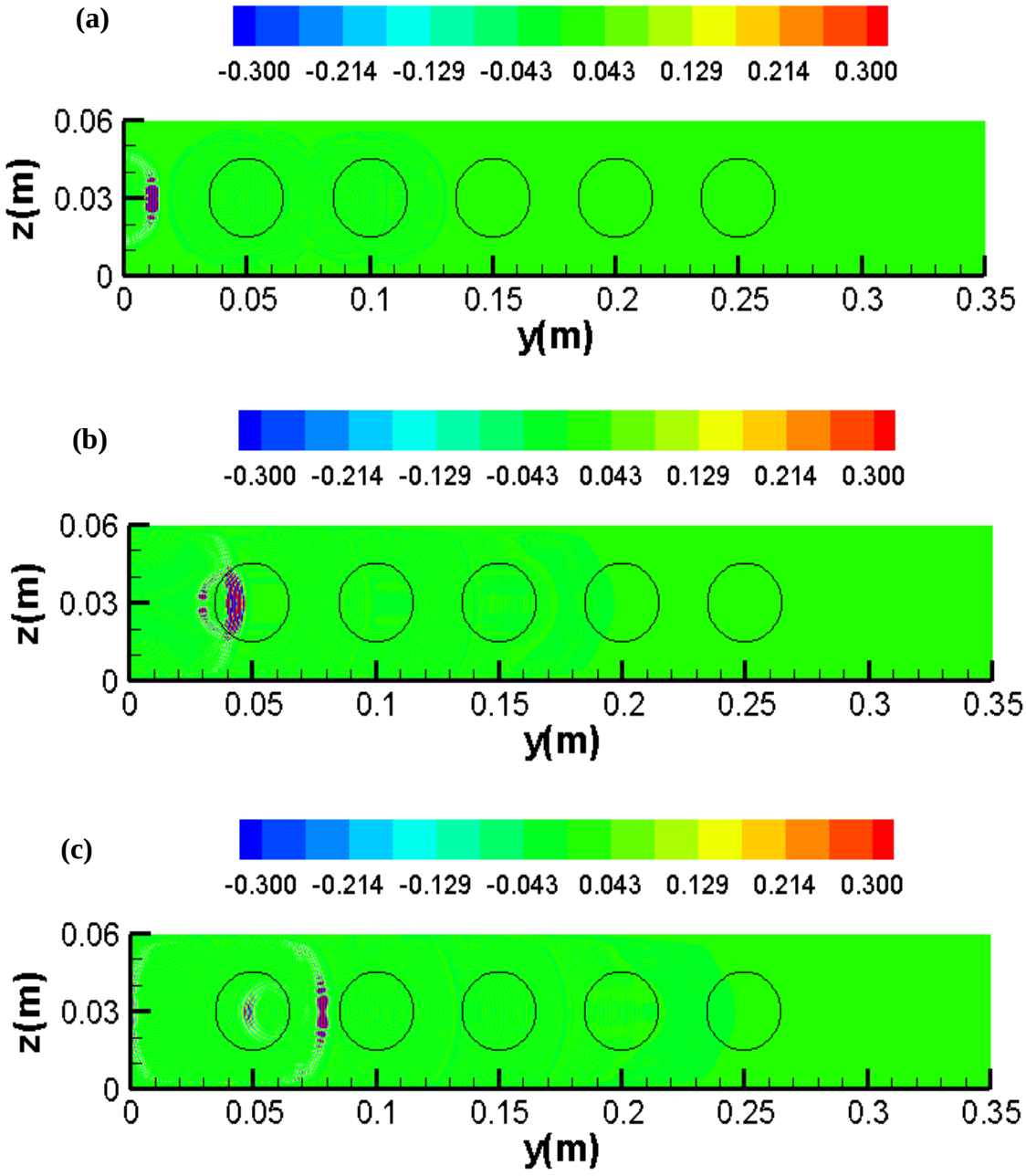

(d)

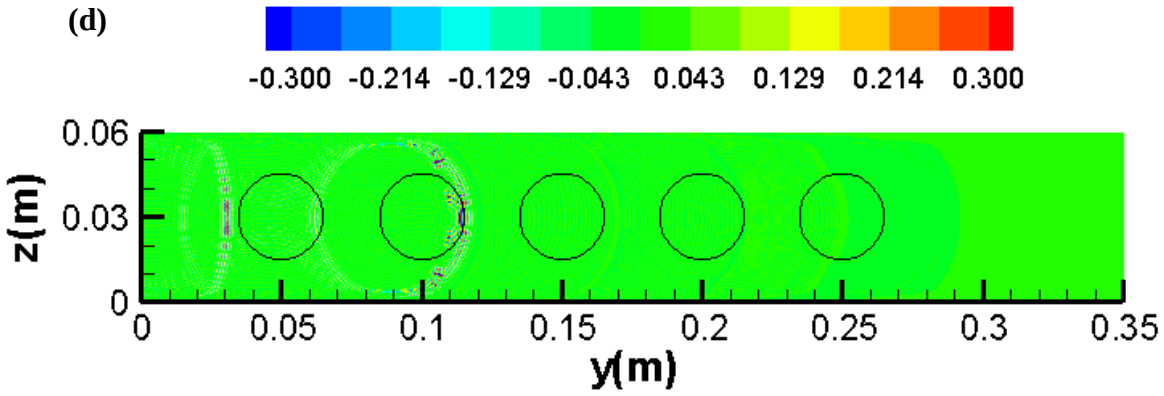
-0.300 -0.214 -0.129 -0.043 0.043 0.129 0.214 0.300
0.06
0.03
0
z(m)
0 0.05 0.1 0.15 0.2 0.25 0.3 0.35
y(m)

(e)

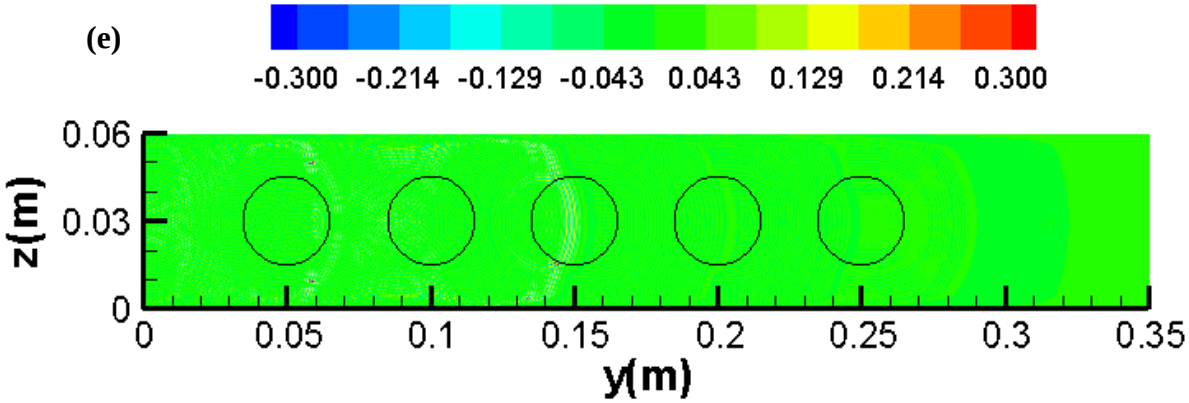
-0.300 -0.214 -0.129 -0.043 0.043 0.129 0.214 0.300
0.06
0.03
0
z(m)
0 0.05 0.1 0.15 0.2 0.25 0.3 0.35
y(m)

(f)

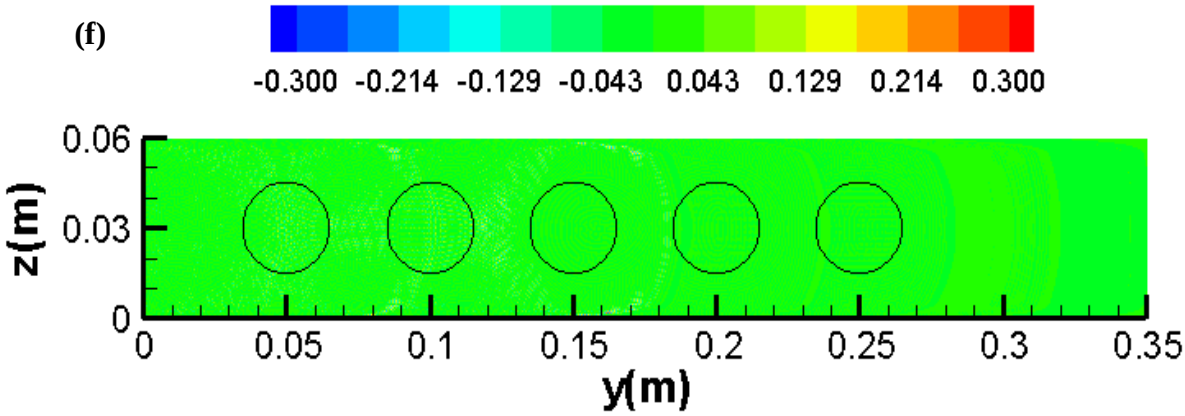
-0.300 -0.214 -0.129 -0.043 0.043 0.129 0.214 0.300
0.06
0.03
0
z(m)
0 0.05 0.1 0.15 0.2 0.25 0.3 0.35
y(m)

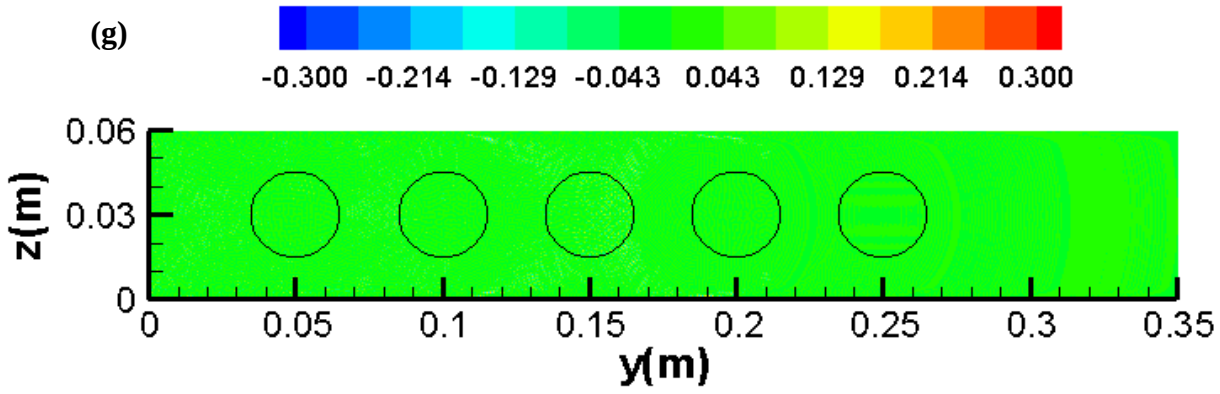

Fig. 4.11 Pressure contours of ultrasound propagation through cylinder arrays at different moment (a) t=0.01ms (b) t=0.03ms (c) t=0.05ms (d) t=0.07ms (e) t=0.9ms (f) t=0.11ms (g) t=0.13ms.

Fig. 4.11 gives the pressure contours of the ultrasound propagation through sonic crystals at different moment. We can see how the ultrasonic wave is greatly absorbed and attenuated by the bone sonic crystals. From Fig. 4.11 (f) we notice that after passing through the fourth sonic crystal, the ultrasonic wave is already extremely weak compared to the incident wave. It even can barely be observed from the pressure contour.

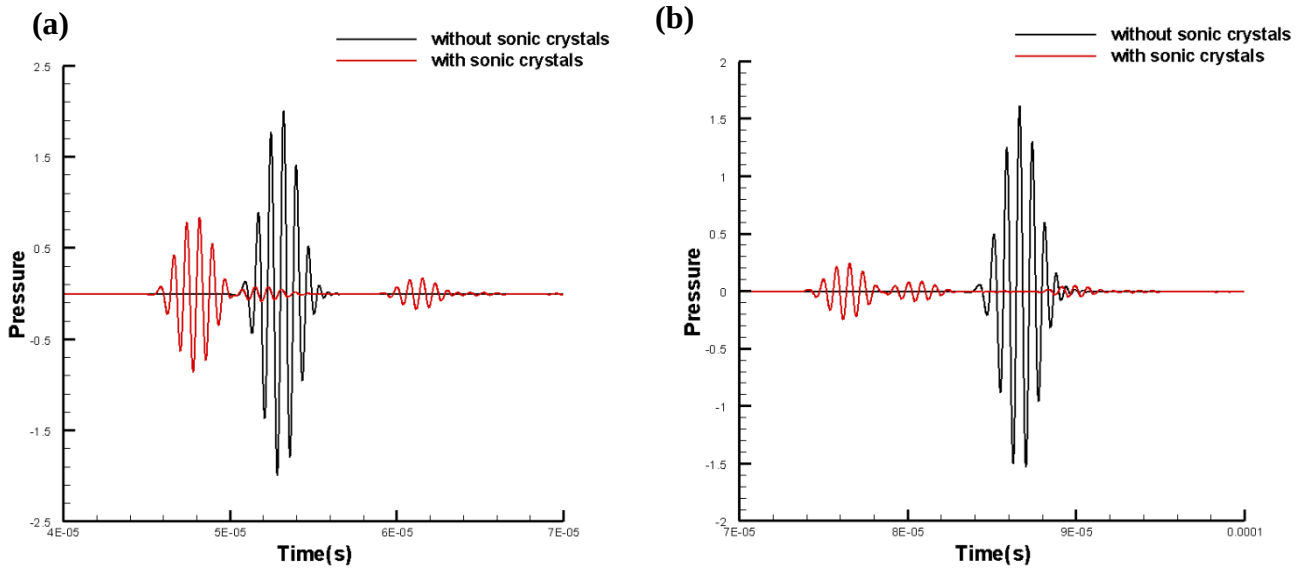

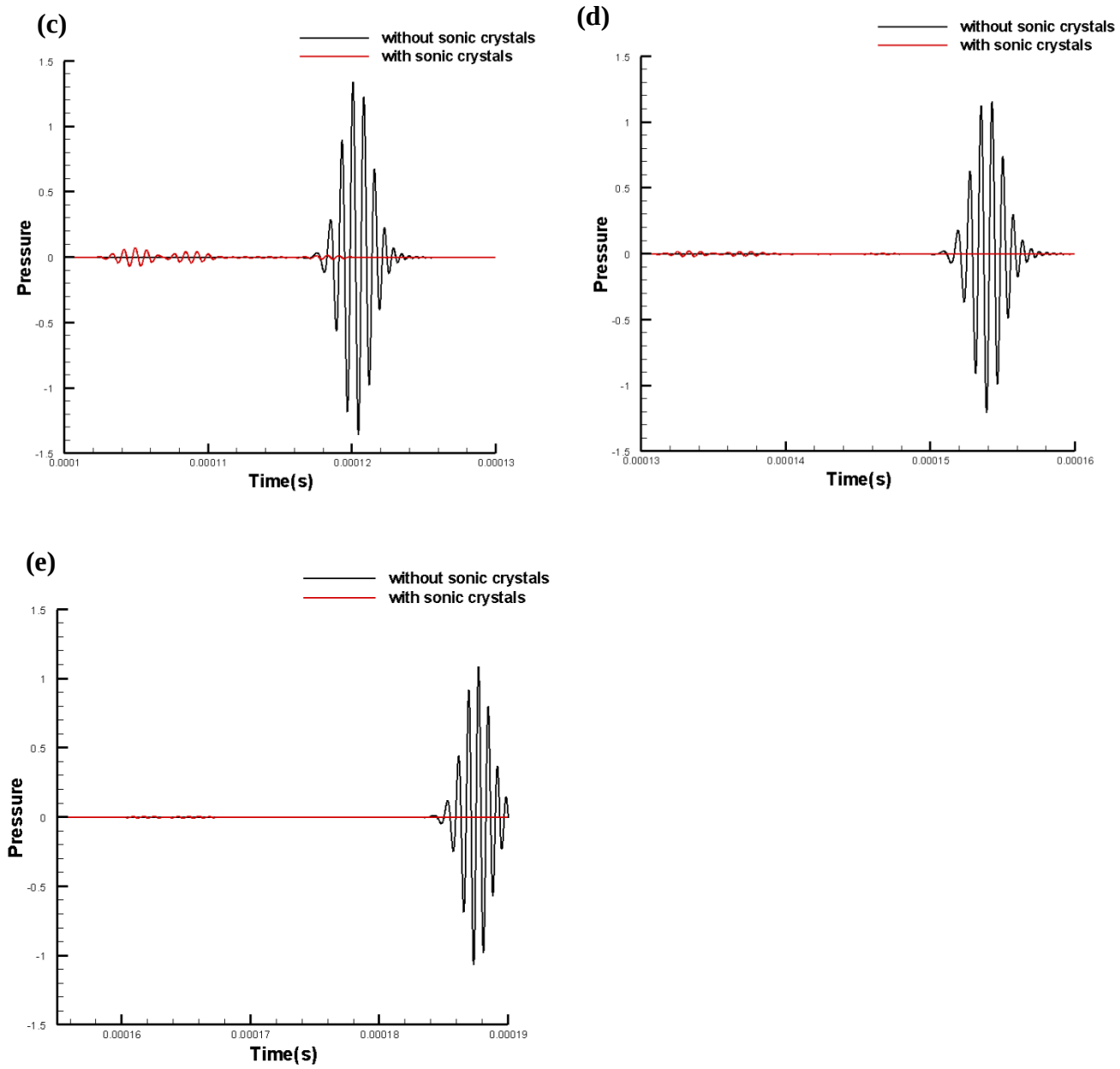

Fig. 4.12 Numerical pressure versus time for each receiver (a) (0.075, 0.03) (b) (0.125, 0.03) (c) (0.175, 0.03) (d) (0.225, 0.03) (e) (0.275, 0.03).

The numerical pressure of each receiver is shown in Fig. 4.12, and the values simulated without sonic crystals are also represented in the figure for comparison. It is seen that when the sonic crystals are applied, the ultrasonic plane wave pressure decreases drastically after passing through each bone. When there are no sonic crystals, the pressure of sonic plane wave is gradually decreasing while propagating, but the magnitude are many times larger than the pressure with sonic crystals. The corresponding sound attenuation levels are given in Fig. 4.13.

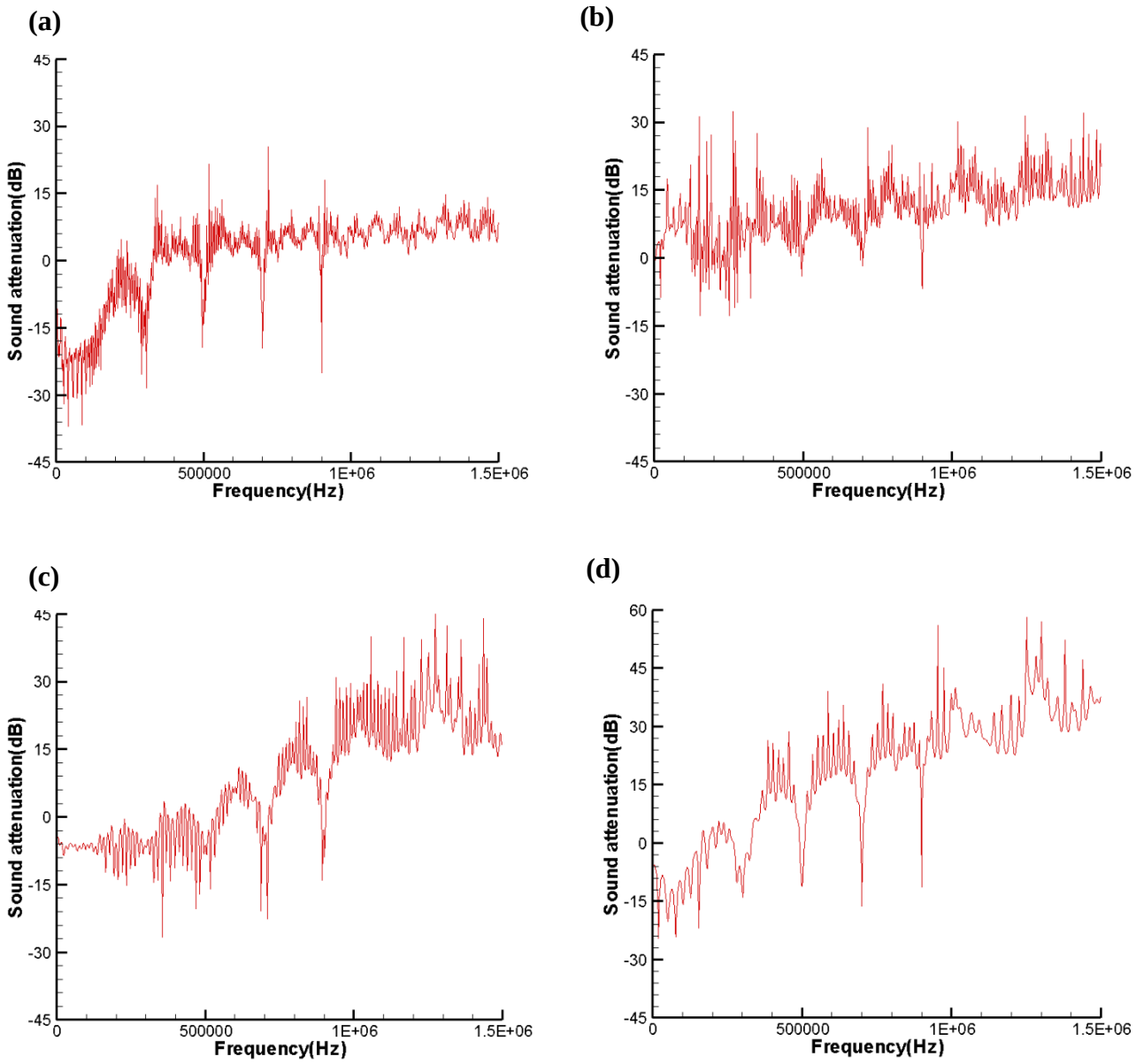

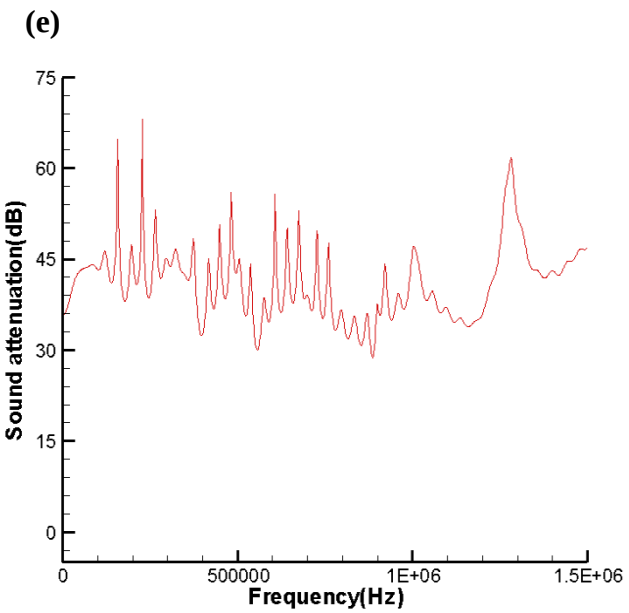

Fig. 4.13 Sound attenuations versus frequency for each receiver (a) (0.075, 0.03) (b) (0.125, 0.03) (c) (0.175, 0.03) (d) (0.225, 0.03) (e) (0.275, 0.03)

4.4 Summary

In this chapter, the ultrasonic plane wave propagation in biological tissue is studied. The theoretical governing equations and the numerical fractional Laplacian derivative approach are described. First of all, the simulation for single ultrasonic plane wave is implemented, the pressure of ultrasound is apparently attenuated after propagating through bone material, where the fractional Laplacian derivative is applied. After that, the absorption effect of PML boundary in Ref. [83]-[85] for ultrasound is studied. The numerical result shows that the PML boundary is also capable of attenuating and bending ultrasonic waves. Four ultrasonic plane waves come from four different directions are simulated. The interactions between ultrasonic waves can be observed based on corresponding pressure contours, the numerical absolute pressure is also given.

In the end the sonic crystals blockage effect for ultrasonic waves is studied. The sonic crystals are consisted of five bone material, which the fractional Laplacian derivative is applied. Due to the remarkable absorption and dispersion effect of sonic crystals, the pressure of ultrasonic waves are greatly decreased. As the result the sound attenuation values for each receiver are high.

5 Conclusion

5.1 Conclusions

The primary focus of this thesis is investigating the sound wave propagation under complex environments. Various factors for acoustics, such as sonic crystals, ground surface and ambient vortical flow are considered. This study is implemented by a numerical model for linearized Euler equations combining the FDTD method with the immersed boundary method. The numerical results are compared with the analytical solutions or experimental data, when applicable.

The sound wave perpendicularly propagating through cylinder arrays is studied for both two- and three-dimensional cases. In 2D studies, when the number of cylinders in the vertical direction is fixed, the use of more cylinders in the wave propagation direction results in a better sound blockage effect. This conclusion is not necessarily valid when the receiver is close to the arrays because the sound pressure level is enhanced instead of attenuated due to the reflections. The validity of the numerical model is confirmed by the good agreement with the theoretical Bragg band gap value. An Euler-type moving zonal-domain approach is applied for three-dimensional simulations. The moving domain size is an important factor for numerical simulation. The size needs to be small enough to achieve high calculation efficiency and large enough to maintain the dispersing pulse and energy. The accuracy of the moving-domain method has been verified by comparing its simulated results with the results of non-moving domain method. Additional simulation studies for sonic crystals are performed based on the published measurement. The two band gaps of the simulated results have a very good agreement with the experimental data, again showing the accuracy of the simulation model. By using different sonic crystal materials, the results suggest that selecting appropriate materials is an important factor to block different sound

source frequency. The sonic crystals made of porous materials with intermediate flow resistivity are more effective for noise blockage.

Sound plane wave propagation through a vortex pair is investigated. The FDTD linearized Euler equations are solved with a fifth order WENO scheme. Frist, the sound propagation over a stationary vortex pair is considered for different Mach numbers and vortex pair orientation angles ψ. The pressure distributions and normalized pressure levels clearly show the significant sound scattering effect of the vortical flow. The maximum sound scattering effect is obtained at $\psi = 270^0$ and the minimum values are at $\psi = 0^0$ and $\psi = 180^0$. Furthermore, the scattering effect of a moving vortex pair is studied with different Mach numbers under angle $\psi = 90°$. The accuracy of the numerical model has also been verified by comparing with the analytical solutions.

The ultrasonic plane wave propagation in biological tissue is studied. The linearized Euler acoustic equations coupled with spatial-fractional Laplacian operators are presented. From our numerical analysis, it is seen that the ultrasonic wave is significantly absorbed and attenuated after propagating through the bone material, where the fractional Laplacian derivative is applied. After that, the absorption effect of the Perfectly-Matched-Layer (PML) boundary for ultrasonic wave is investigated. The numerical results suggest that the PML boundary is also capable of absorbing ultrasound. The simulation with four ultrasonic plane waves that came from four different directions is implemented for studying the interactions between ultrasonic waves. In the end, the sonic crystals' sound blockage effect for ultrasonic waves is investigated. The sonic crystals are made up of five bone materials, where the fractional Laplacian derivative is applied. Due to the remarkable absorption and dispersion effects, the pressure of ultrasonic plane waves drastically decreases. As a result the sound attenuation values for each receiver are high.

5.2 Future Works

Besides the current advances presented in this thesis, there are still many other possible improvements for the future works. First, most of the analytical solutions are limited to homogeneous propagation conditions in which the environmental properties do not change much. The development of analytical solutions for inhomogeneous atmosphere and complex terrain can help verify and improve the accuracy of the numerical simulations.

Secondly, for the three-dimensional long distance sound wave propagation simulations, one must note that the required computer memory is prohibitively high and the cost is expensive. The development of supercomputer power and parallel computing techniques would help to speed up the calculation and greatly reduce the cost.

Appendix A: Error Analysis for Numerical Scheme

In our simulations, we use second-order central difference for space and time. When calculate the values of the nodes that near the boundary of two different media, a numerical error is generated because the central difference scheme. To discuss the numerical error, we consider the one-dimensional scheme in y-direction with no background shear flow: $V_{av}=0$. Then the governing equations and the corresponding discretized equations for propagation in air are:

$$\frac{\partial v}{\partial t}=-\alpha_{av}\frac{\partial p}{\partial y} \tag{A.1}$$

$$\frac{\partial p}{\partial t}=-\gamma p_{av}\frac{\partial v}{\partial y} \tag{A.2}$$

$$v_j^{n+1}-v_j^n=-\alpha_{av}\frac{\Delta t}{\Delta y}\left(p_j^{n+1}-p_{j-1}^{n+1}\right) \tag{A.3}$$

$$p_j^{n+1}-p_j^n=-\gamma p_{av}\frac{\Delta t}{\Delta y}\left(v_{j+1}^n-v_j^n\right) \tag{A.4}$$

Combining equation (A.3) and (A.4) we have the scheme for air:

$$v_j^{n+1}=2v_j^n-v_j^{n-1}+c^2\left(\frac{\Delta t}{\Delta y}\right)^2\left(v_{j+1}^n-2v_j^n+v_{j-1}^n\right) \tag{A.5}$$

The governing equations and discretized equations in porous media:

$$\frac{\partial v}{\partial t}=-\frac{\Omega}{c_s}\alpha_{av}\left(\frac{\partial p}{\partial y}+\sigma v\right) \tag{A.6}$$

$$\frac{\partial p}{\partial t}=-\frac{\gamma p_{av}}{\Omega}\frac{\partial v}{\partial y} \tag{A.7}$$

$$v_j^{n+1}-v_j^n=-\frac{\Omega}{c_s}\alpha_{av}\frac{\Delta t}{\Delta y}\left(p_j^{n+1}-p_{j-1}^{n+1}+\Delta y\sigma v_j^n\right) \tag{A.8}$$

$$p_j^{n+1}-p_j^n=-\frac{\gamma p_{av}}{\Omega}\frac{\Delta t}{\Delta y}\left(v_{j+1}^n-v_j^n\right) \tag{A.9}$$

For rigid barriers, the resistivity of porous medium is selected as an extremely high value, to make the matrix diagonal dominant, we change the velocity equation Eq. (A.8) to semi-explicit scheme:

$$v_j^{n+1} - v_j^n = -\frac{\Omega}{c_s}\alpha_{av}\frac{\Delta t}{\Delta y}\left(p_j^{n+1} - p_{j-1}^{n+1} + \Delta y \sigma v_j^{n+1}\right) \tag{A.10}$$

Combining Eq. (A.9) and Eq. (A.10) we have:

$$(1+\beta)v_j^{n+1} - 2v_j^n + v_j^{n-1} = {c_p}^2\left(\frac{\Delta t}{\Delta y}\right)^2\left(v_{j+1}^n - 2v_j^n + v_{j-1}^n\right) + \beta v_j^n \tag{A.11}$$

where $\beta = \frac{\Omega c^2 \sigma \Delta t}{\gamma p_{av} c_s}$. Thus we get the numerical scheme for high resistivity porous media:

$$v_j^{n+1} = \frac{2}{1+\beta}v_j^n - \frac{1}{1+\beta}v_j^{n-1} + \frac{1}{1+\beta}{c_p}^2\left(\frac{\Delta t}{\Delta y}\right)^2\left(v_{j+1}^n - 2v_j^n + v_{j-1}^n\right) + \frac{\beta}{1+\beta}v_j^n \tag{A.12}$$

Now we discuss the situation that the sound wave propagates into porous media from air domain. The graphic illustration of the grid is given in Fig. A.1.

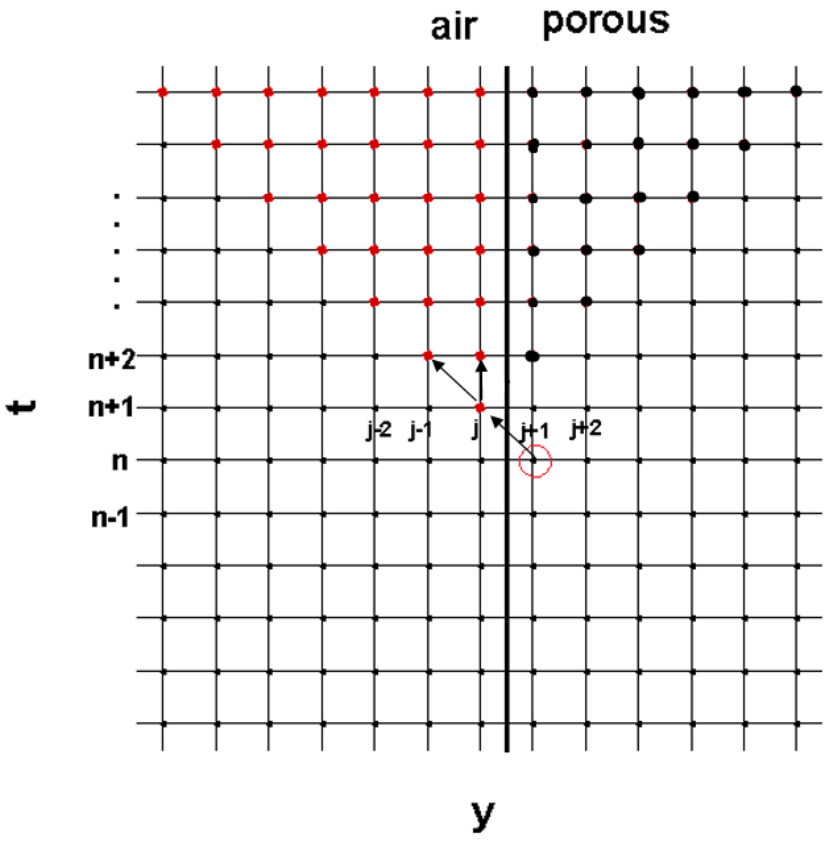

Fig. A.1 Grid illustration for numerical error near the boundary.

In Fig. A.1, *y*-axis is the wave propagation direction, and *t*-axis stands for the time marching. We can find that at moment $n+1$ the 1D sound wave propagates to location $y= j$ where is right before the interface of air and porous medium. To calculate the values for the node $y= j$, we need to use the velocity v_{j+1}^{n} at point $j+1$, which is inside the porous media. However in our numerical scheme we consider the point $j+1$ is still in air domain. To discuss the caused numerical error, we use the pressure equation (A.9) of porous media first and then use velocity equation (A.3) of air. Combining those two equations we have the corrective scheme for point *j*:

$$v_j^{n+1}|_{a\to p} = 2v_j^n - v_j^{n-1} + \frac{c^2}{\Omega}\left(\frac{\Delta t}{\Delta y}\right)^2\left(v_{j+1}^n - 2v_j^n + v_{j-1}^n\right) \tag{A.13}$$

The subscript $a \to p$ means the wave propagates from air to porous. Then Equation (A.13) subtracts the current scheme (A.5) we have the error between those two schemes:

$$\delta v_j^{n+1} = \left|v_j^{n+1}|_{a\to p} - v_j^{n+1}\right| = \left|\left(\frac{1}{\Omega}-1\right)c^2\left(\frac{\Delta t}{\Delta y}\right)^2\left(v_{j+1}^n - 2v_j^n + v_{j-1}^n\right)\right| \tag{A.14}$$

Then we change the current scheme (A.5) and (A.12) to error format for air (A.15) and porous (A.16):

$$\delta v_j^{n+1} = 2\delta v_j^n - \delta v_j^{n-1} + a\left(\delta v_{j+1}^n - 2\delta v_j^n + \delta v_{j-1}^n\right) \tag{A.15}$$

$$\delta v_j^{n+1} = \frac{2}{1+\beta}\delta v_j^n - \frac{1}{1+\beta}\delta v_j^{n-1} + \frac{b}{1+\beta}\left(\delta v_{j+1}^n - 2\delta v_j^n + \delta v_{j-1}^n\right) + \frac{\beta}{1+\beta}\delta v_j^n \tag{A.16}$$

To simplify the following expressions, we notate the $a = c^2\left(\frac{\Delta t}{\Delta y}\right)^2$, $b = c_p{}^2\left(\frac{\Delta t}{\Delta y}\right)^2$. For most of the cases, the initial conditions are chosen as speed of sound $c = 340\text{m/s}$, time step $\Delta t = 2.5\times10^{-6}\text{s}$, grid size $\Delta y = 0.008\text{m}$, ambient pressure $p_{av} = 101000\text{Pa}$ and the resistivity $\sigma = 4\times10^8\,\text{Pa}$. Then we have $a = 0.011$, $b = 0.0038$, $\beta = 81.75$.

Now we notate the value $E = \delta v_j^{n+1}$ as the error between two schemes. And to simplify the analysis, we only keep the leading terms in equation (A.16):

$$\delta v_j^{n+1} \approx \delta v_j^n \tag{A.17}$$

By this assumption, the propagation of error is simplified to happen only in location $y = j$. And the error will not propagate into porous media, which coincides with the initial condition that the porous media is rigid. The numerical errors of each point at every following time step are calculated and are given in the tables below.

T=n+1					
	δv_y^{n-1}	δv_{y-1}^n	δv_y^n	δv_{y+1}^n	δv_y^{n+1}
$y=j$	0	0	0	0	E

T=n+2					
	δv_y^n	δv_{y-1}^{n+1}	δv_y^{n+1}	δv_{y+1}^{n+1}	δv_y^{n+2}
$y=j$-1	0	0	0	E	aE
$y=j$	0	0	E	0	$2E-2aE$

T=n+3					
	δv_y^{n+1}	δv_{y-1}^{n+2}	δv_y^{n+2}	δv_{y+1}^{n+2}	δv_y^{n+3}
$y=j$-2	0	0	0	aE	a^2E
$y=j$-1	0	0	aE	$2E-2aE$	$4aE-4a^2E$
$y=j$	E	aE	$2E-2aE$	0	$3E-8aE+5a^2E$

T=n+4					
	δv_y^{n+2}	δv_{y-1}^{n+3}	δv_y^{n+3}	δv_{y+1}^{n+3}	δv_y^{n+4}
$y=j$-3	0	0	0	a^2E	a^3E
$y=j$-2	0	0	a^2E	$4aE-4a^2E$	$6a^2E-6a^3E$
$y=j$-1	aE	a^2E	$4aE-4a^2E$	$3E-8aE+5a^2E$	$10aE-24a^2E$ $+14a^3E$
$y=j$	$2E-2aE$	$4aE-4a^2E$	$3E-8aE+5a^2E$	0	$4E-20aE+$ $30a^2E-14a^3E$

T=n+5					
	δv_y^{n+3}	δv_{y-1}^{n+4}	δv_y^{n+4}	δv_{y+1}^{n+4}	δv_y^{n+5}
$y=j$-4	0	0	0	a^3E	a^4E
$y=j$-3	0	0	a^3E	$6a^2E-6a^3E$	$8a^3E-8a^4E$
$y=j$-2	a^2E	a^3E	$6a^2E-6a^3E$	$10aE-24a^2E$ $+14a^3E$	$21a^2E-48a^3E$ $+25a^4E$
$y=j$-1	$4aE-4a^2E$	$6a^2E-6a^3E$	$10aE-24a^2E$ $+14a^3E$	$4E-20aE$ $+30a^2E-14a^3E$	$20aE-84a^2E$ $+112a^3E-48a^4E$
$y=j$	$3E-8aE$ $+5a^2E$	$10aE-24a^2E$ $+14a^3E$	$4E-20aE$ $+30a^2E$ $-14a^3E$	0	$5E-40aE+115a^2E$ $-112a^3E+42a^4E$

……

Based on the results above, we can conclude the errors of each point at every time step, and the values are listed in the table below. We can find that the error will propagate to the red points that marked in Fig. A.1 until all the nodes in air domain. However since the coefficients *a* and *b* are very small values, and the coefficients before the error *E* are reduced exponentially. As a result, the numerical errors far away from the boundary are negligible, and we can find that our numerical results given in Fig. 1.3 have an excellent agreement with the data in the literature.

T	n+1	n+2	n+3	n+4	n+5	…
…						
y=j-4	0	0	0	0	a^4E	
y=j-3	0	0	0	a^3E	$8a^3E-8a^4E$	
y=j-2	0	0	a^2E	$6a^2E-6a^3E$	$21a^2E-48a^3E$ $+25a^4E$	
y=j-1	0	aE	$4aE-4a^2E$	$10aE-24a^2E$ $+14a^3E$	$20aE-84a^2E$ $+112a^3E$ $-48a^4E$	
y=j	E	$2E$ $-2aE$	$3E$ $-8aE$ $+5a^2E$	$4E-20aE$ $+30a^2E$ $-14a^3E$	$5E-40aE$ $+115a^2E$ $-112a^3E$ $+42a^4E$	

References

[1] Cowan, J. P., Handbook of Environmental Acoustics, John Wiley and Sons, Chichester, UK, 1993.

[2] Cox, T. J., D'Antonio, P., Acoustic Absorbers and Diffusers: Theory, Design and Application, Spon, London, UK, 2004.

[3] Attenborough, K., Li, K. M., Horoshenkov, K., Predicting Outdoor Sound, Taylor and Francis, New York, 2006.

[4] Bucur, V., Urban Forest Acoustics, Springer, Berlin, Germany, 2006.

[5] Moser, M., Zimmermann, S., Ellis, R., Engineering Acoustics: An Introduction to Noise Control, Springer, New York, 2009.

[6] J. E. Piercy, T. F.W. Embleton, and L.C.Sutherland, "Preview of noise propagation in the atmosphere," J. Acoust. Soc. Am. 61(6), 1403-1418 (1977)

[7] P. H. Parkin and W. E. Scholes. "The horizontal propagation of sound from a jet noise close to the ground at Hatfield," J. Sound Vib. 2, 353-374 (1965).

[8] Szabo, T. L., Diagnostic Ultrasound Imaging, Elsevier, New York, 2004.

[9] Ter Haar, G., Coussios, C., "High intensity focused ultrasound: ultrasound: Physical principles and devices," International Journal of Hyperthermia, Vol. 23, 2007, pp. 89-104.

[10] Cox, B. T., Treeby, B. E., "Artifact trapping during time reversal photo acoustic imaging for acoustically heterogeneous media," IEEE Transactions on Medical Imaging, Vol. 29, 2010, pp. 387-396.

[11] Laufer, J., Cox, B., Zhang, E., Beard, P., "Quantitative determination of chromophore concentrations from 2D photo acoustic images using a nonlinear model-based inversion scheme," Applied optics, Vol. 49, 2010, pp. 1219-1233.

[12] Treeby, B. E., Cox, B. T., “Modeling power law absorption and dispersion for acoustic propagation using the fractional Laplacian,” Journal of the Acoustical Society of America, Vol. 127, 2010, pp. 2741-2748.

[13] Treeby, B. E., Jaros, J., Rendell, A. P., Cox, B. T., “Modeling nonlinear ultrasound propagation in heterogeneous media with power law absorption using a k-space pseudo spectral method,” Journal of the Acoustical Society of America, Vol. 131, 2012, pp. 4324-4336.

[14] Rosenschein, U., Frimerman, A., Laniado, S., Miller, H. I., “Study of the mechanism of ultrasound angioplasty from human thrombi and bovine aorta,” American Journal of Cardiology, Vol. 74, 1994, pp. 1263-1266.

[15] Rosenschein, U., Furman, V., Kerner, E., Fabian, I., Bernheim, J., Eshel, Y., “Ultrasound imaging-guided noninvasive ultrasound thrombolysis: preclinical results,” Circulation, Vol. 102, 2000, pp. 238-245.

[16] Maxwell, A. D., Cain, C. A., Duryea, A. P, Yuan, L., Gurm, H. S., Xu, Z., “Noninvasive thrombolysis using pulsed ultrasound cavitation therapy-histotripsy,” Ultrasound in Medicine and Biology, Vol. 35, 2009, pp. 1982-1984.

[17] Wright C, Hynynen K, Goertz, D., “In vitro and in vivo high intensity focused ultrasound thrombolysis,” Investigative Radiology, Vol. 47, 2012, pp. 217-225.

[18] Carstensen E. L., Bacon D. R. (2008). Biomedical Applications. In Hamilton, M. F., Blackstock, D.T. (eds.), Nonlinear Acoustics, Acoustical Society of America.

[19] Cobbold, R. S. (2007). Nonlinear Ultrasonics. In Foundations of Biomedical Ultrasound, Oxford University Press.

[20] Tao, H., “Propagation of sound in the vicinity of rigid porous interfaces,” Purdue University, (2013).

[21] Raspet, R., Lee, S. W., Kuester, E., Chang, D. C., Richards, W. F., Gilbert, R., Bong, N., “A fast-field program for sound propagation in a layered atmosphere above an impedance ground,” Journal of the Acoustical Society of America, Vol. 77, 1985, pp. 345-352.

[22] Lee, S. W., Bong, N., Richards, W. F., Raspet, R., “Impedance formulation of the fast field program for acoustic wave propagation in the atmosphere,” Journal of the Acoustical Society of America, Vol. 86, 1989, pp. 179-183.

[23] Nijs, L., Wapenaar, C. P. A., “The Influence of wind and temperature gradients on sound propagation, calculated with the two-way wave equation,” Journal of the Acoustical Society of America, Vol. 87, 1990, pp. 1987-1998.

[24] Wilson, D. K., “Sound field computations in a stratified, moving medium,” Journal of the Acoustical Society of America, Vol. 94, 1993, pp. 400-407.

[25] F. R. Dinapoli, “Fast field program,” J. Acoust. Soc. Am. 47, 100-100 (1970).

[26] F. R. Dinapoli and M. R. Powers, “Fast field program (FFP) and attenuation loss in hudson bay,” J. Acoust. Soc. Am. 51, 108-108 (1972).

[27] T. L. Richards and K. Attenborough, “Accurate FFT-based Hankel transform for predictions of outdoor sound propagation,” J. Sound Vib. 109(1). 157-167(1986).

[28] S. J. Franke and G. W. Swenson Jr, “A brief tutorial on the fast field program(FFP) as applied to sound propagation in the air,” J. Appl. Acoust, 27, 103-115 (1989).

[29] M. West, R. A. Sack and R. Walkden, “The Fast Field Program (FFP). A second tutorial: Application to long range sound propagation in the air,” J. Appl. Acoust. 33, 199-228 (1991).

[30] S. M. Candel, “Dual algorithms for fast calculation of the Fourier-Bessel transform,” I.E.E.E. Transactions on acoustics, speed and signal processing, ASSP- 29 (1981).

[31] F. R. Dinapoli and R. L. Deavenport, “Theoretical and numerical Green's function field solution in a phase multilayered medium,” J. Acoust. Soc. Am. 67, 92-105 (1980).

[32] S. Tooms, S. Taherzadeh and K. Attenborough, “Sound propagation in a refractive fluid above a layered fluid-saturated porous elastic material,” J. Acoust. Soc. Am. 93, 173-181 (1993).

[33] M. A. Letontovich and V. A. Fock, “Solution of the problem of propagation of electromagnetic waves along the earth's surface by the method of parabolic equation,” J. Exp. Theor. Phys. 16(7), 557 (1946).

[34] Di, X., Gilbert, K. E., “Wave propagation in a 3-D turbulent atmosphere: horizontal coherence,” Proc. Eighth Symposium on Long-Range Sound Propagation, The Pennsylvania State University, Pennsylvania, 1998, pp. 169-180.

[35] K. E. Gilbert and X. Di, “A fast Green's function method for one-way sound propagation in the atmosphere,” J. Acoust. Soc. Am. 94(4), 2343-2352 (1993).

[36] E. M. Salomons, “Improved Green's function parabolic equation method for atmospheric sound propagation,” J. Acoust. Soc. Am. 104(1), 100-111 (1998). 227.

[37] Dallois, L., Blanc-Benon, P., “Wide angle parabolic equations in moving media: sound diffraction by a core vortex,” AIAA paper, 2001, pp. 2001-2256.

[38] Gilbert, K. E., White, M. J., “Application of the parabolic equation to sound propagation in a refracting atmosphere,” Journal of the Acoustical Society of America, Vol. 85, 1989, pp. 630-637.

[39] M. J. White and K. E. Gilbert, “Application of the parabolic equation to the outdoor sound propagation,” Appl Acoust. 27(3), 227-238 (1989).

[40] F. D. Tappert, “The parabolic approximation method,” Wave propagation and underwater acoustics, Lecture Notes in Physics. 70, 224-287 (1977).

[41] J. F. Claerbout, Fundamentals of geophysical data processing, Blackwell, Oxford, 1985.

[42] M. West, K. E. Gilbert and R. A. Sack, “A tutorial on the parabolic equation (PE) model used for long range sound propagation in the atmosphere,” Appl Acoust. 37, 31-49 (1992).

[43] J. S. Robertson, W. L. Siegmann, and M. J. Jacobson, “Low-frequency sound propagation modeling over a locally reacting boundary with the parabolic approximation,” J. Acoust. Soc. Am. 98(2), 1130-1137 (1995).

[44] J. S. Robertson, P. J. Schlatter, and W. L. Siegmann, “Sound propagation over impedance discontinuities with the parabolic approximation,” J. Acoust. Soc. Am. 99(2), 761-767 (1996).

[45] V. A. Dougalis, N. A. Kampanis, “Finite element methods for the parabolic equation with interfaces,” J. Comp. Acoustics. 4, 55-88 (1996).

[46] P. Malbequi, “Atmospheric sound propagation using the wide-angle parabolic equation,” ONERA TP, 4, 1996-174 (1996).

[47] J. S. Robertson, “Sound propagation over a large wedge: A comparison between the geometrical theory of diffraction and the parabolic equation,” J. Acoust. Soc. Am. 106(1), 113-119 (1999).

[48] N. A. Kampanis and J. A. Ekaterinaries, “Numerical prediction of far-field wind turbine noise over terrain of moderate complexity,” System Analysis Modeling Simulation. 41, 107-122 (2001).

[49] N. A. Kampanis, “Numerical simulation of low frequency aeroacoustics over irregular terrain using a finite element discretization of the parabolic equation,” J. Comp. Acoustics. 1, 97-112 (2002).

[50] B. Lihoreau, B. Gauvreau, M. Berengier, P.Blanc-Benon, I. Calmet, “Outdoor sound propagation modeling in realistic environment: Application of coupled parabolic equation and atmospheric models,” J. Acoust. Soc. Am. 120(1), 110-119 (2006).

[51] T.Van Renterghem, D. Bottledooren, P.Lercher, “Comparison of measurements and predictions of sound propagation in valley-slope configuration in an inhomogeneous atmosphere,” J. Acoust. Soc. Am. 121(5), 2522-2533 (2007).

[52] N. A. Kampanis, A. I. Delis, D. C. Antonopoulou, G. Kozyrakis, “A finite element discretization of the standard parabolic equation in generalized boundary fitting coordinates,” Applied Numerical Mathematics (2011)

[53] Chevret, P., Blanc-Benon, P., Juve, D., “A numerical model for sound propagation through a turbulent atmosphere near the ground,” Journal of the Acoustical Society of America, Vol. 100, 1996, pp. 3587-3599.

[54] Ph. Blanc-Benon, L. Dallois, D.Juve, “Long range sound propagation over non-flat terrain using parabolic equation,” 11th International Congress on Acoustics, Rome, Italy, 2001.

[55] Michael D. Collins, “A self-starter for the parabolic equation method,” J. Acoust. Soc. Am. 92(4), 2069-2074 (1992).

[56] Robert J. Cederberg and Michael D. Collins, “Application of an improved self-starter to geoacoustic inversion,” I.E.E.E J. Oceanic Engineering 22(1), 102-109 (1992).

[57] Michael D. Collins, “A split-step Pade solution for the parabolic equation method,” J. Acoust. Soc. Am. 93, 1736-1742 (1993).

[58] .H. Chen, D.G.S., “Sound Radiation from and arbitrary body,” Journal of Acoustical Society of America, 1963.35: p. 1626-1632.

[59] W.J. Mansur, C.A.B., “Formulation of the boundary element method for transient problems governed by the scalar wave equation,” Appl. Math. Modelling, 1982. 6:p. 307-311.

[60] W.J. Mansur, C.A.B., “Numerical Implementation of the boundary element method for two-dimensional transient scalar wave propagation problems,” Appl. Math. Modelling, 1982. 6: p. 299-306.

[61] Mansur, W. J., “A Time Stepping Technique to Solve Wave Propagation Problems Using the Boundary Element Method,” 1987, Southhamton University: Southhampton, England.

[62] Hothersall, D. C., Chandler-Wilde, S. N., Hajmirzae, M. N., “Efficiency of single noise barriers,” Journal of Sound and Vibration, Vol. 146, No. 2, 1991, pp. 303-322.

[63] Premat, E., Gabillet, Y., "A new boundary-element method for predicting outdoor sound propagation and application to the case of a sound barrier in the presence of downward refraction," Journal of the Acoustical Society of America, Vol. 108, No. 6, 2000, pp. 3813–3821.

[64] Wu, T.W., Boundary Element Acoustics: Fundamentals and Computer Codes. 2000: WIT Press.

[65] K.R. Kelly, R.W.W., S. Treitel, R.M. Alford, Synthetic Seismograms: a finite difference approach. Geophysics, 1976. 41(1): p. 2-27.

[66] Kelly, K.R., Numerical study of Love wave propagation. Geophysics, 1983.48(7): p. 833-853.

[67] Vireux, J., SH-wave propagation in heterogeneous media: Velocity stress finite-difference method. Geophysics, 1984. 49(1933-1957).

[68] Vireux, J., “P-SV wave propagation in heterogeneous media: Velocity stress finite-difference method,” Geophysics, 1986. 51: p. 889-901.

[69] Q.H. Liu, E.S., F. Daube, C. Randall, H.L. Liu, and P. Lee, “Large-scale 3D finite-difference simulation of elastic wave propagation in borehole environments,” Journal of the Acoustical Society of America, 1994. 94: p. 3337.

[70] Q.H. Liu, E.S., F. Daube, C. Randall, H. L. Liu, and P. Lee, “A three-dimensional finite difference simulation of sonic logging. Journal of the Acoustical Society of America,” 1996.100: p. 72-79.

[71] Colonius, T., Lele, S. K., Moin, P., “The scattering of sound waves by a vortex: numerical simulations and analytical solutions,” Journal of Fluid Mechanics, Vol. 260, 1994, pp. 271-298.

[72] Cheinet, S., Ehrhardt, L., Juve, D., Blanc-Benon, P., “Unified modeling of turbulent effects on sound propagation,” Journal of the Acoustical Society of America, Vol. 132, No. 4, 2012, pp. 2198-2209.

[73] Blumrich, R., and Heimann, D., "A linearized Eulerian sound propagation model for studies of complex meteorological effects," Journal of Acoustics Society of America, Vol. 112, No.2, 2002, pp.446–455.

[74] Salomons, E. M., Blumrich, R., Heimann, D., “Eulerian time-domain model for sound propagation over a finite-impedance ground surface. Comparison with frequency-domain models,” Acta Acustica united with Acustica, Vol. 88, No. 4, 2002, pp. 483-492.

[75] Symons, N. P., Aldridge, D. F., Marlin, D. H., Wilson, D. K., Patton, D. G., Sullivan, P. P., Collier, S. L., Ostashev, V. E., Drob, D. P., “3D staggered-grid finite-difference simulation

of sound refraction and scattering in moving media," in Proceedings of the 11th International Symposium on Long Range Sound Propagation, Fairlee, VT, 2004.

[76] Wilson, D. K., Liu, L., "Finite-difference, time-domain simulation of sound propagation in a dynamic atmosphere," ERDC/CREEL Technical Report No. TR-04-12, 2004, p.56.

[77] Heimann, D., Karle R., "A linearized Euler finite-difference time-domain sound propagation model with terrain-following coordinates, " Journal of the Acoustical Society of America, Vol. 119, 2006, pp. 3813–3821.

[78] Dragna, D., Blanc-Benon, P., Poisson, F., "Time-domain solver in curvilinear coordinates for outdoor sound propagation over complex terrain," Journal of the Acoustical Society of America, Vol. 133, No. 6, 2013, pp. 3751-3763.

[79] Cotte, B., Blanc-Benon, P., Bogey, C., Poisson, F., "Time-domain impedance boundary condition for simulation of outdoor sound propagation," AIAA Journal, Vol. 47, No. 10, 2009, pp. 2391-2403.

[80] Dragna, D., Cotte, B., Blanc-Benon, P., Poisson, F., "Time-Domain simulations of outdoor sound propagation with suitable impedance boundary conditions," AIAA Journal, Vol. 49, No. 7, 2011, pp. 1420-1428.

[81] H. Dong, A.M.K., C. Madshus, and J. M. Hovem, "Sound propagation over layered poro-elastic ground using a finite-difference model," Journal of the Acoustical Society of America, 2000.108: p. 494-502.

[82] Liu, Q., and Oleg V. V. "A Brinkman penalization method for compressible flows in complex geometries." Journal of Computational Physics 227.2 (2007): 946-966.

[83] Berenger, J. P., "A Perfectly Matched Layer for the Absorption of Electromagnetic Waves," Journal of Computational Physics, Vol. 114, No. 2, 1994, pp. 185-200.

[84] Hu, F. Q., "On absorbing boundary conditions for linearized Euler equation by a perfectly matched layer," Journal of Computational Physics, Vol. 129, 1996, pp. 201-219.

[85] Hu, F. Q., "A perfectly matched layer absorbing boundary condition for linearized Euler equations with a non-uniform mean-flow," Journal of Computational Physics, Vol. 208, 2005, pp. 469-492.

[86] J. V. Sanchez-Perez, D. Caballero, R. Martiniez-Sala, C. Rubio, J. Sanchez-Grandia, F. Meseguer, J. Llinares, F. Galvez, "Sound attenuation by a two dimensional array of rigid cylinders," Journal of Physical Review Letters, Vol. 80, No. 24.

[87] J. V. Sanchez-Perez, C. Rubio, R. Martiniez-Sala, R. Sanchez-Grandia, V. Gomez, "Acoustic barriers based on periodic arrays of scatterers," Journal of Applied Physics Letters, Vol. 81, No. 27.

[88] A. Gupta, K. M. Lim and C. H. Chew, "Parametric study on rectangular sonic crystal," Journal of Applied Mechanics and Materials, Vol. 152-154(2012), pp. 281-286.

[89] Krynkin, A., Umnova, O., Sanchez-Perez, J. V., Chong Y. B. A., Taherzadeh, S., Attenborough, K., 2011, "Acoustic insertion loss due to two dimensional periodic arrays of circular cylinders parallel to a nearby surface," Journal of the Acoustical Society of America, Vol. 130, pp. 3736-3742.

[90] Van der Aa, B., Forssen, J., "Upward refraction of sound propagation outdoors by a graded index sonic crystal noise barrier," Applied acoustics, Vol. 74, 2013, pp. 89-101.

[91] Crombie, D. H., Hothersall, D. C., "The performance of multiple noise barriers," Journal of Sound and Vibration, Vol. 176, 1994, pp. 459-473.

[92] Ke, G. and Zheng, Z. C., "Time-domain simulation of long-range sound propagation in an atmosphere with temperature gradient," 51st AIAA Aerospace Sciences Meeting including the New Horizons Forum and Aerospace Exposition, Grapevine, Texas, 2013, pp. 2013-1066.

[93] A. Gupta, K. M. Lim and C. H. Chew, "Analysis of frequency band structure in one-dimensional sonic crystal using Webster horn equation," Journal of Applied Physics Letters, Vol. 98, 201906 (2011).

[94] A. Gupta, K. M. Lim and C. H. Chew, "A quasi two-dimensional model for sound attenuation by the sonic crystals," Journal of Acoustical Society of America, Vol. 0001-4966 (2012), pp. 2909-2914.

[95] Zwikker, C., Kosten, C. W., 1949, Sound Absorbing Materials, Elsevier, New York.

[96] Zheng, Z. C., Li, W., "Numerical stabilities and boundary conditions in time-domain Eulerian simulations of acoustic wave propagations with and without background flow," Applied Mathematics and Computation, Vol. 202, No. 1, 2008, pp. 146-161.

[97] Zheng, Z. C., Ke, G., "Accuracy and efficiency of a moving-zone method in the time-domain simulation," Applied Acoustics 92 (2015) 1-2.

[98] Ke, G., "Time Domain simulation for outdoor sound propagation near the ground considering various barriers and environmental conditions,", University of Kansas, 2014

[99] Ford, R., Smith, S. G. L., "Scattering of acoustic waves by a vortex," Journal of Fluid Mechanics, Vol. 386, 1999, pp. 305-328.

[100] Muller, E. A., Matschat, K. R., "The scattering of sound by a single vortex and by turbulence," Technical Report, Max Planck Institute, 1959.

[101] Harten, A., Engquist, B., Osher, S., Chakravarthy, S., "Uniformly high-order accurate non oscillatory schemes," Journal of Computational Physics, Vol. 71, 1987, pp. 231

[102] Shu, C. W., Zang, T. A., Erlebacher, G., Whitaker, D., Osher, S., “High order ENO schemes applied to two and three dimensional compressible flow,” Applied Numerical Mathematics, Vol. 9, 1992, pp. 45-71.

[103] Liu, X. D., Osher, S., Chan, T., “Weighted essentially non oscillatory scheme,” Journal of Computational Physics, Vol. 115, 1994, pp. 200-212.

[104] Walsteijn, F., “Robust numerical methods for 2D turbulence,” Journal of Computational Physics, Vol. 114, 1994, pp. 129-145.

[105] Jiang, G. S., Shu, C. W., “Efficient implementation of weighted ENO schemes,” Journal of Computational Physics, Vol. 126, 1996, pp. 202–228.

[106] Erlebacher, G., Hussaini, Y., Shu, C. W., “Interaction of a shock with a longitudinal vortex,” Journal of Fluid Mechanics, Vol. 337, 1997, pp. 129-153.

[107] Jiang, G. S., Peng, D., “Weighted ENO schemes for Hamilton-Jacobi equations,” SIAM Journal on Scientific Computing, Vol. 21, 2000, pp. 2126-2143.

[108] Berthelsen, P. A., Faltinsen, O. M., “A local directional ghost cell approach for incompressible viscous flow problems with irregular boundaries,” Journal of Computational Physics, Vol. 227, 2008, pp. 4354-4397.

[109] Xu, Y., Zheng, Z. C., Wilson, D. K., "Simulation of turbulent wind noise reduction by porous windscreens using high-order schemes," Journal of Computational Acoustics, Vol. 18, No. 4, 2010, pp. 321-334.

[110] Xu, Y., Zheng, Z. C., Wilson, D. K., “A computational study of the effect of windscreen shape and flow resistivity on turbulent wind noise reduction,” Journal of the Acoustical Society of America, Vol. 129, No. 4, 2011, pp. 1740-1747.

[111] Ferziger, J. H., “Low-frequency acoustic scattering from a trailing vortex,” Journal of the Acoustical Society of America, Vol. 56, 1974, pp. 1705-1707.

[112] Kop’ev, V. F., Belyaev, I. V., “On the statement of the problem of sound scattering by a cylindrical vortex,” Acoustical Physics, Vol. 54, No. 5, 2007, pp. 603-614.

[113] O’Shea, S., “Sound scattering by a potential vortex,” Journal of Sound and Vibration, Vol. 43, 1975, pp. 109-116.

[114] Tanaka, K., Ishii, S., “Scattering of a plane sound wave by a vortex pair,” Journal of the Physical Society of Japan, Vol. 51, No. 6, 1982, pp. 1992-1999.

[115] Naugolnykh, K., “Sound scattering by a vortex dipole,” Journal of the Acoustical Society of America, Vol. 133, No. 4, 2013, pp. 1882-1884.

[116] Candel, S. M., “Numerical solution of wave scattering problems in the parabolic approximation,” Journal of Fluid Mechanics, Vol. 90, 1979, pp. 465-507.

[117] J. Reinschke, W. Mohring, F. Obermeier, “Scattering of sound waves by a cylindrical vortex: a semi-analytical theory,” J. Fluid Mech. (1997), Vol. 333, pp. 273-299.

[118] G. Brillant, F. Chilla, J. F. Pinton, “Transmission of sound through a single vortex,” Eur. Phys. J. B 37, 229-239 (2004).

[119] I IWATSU, Reima, and Hideo TSURU. "Numerical Simulation of Acoustic Scattering from a Circular Vortex." Theoretical and Applied Mechanics Japan61.0 (2013): 95-104.

[120] Shu, C. W., Osher, S., “Efficient implementation of non-oscillatory shock capturing schemes,” Journal of Computational Physics, Vol. 77, 1988, pp. 439-471.

[121] Osher, S., Sethian, J., “Fronts propagating with curvature-dependent speed: algorithms based on Hamilton-Jacobi formulation,” Journal of Computational Physics, Vol. 79, 1988, pp. 12-49.

[122] Shu, C. W., Osher, S., "Efficient implementation of essentially non-oscillatory shock capturing schemes II," Journal of Computational Physics, Vol. 83, 1989, pp. 32-78.

[123] Osher, S. Shu, C. W., "High-order essentially non oscillatory schemes for Hamilton-Jacobi equations," SIAM Journal on Numerical analysis, Vol. 28, 1991, pp. 907-922.

[124] Jerome, J., Shu, C. W., "Transport effects and characteristic modes in the modeling and simulation of submicron devices," IEEE Transactions on Computer-Aided Design of Integrated Circuits and Systems, Vol. 14, 1995, pp. 917-923.

[125] Admas, N., Shariff, K., "A high-resolution hybrid compact-ENO scheme for shock-turbulence interaction problems," Journal of Computational Physics, Vol. 127, 1996, pp. 27-51.

[126] Lafon, F., Osher, S., "High-order two-dimensional non-oscillatory methods for solving Hamilton-Jacobi scalar equations," Journal of Computational Physics, Vol. 123, 1996, pp. 235-253.

[127] Wismer, G. M., "Finite Element Analysis of Broadband Acoustic Pulses through Inhomogeneous Media with Power Law Attenuation," Acoustical Society of America, 2006, pp. 3493-3502.

[128] Oelze, M. L., O'Brien, W. D., "Frequency dependent attenuation-compensation functions for ultrasonic signals backscattered from random media," Acoustical Society of America, 2002, Vol 111, pp. 2308-2319.

[129] Padilla, F., Peyrin, F., Laugier, P., "Measure of attenuation and backscatter coefficient in trabecular bones using a numerical model of three-dimensional microstructure," Acoustical Society of America, 2003, Vol 113, pp. 1122-1129.

[130] Zhang, X., Broschat, S., Flynn, P., "A comparison of material classification techniques for ultrasound inverse imaging," Acoustical Society of America, 2001, Vol 111, pp. 457-467.

[131] Hughes, D. I., Duck, F. A., "Automatic attenuation compensation for ultrasonic imaging," Ultrasound Med. Biol. 23, pp. 651-664

[132] He. P., "Experimental verification of models for determining dispersion from attenuation," IEEE Trans. Ultrason. Ferroelectr. Freq. Control Vol. 46, pp. 706-714.

[133] Girault, J. M., Ossant, F., Ouahabi, A., Kouame, Patat, F., "Time-varying autoregressive spectral estimation for ultrasound attenuation in tissue characterization," IEEE Trans. Ultrason. Ferroelectr. Freq. Control Vol. 45, pp. 650-659.

[134] Treeby, B. E., Cox, B. T., "Modeling Power Law Absorption and Dispersion for Acoustic Propagation Using the Fractional Laplacian," Acoustical Society of America, 2010, pp. 2741-2748.

[135] Gorenflo, R., Mainardi, F., "Random Walk Models for Space Fractional Diffusion Processes," Fractional Calculus and Applied Analysis, Vol. 1, No. 2, 1998, pp. 167-191.

[136] Meerchaert, M. M., Tadjeran, C., "Finite Difference Approximations for Two-Sided Space-Fractional Differential Equations," Applied Numerical Mathematics, Vol. 56, No. 1, 2006, pp. 80-90.

[137] Wang, Z., "A Numerical Method for Delayed Fractional-Order Differential Equations," Journal of Applied Mathematics, Vol. 2013.